DISSERTATION

Experimental Investigation of the Flow Field in an Adaptive Throttling Nozzle

carried out for the purpose of obtaining the degree of

Doctor technicae (Dr. techn.)

submitted to

Technische Universität Wien, Faculty of Mechanical and Industrial Engineering

by

Khoiri Rozi, M. Eng

Matr. Nr.: 1428680

under the supervision of

Ao. Univ. Prof. Dipl.-Ing. Dr. techn. Reinhard Willinger

Institute for Energy Systems and Thermodynamics

reviewed by

Univ. Prof. Dipl.-Ing. Dr.-Ing. Christian Bauer

and

Ao. Univ. Prof. Dipl.-Ing. Dr. techn. Andreas Werner

Vienna, October 2019

Die approbierte gedruckte Originalversion dieser Dissertation ist an der TU Wien Bibliothek verfügbar.
The approved original version of this doctoral thesis is available in print at TU Wien Bibliothek.

This work was supported by LPDP - Indonesian Endowment
Fund for Education
Contract Nr.: 20131222010576

DEDICATION

I dedicate this dissertation to:
Diponegoro University
Ministry of Research, Technology and Higher Education
Republic of Indonesia

Die approbierte gedruckte Originalversion dieser Dissertation ist an der TU Wien Bibliothek verfügbar.
The approved original version of this doctoral thesis is available in print at TU Wien Bibliothek.
TU Bibliothek Your knowledge hub WIEN

Abstract

The adaptive stage could be a very reliable solution to avoid an off-design performance in extraction turbines where the highly improved circumferential nonuniformities of the flow and efficiency are needed without significant losses in enthalpy and pressure drop inside the stage. However, the mechanism that is responsible for high performance adaptive stage and the influence of parameters which has limited the efficiency are not well understood nowadays. In this thesis, the flow field in the throttling nozzle used for adaptive stage has been investigated experimentally with an emphasis on the midspan wakes and the endwall secondary flows. A nozzle geometry with fully opening condition was used for this study to describe the basic characteristic of the throttling nozzle flows. Moreover, two different closing techniques with the same design point to regulate the flow capacity are developed and tested on a linear cascade: these are referred to as closing to the pressure side (CPS) and closing to the suction side (CSS).

A detailed investigation of the throttling nozzle has been conducted using a linear cascade wind tunnel. The design and experiment methods are based on the previous research in thermal laboratory of Technische Universität Wien. Measurements were achieved by total and wall static pressure probe, static pressure taps, pneumatic probes, and a hot-wire anemometry. An original database was thus documented. Using the pressure taps, the distribution of blade loading in term of static pressure at midspan was measured and used to define a region of favourable and adverse pressure gradient in fully opening cascade. Furthermore, a description of the two-dimensional flow at midspan was tested using two devices involving three-hole probe and single hot-wire to reveal the wake profiles. From these measurements, an increase in the degree of closing leads to an increase of flow nonuniformity in line with an increase of the profile loss and an enlarge of the wake width, however, it reduces static pressure for both closing types investigated.

The existence of three-dimensional flow was measured using a five-hole probe. Based on this measurement, the flow field near the endwall is highly three-dimensional occupied by the passage vortex, the counter-rotating vortex, and the suction side leg of the horseshoe vortex. The cores of passage vortex are found more clearly through the isoclines contour of the pitchwise flow angle than in the isoclines contour of the spanwise flow angle. The total pressure deficit and the secondary kinetic energy increase considerably in the secondary flow region compared to the midspan region in all measurement cases. Measurements by partially closing degree indicate a unique result which is that the changes of the closing degree have a substantially effect on the flow structures where the flow field is dominated by the secondary flows with strong vorticity at low degree of closing, however, this flow structure is found to be weak with a significant reduction of the vortex strength at higher closing degree for both closing models examined.

Die approbierte gedruckte Originalversion dieser Dissertation ist an der TU Wien Bibliothek verfügbar.
The approved original version of this doctoral thesis is available in print at TU Wien Bibliothek.
TU Bibliothek Your knowledge hub WIEN

Kurzfassung

Zur Regulierung des Entnahmedruckes von Entnahme-Dampfturbinen stehen verschiedene technische Möglichkeiten zur Verfügung. Die einzelnen Lösungen weisen spezifische Vor- und Nachteile auf. Bei der sogenannten adaptiven Stufe wird die Leitschaufelreihe aus einem im Gehäuse fixen Festring und einem in Umfangsrichtung verstellbaren Drehring gebildet. Diese Ausführung zeichnet sich auch bei hohen Schließgraden durch eine über den Umfang gleichmäßig verteilte Strömung in der Stufe aus. Die Motivation für die vorliegende Arbeit ergibt sich aus der Tatsache, dass in der offenen Literatur relativ wenige Informationen über adaptive Turbinenstufen zu finden sind. Es wurden experimentelle Untersuchungen durchgeführt, die zur Verbesserung des Verständnisses der räumlichen Strömungsverhältnisse im Drehschieber für eine adaptive Turbinenstufe führen sollen. Neben dem voll geöffneten Drehschieber wurde der Einfluss verschiedener Schließgrade untersucht. Dabei wurde zwischen einem Schließen Richtung Druckseite bzw. Saugseite unterschieden. Man spricht in diesem Zusammenhang auch von Saugseitenüberdeckung bzw. Druckseitenüberdeckung.

Als Basis diente eine Gittergeometrie, in der die ebene Strömung in vorangegangenen Arbeiten numerisch und experimentell untersucht wurde. Im Rahmen dieser Arbeit wurden Strömungsmessungen im ebenen Gitterwindkanal des Institutes durchgeführt. Bei voll geöffnetem Drehschieber wurde die statische Profildruckverteilung in halber Schaufelhöhe gemessen. Aus der Profildruckverteilung lassen sich Gebiete mit verzögerter bzw. beschleunigter Strömung identifizieren. Zur Messung der ebenen Nachlaufströmung in halber Schaufelhöhe wurde sowohl eine pneumatische Dreilochsonde als auch eine 1D-Hitzdrahtsonde verwendet. Der Abströmwinkel nimmt mit steigendem Schließgrad ab und die Totaldruckverluste nehmen zu. Bei höheren Schließgraden nimmt die Nachlaufdelle schließlich die komplette Schaufelteilung ein, was auch aus der Verteilung des Turbulenzgrades ersichtlich ist.

Zur Messung der räumlichen Abströmung wurde eine pneumatische Fünflochsonde eingesetzt. Bei voll geöffnetem Drehschieber konnten die typischen Merkmale der räumlichen Abströmung eines ebenen Turbinengitters (Kanalwirbel, Hufeisenwirbel, Eckenwirbel) identifiziert werden. Zur Lokalisierung des Kanalwirbels eignet sich die Verteilung des Abströmwinkels in Umfangsrichtung besser als jene in Schaufellängsrichtung. Die Strömung in der Nähe der Seitenwand ist durch hohe Totaldruckverluste sowie eine hohe kinetische Energie der Sekundärströmung geprägt. Mit steigendem Schließgrad werden die räumlichen Strömungseffekte unterdrückt und die Abströmung wird durch den Einfluss der Strömung hinter dem jeweils rückspringenden Teil des Drehringes dominiert. Bezüglich der Totaldruckverluste zeigt die Saugseitenüberdeckung Vorteile gegenüber der Druckseitenüberdeckung.

Die approbierte gedruckte Originalversion dieser Dissertation ist an der TU Wien Bibliothek verfügbar.
The approved original version of this doctoral thesis is available in print at TU Wien Bibliothek.
TU Bibliothek Your knowledge hub WIEN

Acknowledgments

This dissertation is a monograph, the results of my experimental research in the Technical University of Vienna. The study has been financially supported by Indonesian Endowment Fund for Education (LPDP) through the scheme of a postgraduate scholarship program. All their financial support is gratefully appreciated and acknowledged.

First and foremost, I would like to express my sincere gratitude to my supervisor Ao. Univ. Prof. Dr. techn. Reinhard Willinger for providing me a chance to study this interesting research in an excellent working environment. His comprehensive knowledge and deep understanding the field of turbomachinery and experimental methods proved invaluable to me throughout the course of this study. I am grateful to him for his invaluable guidance, motivations and supervision throughout the time of my study.

Next, I would like to thank to Univ. Prof. Dr.-Ing. Christian Bauer and Ao. Univ. Prof. Dr. techn. Andreas Werner for reviewing this manuscript.

Later, I would like to extend my gratitude and appreciation to Dipl.-Ing Lukas Hofmann for his help and support in the collecting of measurement data for my research. Likewise, special gratitude goes to Mr. Franz Trummer for his skilled work and dedication for IT-computer support during my research. Similarly, special thanks also go to all technicians at thermal laboratory for supporting me with this work. Further, my sincere thanks go to my colleagues at the department of Fluid-Flow Machinery, Dr. techn. Pouya Ghaffari, Dr. techn. Leopold Ruppert, Dipl.-Ing Julian Unterluggauer, and Dipl.-Ing Christoph Öttl for creating an encouraging atmosphere and their support during my study. Thanks also go to all friends in Institute for Energy Systems and Thermodynamics for their kind cooperation and help during my study and stay in Vienna.

Finally, and most importantly, I wish to thank and to express my deepest appreciation to my parents, my sisters, my wife and all my families for always believing in me and the endless supports during the time of this study.

Die approbierte gedruckte Originalversion dieser Dissertation ist an der TU Wien Bibliothek verfügbar.
The approved original version of this doctoral thesis is available in print at TU Wien Bibliothek.
TU Bibliothek Your knowledge hub WIEN

Table of contents

Abstract i
Kurzfassung ii
Acknowledgments iii
Table of contents iv
Nomenclature vi

1 Introduction 1

2 Literature Review 4
2.1 Extraction turbines 4
2.2 Control mechanism 9
2.2.1 Throttle control 9
2.2.2 Nozzle group control 10
2.2.3 Adaptive control 12
2.3 Adaptive control stage 13
2.3.1 Rotated stator 13
2.3.2 Flap nozzle 14
2.3.3 Throttling nozzle 15
2.4 Performance of axial turbine 18
2.4.1 Classification of the losses 18
2.4.2 Loss coefficients 18
2.4.3 Efficiency of turbine 21
2.5 Flow fields in a turbine cascade 23
2.5.1 Two-dimensional flow field 23
2.5.2 Three-dimensional flow field 25

3 Experimental facility and methods 30
3.1 Cascade geometry 30
3.2 Linear cascade wind tunnel 34
3.3 Free jet facility 38
3.4 Pneumatic measuring systems 40
3.4.1 Total and static pressure probe 40
3.4.2 Static pressure taps 42
3.4.3 Three-hole pneumatic probe 42
3.4.4 Five-hole pneumatic probe 44
3.5 Hot-wire anemometry 48
3.6 Uncertainty analysis 50
3.6.1 Statistical uncertainty 50
3.6.2 Uncertainties of operating condition 52
3.6.3 Uncertainty of outlet flow parameter 54

Die approbierte gedruckte Originalversion dieser Dissertation ist an der TU Wien Bibliothek verfügbar.
The approved original version of this doctoral thesis is available in print at TU Wien Bibliothek.
TU Bibliothek Your knowledge hub WIEN

4 Results of the fully opening cascade 61
4.1 Two-dimensional flow field 61
4.1.1 Blade loading 61
4.1.2 Exit flow angle 62
4.1.3 Nondimensional velocity 63
4.1.4 Static pressure coefficient 64
4.1.5 Total pressure coefficient 64
4.1.6 Turbulence intensity 64
4.2 Three-dimensional flow field 65
4.2.1 Pitchwise flow angle 65
4.2.2 Spanwise flow angle 66
4.2.3 Nondimensional velocity 66
4.2.4 Secondary kinetic energy 67
4.2.5 Nondimensional vorticity 68
4.2.6 Total pressure coefficient 70
4.2.7 Pitchwise-averaged distribution 71

5 Results of the partially closing for CPS and CSS 75
5.1 Two-dimensional flow field 75
5.1.1 Exit flow angle 75
5.1.2 Nondimensional velocity 75
5.1.3 Static pressure coefficient 76
5.1.4 Total pressure coefficient 77
5.1.5 Turbulence intensity 78
5.1.6 Pitchwise-averaged distribution 79
5.2 Three-dimensional flow field 81
5.2.1 Pitchwise flow angle 81
5.2.2 Spanwise flow angle 84
5.2.3 Nondimensional velocity 84
5.2.4 Secondary kinetic energy 86
5.2.5 Nondimensional vorticity 86
5.2.6 Total pressure coefficient 89
5.2.7 Pitchwise-averaged distribution 91

6 Conclusion and outlook 95

References 98

Appendix 102

Die approbierte gedruckte Originalversion dieser Dissertation ist an der TU Wien Bibliothek verfügbar.
The approved original version of this doctoral thesis is available in print at TU Wien Bibliothek.
TU Bibliothek Your knowledge hub WIEN

Nomenclature

Latin letters and notation

a	Maximum closing depth (mm)
a'	Closing length (mm)
AR	Aspect ratio, H/c (-)
b	Axial chord (mm)
C	Absolute velocity (m/s), chord length (mm)
C_p	Blade pressure coefficient (-)
C_{ps}	Static pressure coefficient (-)
C_{pt}	Total pressure coefficient (-)
C_{SKE}	Secondary kinetic energy coefficient (-)
$\bar{C}_{pt}$	Average total pressure coefficient (-)
$\bar{C}_{SKE}$	Average secondary kinetic energy coefficient (-)
H	Enthalpy (J), Span (mm)
h	Specific enthalpy (J/kg)
I	Inertia moment ($kg.m^2$)
k	Isentropic index (k = 1.4)
k_β	Yaw angle coefficient (-)
k_γ	Pitch angle coefficient (-)
k_s	Static pressure coefficient (-)
k_t	Total pressure coefficient (-)
l	Blade length/span (m)
Ma	Mach number (-)
p	Surface static pressure on the blade surface (Pa)
p_o	Static pressure in the inlet test section (Pa)
p_s	Static pressure (Pa)
p_t	Total pressure (Pa)
$\bar{p}$	Average pressure (Pa)
R	Specific gas constant (J/kg. K)
Re	Reynolds number (-)
S	Entropy ([J/K), Sutherland constant (K)
s	Specific entropy (J/kg. K)
t	Pitch (mm)
T	Temperature (K)
To	Reference temperature for Sutherland's law (K)
Tu	Turbulence intensity (%)
Y_R	Profile loss coefficient of rotor (-)
Y_S	Profile loss coefficient of stator (-)

Die approbierte gedruckte Originalversion dieser Dissertation ist an der TU Wien Bibliothek verfügbar.
The approved original version of this doctoral thesis is available in print at TU Wien Bibliothek.
TU Bibliothek Your knowledge hub WIEN

Greek letters and symbol

α_1	Pitchwise flow angle (°)
$\bar{\alpha}_1$	Averaged pitchwise flow angle (°)
$\bar{\alpha}_{1MS}$	Midspan-pitchwise flow angle (°)
β_1	Spanwise flow angle (°)
$\bar{\beta}_1$	Averaged spanwise flow angle (°)
$\Delta\beta$	Yaw angle (°)
γ	Stagger angle (°)
$\Delta\gamma$	Pitch angle (°)
δ	Closing degree (%)
Δ	Incremental difference
ε	Relative uncertainty (%)
η	Efficiency (%)
μ	Dynamic viscosity (Pa. s)
π_T	Degree of expansion (-)
ρ	Fluid density (kg/m^3)
σ	Solidity [-], absolute uncertainty (-)
υ	Kinematic viscosity (Pa. s)
ω	Vorticity (1/s)
Ω	Normalized vorticity (-)
ξ_R	Kinetic energy loss of rotor (-)
ξ_S	Kinetic energy loss of stator (-)
Ψ	Zweifel coefficient (-)
ζ_R	Enthalpy loss coefficient of rotor (-)
ζ_S	Enthalpy loss coefficient of stator (-)

Abbreviations

CPS	Closing to pressure side
CSS	Closing to suction side
CTA	Constant temperature anemometry
FP	Fixed part
HWA	Hot-wire anemometry
MP	Movable part
PS	Pressure side
SKE	Secondary kinetic energy
SS	Suction side
1D	One-dimensional
2D	Two-dimensional

Die approbierte gedruckte Originalversion dieser Dissertation ist an der TU Wien Bibliothek verfügbar.
The approved original version of this doctoral thesis is available in print at TU Wien Bibliothek.
TU Bibliothek Your knowledge hub WIEN

3D	Three-dimensional
3H-P	Three-hole pressure probe
5H-P	Five-hole pressure probe

Superscripts

$\overline{...}$	Average

Subscripts

0	Inlet
1	Outlet
MS	Midspan
P	Pressure, profile
R	Rotor
r	Relative
rms	Root mean square
S	Stator, secondary
s	Static, streamwise, secondary
ss	Static-to-static
t	Total
ts	Total-to-static
tt	Total-to-total
x	Axial direction
y	Pitchwise direction
z	Spanwise direction

Die approbierte gedruckte Originalversion dieser Dissertation ist an der TU Wien Bibliothek verfügbar.
The approved original version of this doctoral thesis is available in print at TU Wien Bibliothek.
TU Bibliothek Your knowledge hub WIEN

1 Introduction

Steam turbines are one of the most vital rotating machines of a family of turbomachines used for the prime mover in the world, which can extract thermal energy from pressurized steam into mechanical work. Since their introduction in 1884, the steam turbine has had an enormous development and significant market expansion as the energy production devices over the last several decades. Steam turbines (Fig. 1.1) are found in various industries and used in a variety application in the plant purposes because of their high performances and low operating cost. Many industrial applications of steam turbines can be found in the chemical and petrochemical plants mainly in the process facilities of petroleum and gas refinery, in cogeneration plants, and in other users which have certain process including pulp and paper mills, metallurgical works, and mining interests. In these industries, steam turbines can improve efficiency of the plant by allowing the motive steam to first expand through a series of blades and then to be used for supplying heat to process in the plant or as utility steam for heating buildings. Due to constantly increasing demands for heat and mechanical power in these industries, steam turbines will keep its central position as a primary equipment of the energy production in the coming decades.

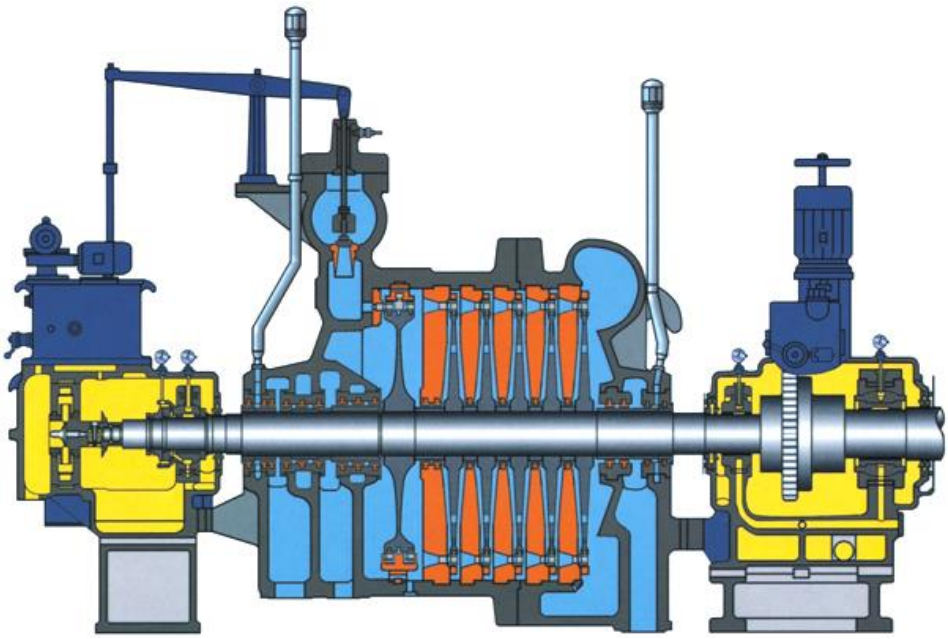

Figure 1.1 Cross-sectional views of typical industrial steam turbines
(Source: www.qdjnpse.com)

The importance and leading role of steam turbines in technological process industries leads to continuously strive for enhancement of efficiency and reliability of these turbines. As mentioned previously, many industrial applications require the extraction turbines which regulate two or more parameters because economically benefits result from more efficient

Die approbierte gedruckte Originalversion dieser Dissertation ist an der TU Wien Bibliothek verfügbar.
The approved original version of this doctoral thesis is available in print at TU Wien Bibliothek.
TU Bibliothek Your knowledge hub WIEN

use of energy by saving the fuel consumption. However, the extraction of steam for these industries can potentially lead to the off-design performance of these turbines at variable operations. In preventing this off-design performance impact, one method is necessary for the application of control valve that can adapt blading system of the turbine to changeable load condition. This control valve is well-known as adaptive stage of flexible geometry located directly downstream of the extraction point where expended steam extracted. This flexible geometry consists of a rotary ring and immovable main part with shaped regions of nozzle vanes. When condition of diaphragm is fully opened, both parts of the nozzle vanes form single channels. During extraction of steam to the extraction point, the rotary ring with movable blades of nozzle vanes will change a cross-section of flow passage, thereby changing the removed steam mass flow capacity.

One of the main challenges on the design of an adaptive stage, especially throttling nozzle is the reduction of losses affected by the wake and secondary flows of the nozzles. Since in practice, the steam extraction through the throttling process in the turbine stage can cause the complex flow interaction that produces various loss creating mechanisms. In extraction turbines with the throttling nozzle as an extraction control valve, a larger closing position from the fully opening channel must be arranged to obtain the same work from the rotor of the turbine. Consequently, flow separation occurs in the corner downstream of the leading edge. The results of a vorticity transport from this separation through the nozzles are high fluctuating components of pressures acting on the nozzle blades that can cause a significant drop in turbine efficiency. Although development of modern steam turbines has made great advancements in extraction control technology over the past several decades, there are yet many design aspects remaining unexplored that provide a chance for further enhancements. Therefore, efficiency improvement in steam turbines is an extremely important aspect to mitigate the impact of performance deterioration and has become a very crucial issue in the research and development sector of the steam turbine industry.

In the current research, the flow field in the throttling nozzle is studied. This nozzle flow field contains loss regions caused by the flow encounters a forward- and a backward-facing step geometry simultaneously resulting in a separated-reattached flow forming within the flow passage. The separated-reattached structure with recirculation zones convects into the blade-to-blade interaction mechanisms take place between the loss regions of both nozzle blade rows. Further downstream the resultant flow field is highly complex flow involving the nozzle wakes and the nozzle secondary flows. Such flow structures and its detrimental impact on the turbine performance have been extensive investigated in the last few decades but these formations in the throttling nozzle have not been completely studied until today. Thus, this research work is intended to perform a careful experimental measurement of the throttling nozzle flow field with an emphasis on the midspan and the endwall flows. The purpose of this study is to elucidate the wake transport phenomena related to the pressure losses and to understand profoundly of the secondary flows associated with the endwall losses through the influential flow parameter measurements.

Die approbierte gedruckte Originalversion dieser Dissertation ist an der TU Wien Bibliothek verfügbar.
The approved original version of this doctoral thesis is available in print at TU Wien Bibliothek.
TU Bibliothek Your knowledge hub WIEN

The following research thesis consists of some chapters and is organized as follows: An introduction including background, motivation, and objectives of the research is presented in Chapter 1. A general concept of extraction turbine, control systems, and cascade flow fields are reviewed in Chapter 2. Then, a detailed description of the experimental methods, instrumentation and data acquisition system and uncertainty analysis for the measurements are described in Chapter 3. Chapter 4 concentrates on the measurement results of global flow parameters at the fully opening of the cascade. Chapter 5 devotes an analyzing the difference of flow features between the two closing models of closing to pressure side and closing to suction side. Finally, conclusions from the research and recommendations for future work are given in Chapter 6.

Die approbierte gedruckte Originalversion dieser Dissertation ist an der TU Wien Bibliothek verfügbar.
The approved original version of this doctoral thesis is available in print at TU Wien Bibliothek.
TU Bibliothek Your knowledge hub WIEN

2 Literature review

2.1 Extraction turbines

Steam turbines are energy conversion machines that extract energy from the steam and convert it to mechanical work. The amount of energy that the steam turbine extracts from the steam depends on the enthalpy reduction inside the blading system of the turbine. The enthalpy of the steam is a state function of its pressure and temperature. The two principal classifications of steam turbines are the backpressure and the condensing. The exhaust pressure of a backpressure turbine is equal to or higher than atmospheric while that of a condensing turbine is usually sub-atmospheric. Backpressure turbines usually are used in the process industries, which expand the live steam supplied by boiler to the pressure at which the steam is needed for the process while condensing turbines are most often used for electric power production where process steam is not necessary. In general, physical size and power output of backpressure turbines are smaller than an equivalent condensing unit, and usually operate at much faster rotational speeds while physical size and power output of condensing turbines tend to be larger.

Extraction turbines may be conceived as two-stage units from which steam can be removed at a pressure between that of the supply and that of the exhaust. Such turbines usually have one or more openings in its casing for removing the amount of steam at some intermediate pressure. For their name, the term of extraction turbines stems from a fact that steam is extracted from the extraction point in the steam turbine. The extracted steam may be used for the process requirement within the plant, and it can be used to improve the efficiency of the thermodynamic cycle. The optimum operation point of the extraction process depends on required steam pressure, temperature and quantity overload range. These parameters are essential in determining the kind of steam turbine and the cycle that should be used in the plant. The extraction of the steam pressure may or may not be automatically controlled depending on the design of the turbine. Controlled, or regulated extraction allows for better adaptations of the steam flow through the turbine to produce additional mechanical work depending on the operating condition and purposes.

Extraction turbines can be either backpressure or condensing, depending on the particular purpose. The extraction backpressure turbine as illustrated in Fig. 2.1 is used where the process steam is used at two or more different pressure levels. Backpressure turbine is designed so that the exhaust pressure matches the process requirement. The efficiency of this kind turbine extracting to a process is high because of considerable losses in the form of heat through the condenser being eliminated. The extraction condensing turbine as shown in Fig. 2.2 is used where the power needed is in excess of the process steam. This is a combination of the backpressure and condensing type where the extraction pressure is fixed by the process steam pressure required, while the exhaust pressure is determined as

Die approbierte gedruckte Originalversion dieser Dissertation ist an der TU Wien Bibliothek verfügbar.
The approved original version of this doctoral thesis is available in print at TU Wien Bibliothek.
TU Bibliothek Your knowledge hub WIEN

for the condensing turbine. Here, the process steam is extracted from the steam turbine and the steam which is not extracted for the process further expands in the turbine and is then condensed in a condenser. This type has efficiency lower than a backpressure turbine due to the partial heat loss in the condenser. However, the advantage of this turbine is that the power generated is not proportional to the process steam needed such that power can be generated whilst the process in the plant is shut down.

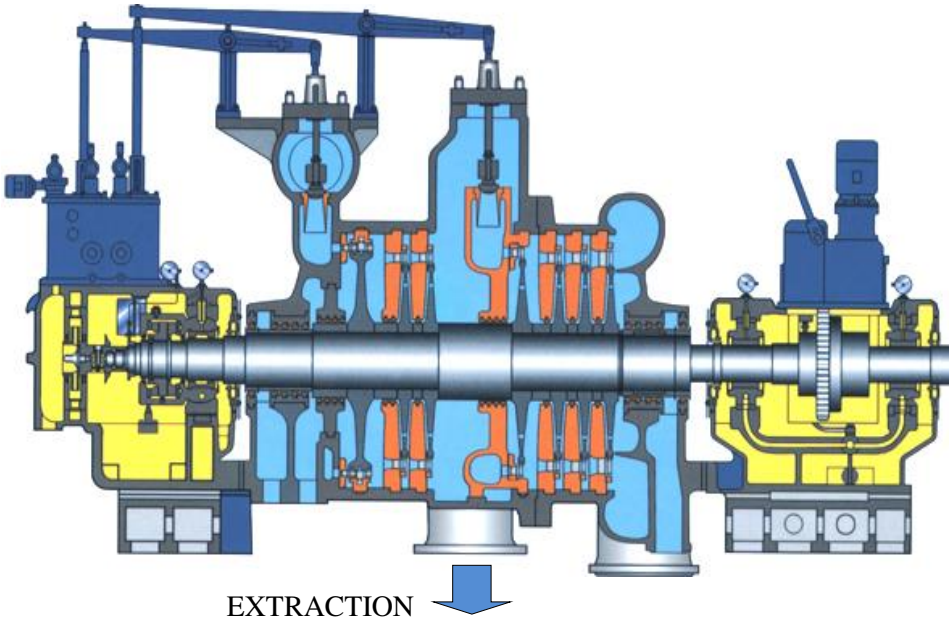

Figure 2.1 A type of extraction backpressure turbine with single extraction (Source: www.qdjnpse.com)

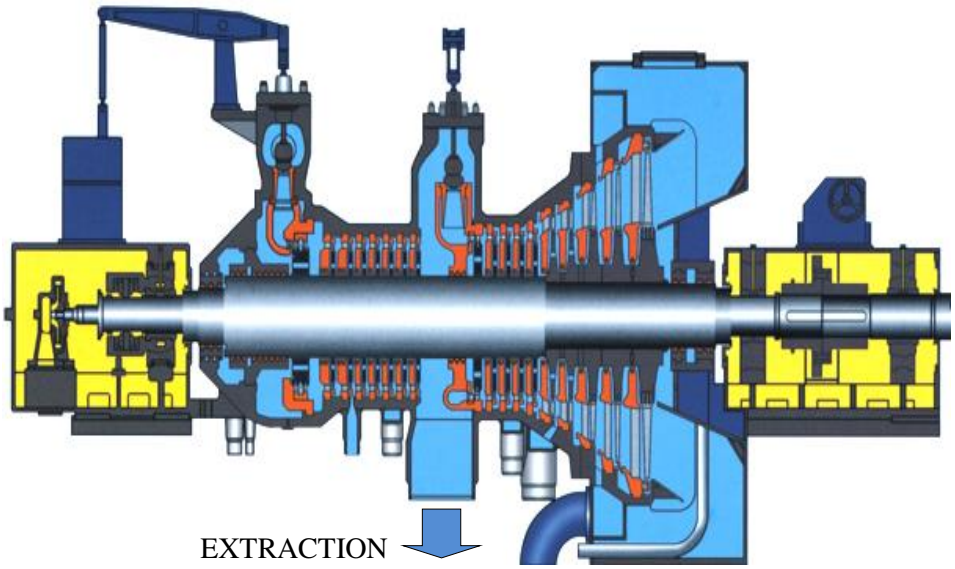

Figure 2.2 A type of extraction condensing turbine with single extraction (Source: www.qdjnpse.com)

Die approbierte gedruckte Originalversion dieser Dissertation ist an der TU Wien Bibliothek verfügbar.
The approved original version of this doctoral thesis is available in print at TU Wien Bibliothek.
TU Bibliothek Your knowledge hub WIEN

In single extraction turbines as depicted in Fig. 2.1 and 2.2, the steam is admitted through the steam control valve and passes through the high-pressure stages. An extraction valve then divides the steam flow path into an extraction stream and a low-pressure stream. The extraction stream escapes the steam turbine to be used elsewhere in the facility for process purposes. The low-pressure stream flows through the low-pressure stages and into an exhaust steam header in the case of a backpressure turbine, or into a condenser in the case of a condensing turbine. For double extraction turbines, the basic operation is similarly as single extraction turbines, but there are two extraction valves enabling two extraction points for process steam. The detailed overview of the extraction turbines and their control systems can be found in Bloch and Singh [6], and Platz [34].

Extraction map: The relationship between the power obtainable and the steam quantities flowing is illustrated in the extraction map as shown in Fig. 2.3. This is a graph description of the extraction operating range for an extraction turbine that relates throttle flow to turbine electrical and thermal power output. Moreover, this map defines the relationships between inlet valve and extraction valve as well as defines the steam extraction boundaries, i.e., maximum and minimum extraction flow rate.

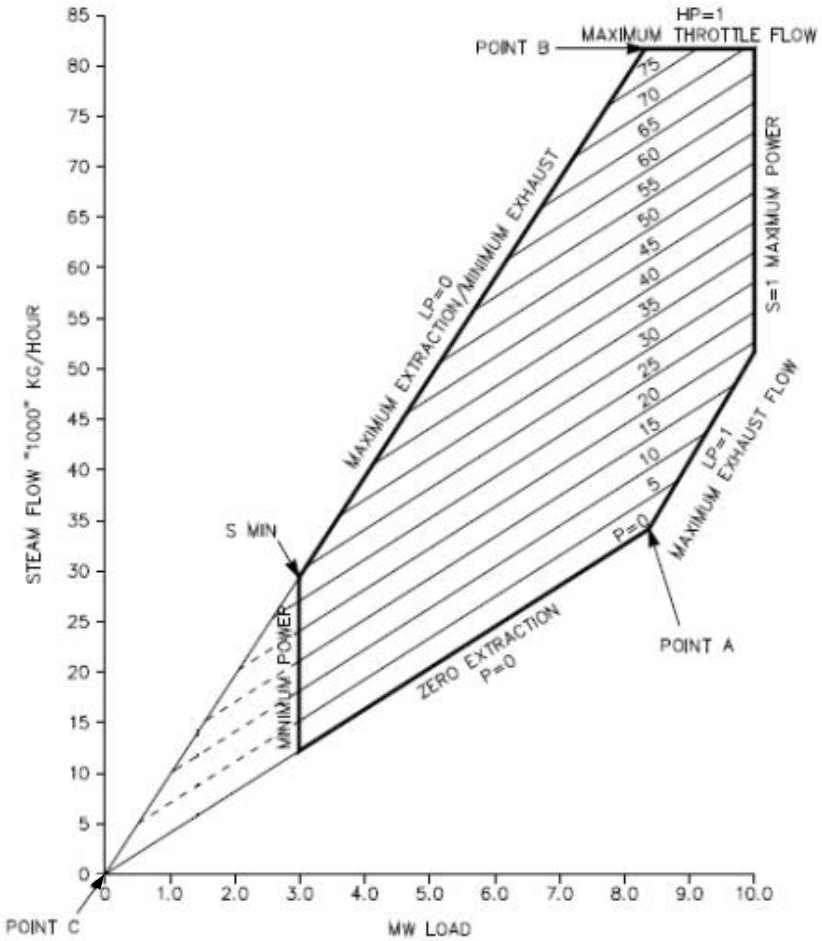

Figure 2.3 Extraction map for operating the extraction steam turbines [34]

Die approbierte gedruckte Originalversion dieser Dissertation ist an der TU Wien Bibliothek verfügbar.
The approved original version of this doctoral thesis is available in print at TU Wien Bibliothek.

The principles of boundary lines on the extraction map can be explained as follows. The vertical coordinate stands for the total steam flow through the turbine inlet, the sum of exhaust and extraction flows, and the horizontal coordinate shows the total power developed of extraction turbine. The total extraction line is the steam flow required when exhaust flow is zero. The extraction lines show the total inlet steam flow for various loads when the flow indicated is extracted.

The maximum throttle flow line (HP = 1) represents the point at which the inlet (HP) valve is at full open, which means the turbine is passing the maximum steam flow allowed with the design steam conditions. The maximum power line (S = 1) represents the maximum power output of the turbine with design steam conditions. Take, for example, a point of intersection between HP = 1 and S = 1, this point shows that maximum power is obtainable by passing the steam quantity through the high-pressure part (HPP), and the quantity through the low-pressure part (LPP).

The maximum exhaust flow line (LP = 1) is a real limit of the turbine in that greater exhaust flows would cause the turbine to operate at higher exhaust pressures. For instance, at the point of intersection between S = 1 and LP = 1, the maximum power is still obtainable, the high-pressure steam flow dropping, the low-pressure steam flow increasing; the reduction in live steam is, therefore, balanced by the increased steam quantity flowing through the low-pressure part (LPP).

The zero-extraction flow line (P = 0) stands for the steam flows required for various loads when extraction flow is zero. This also means the throttle flow from minimum load to maximum exhaust flow, with no extraction steam flow demand.

The minimum exhaust flow (LP = 0) represents the combination of throttle and extraction flow, and associated power output, when minimum steam flow passes to the exhaust section of the turbine. In all turbines there must be a minimum amount of steam flowing through the exhaust in order to avoid overheating this section of the turbine. In effect, the extraction (LP) valve would be fully closed. More details information about the use of the map of extraction was given by Platz [34].

Cogeneration application: Cogeneration is a simultaneous production of electricity and heat in the same thermal power plant. In cogeneration system, the installed power of an extraction turbine constitutes a considerable part of the total electric power. Therefore, the increasing efficiency and reliability are the real issue in their operation.

A main feature of cogeneration system is a diversity of operational conditions. In general, these conditions can be subdivided into the three modes of operation: (i) condensing mode, (ii) operating according to the heat supply demand, and (iii) operating according to the electricity demand. Such diversity conditions make an extremely variable operation of the

Die approbierte gedruckte Originalversion dieser Dissertation ist an der TU Wien Bibliothek verfügbar.
The approved original version of this doctoral thesis is available in print at TU Wien Bibliothek.
TU Bibliothek Your knowledge hub WIEN

low-pressure flow path in the extraction turbines. In this connection, an increase in the efficiency of an extraction turbine unit may be reached primarily through optimization of the design and the provision of the most efficient conditions of the low-pressure part (LPP) operation. Consequently, the efficiency of the LPP significantly depends on the operating mode of the extraction turbines.

Simoyu et al. [42] studied effects of these operation modes on the efficiency of the LPP and found that in a condensing mode where the main steam part operates in the entire steam turbine and the exit steam fed into the condenser, the efficiency of the LPP is not only influenced by the steam flow rate and its initial and final parameters but also determined by the degree of opening the control diaphragm. While in extraction turbine with operating according to the heat supply demand where the diaphragm is maximally closed and the most of steam is fed into a heater or delivered to the steam bleed-offs (cogeneration mode), the efficiency is reached by decreasing heat losses in the cold source through minimization of the steam flow rate in the LPP and other steam–water flows directed into a condenser. Further in extraction turbines with operating according to an electricity demand, a certain amount of the steam through the LPP with the steam flow being varied as a function of the electric and heat loads, therefore the efficiency proper is determined by the internal relative of the LPP efficiency due to the last stage operates in a ventilating mode and do not produce power.

In order to ensure high efficiency of the extraction turbines within a wide range of the operation conditions, the choosing of the LPP should be made while considering the situations of operation with respect to both electric and heat loads and the temperature of the feed circulation water. An effort has been proposed by Batenin et al. [2] to increase the extraction turbines efficiency through controlling an outlet steam pressure by using heat pump that operates with steam. Main result of this experimental work showed that several operating modes of the extraction turbine unit can effectively be improved by installing and operating the heat pump plant which its energy consumption can be supplied by optimizing the steam expansion process in LPP.

The extraction turbine characteristics describing the operation modes as shown by Batenin et al. [2] are usually presented by the dependencies of the efficiency and the dimensionless flow rate ($\overline{G}$) which is defined as

$$\overline{G} = \frac{G\sqrt{RT}}{Fp} \tag{2. 1}$$

where G is the mass flow rate, R is the gas constant, T and p are the temperature and pressure at the inlet to the turbine, and F is the characteristic square on the degree of expansion π_T. Since the rotational speed is constant and inlet temperature changes slightly in all operating modes of the LPP. Therefore, the characteristic of LPP can be presented as only the dependencies on the degree of expansion.

Die approbierte gedruckte Originalversion dieser Dissertation ist an der TU Wien Bibliothek verfügbar.
The approved original version of this doctoral thesis is available in print at TU Wien Bibliothek.
TU Bibliothek Your knowledge hub WIEN

Figure 2.4 describes the LPP characteristics points where the operation mode of extraction turbine is uniquely identified by the degree of expansion at constant rotational speed and constancy of the geometrical dimensions of flow path. In principle, the LPP is designed for optimal operation in the condensation mode which is marked by the letter *K*. This mode provides maximum efficiency. The cogeneration modes which are marked by the letter *T* have a very small degree of expansion, hence, the efficiency of the LPP at the cogeneration modes is very low. The efficiency of cogeneration mode often has a negative value in the ventilation mode due to the LPP does not perform the work.

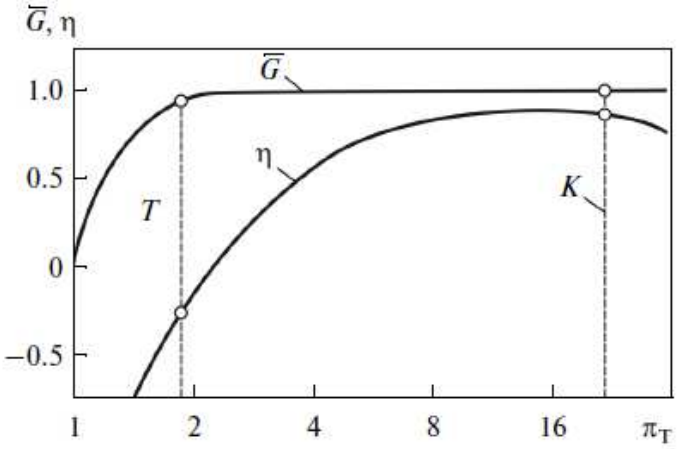

Figure 2.4 Characteristic of low-pressure part (LPP) operation in a cogeneration system [2]

2.2 Control mechanism

The performance of a turbine when operating at different loads depends on the method used for controlling the supply steam to the turbine, so that the rotation will remain sensibly constant, irrespectively of the load. A variety of methods can be used to regulate the steam flow through turbines. The choice of a control type is influenced by the nature application of the driven load and the need for power and process heat. In this section, some methods of the control of steam turbines are presented.

2.2.1 Throttle control

This control is performed by getting down the pressure of the steam through the closing a valve in the entrance of the turbine, the process is called throttle. The main purpose of the control is to reduce the mass flow rate. The schematic arrangement of throttle control is shown in Fig. 2.5a. Here, SV is a quick-closing safety valve and RV is regulating valve component. A quick-acting safety valve is always arranged on the entering of the turbine, which gets self-closed by the command of limit switches. It can be considered that the pressure is held upstream of the turbine at a constant value of p_{A0}, thus, it should be

Die approbierte gedruckte Originalversion dieser Dissertation ist an der TU Wien Bibliothek verfügbar.
The approved original version of this doctoral thesis is available in print at TU Wien Bibliothek.
TU Bibliothek Your knowledge hub WIEN

reduced to a value of p_A. Since during the throttling process h_{A0} = constant and based on STODOLA's cone law, the relationship between required parameters is described as

$$\frac{\dot{m}}{\mu A_V} = \sqrt{\frac{p_{A0}}{v_{A0}}}\,\xi\left(\frac{p_A}{p_{A0}}\right) \tag{2. 2}$$

where $\dot{m}$, μ, v_{A0}, A_V and $\xi\left(\frac{p_A}{p_{A0}}\right)$ denotes each of steam flow rate, the discharge coefficient, the specific volume of steam, the throat area of the control valve and pressure ratio function, respectively.

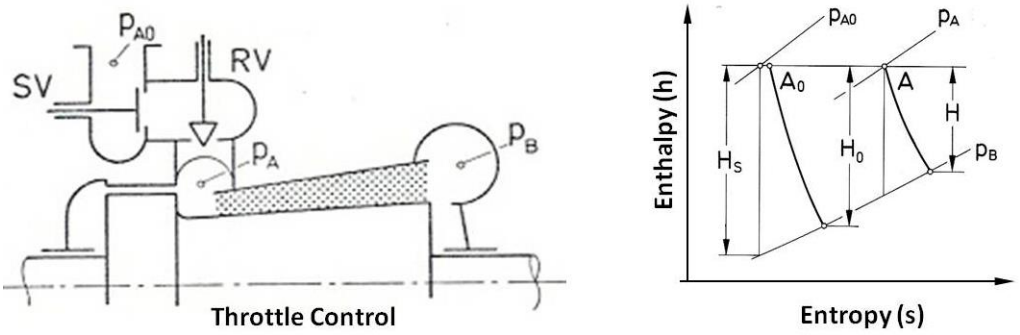

(a) (b)

Figure 2.5 (a) Arrangement of throttle control; (b) Change of the state on the h-s chart for a throttling control [49]

As the valve is closed, the steam experiences an increasing pressure drop through the governing valve with an increase in entropy and a decrease in availability of energy as shown in the h-s diagram in Fig. 2.5b. During throttling process in the control valve, the starting point of the expansion in the turbine shifts from A_0 to A and the heat reduction in the turbine is decreased from H_0 to H. It may be noted that even when the valve is fully open, there is a drop of pressures. Thus, there is a pressure loss at all loads of the turbine with this kind of regulation.

2.2.2 Nozzle group control

The application of nozzle group control is commonly used in steam turbine units which are operating with a constant pressure before the turbine. Here, the pressure entering the first stage nozzles are constant with load. In this control system, the throttle operations are conducted just to regulate the mass flow rate. Furthermore, it is important to note that the absolute pressure of the steam entering the second stage nozzles is in direct proportion to the mass flow through the turbine.

A typical arrangement of nozzle group control is shown in Fig. 2.6. This arrangement forms multiple partial admissions of a steam turbine, which is well-known as a control

Die approbierte gedruckte Originalversion dieser Dissertation ist an der TU Wien Bibliothek verfügbar.
The approved original version of this doctoral thesis is available in print at TU Wien Bibliothek.
TU Bibliothek Your knowledge hub WIEN

stage. Partial admission is used in the first stage where steam enters the steam turbine through one or several nozzle groups, depending on the turbine load.

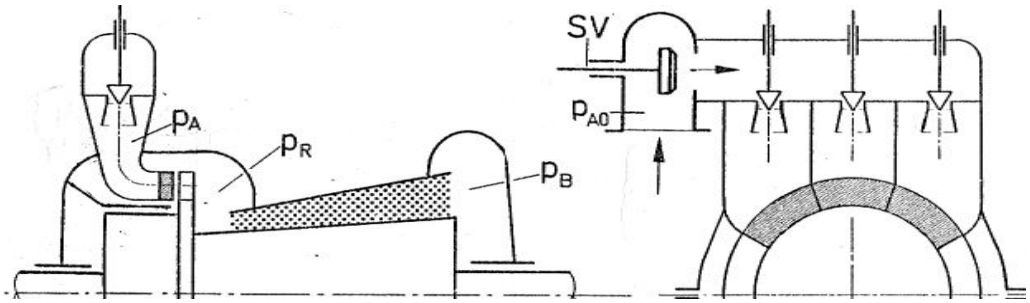

Figure 2.6 Schematic arrangement of three groups for nozzle governing [49]

The relationships between the nozzle exit pressure, mass flow rate and the lines p_{2I}, p_{2II}, and p_{2III}, for one to three numbers of the opened nozzle groups by using three nozzle groups are given by fluid flow diagram in Fig. 2.7a. The expansion in wheel chamber to the pressure of p_R and the expansion in turbine downstream from p_R to p_B for both states with p_{A0} is constant and p_B being constant. In this way, the throttle operations could be made just to a small part of the mass flow rate which corresponds to other operation points of nozzle governing. These points would represent new location between $\dot{m}_I$, $\dot{m}_{II}$, and $\dot{m}_{III}$ depending on the mass flow demand.

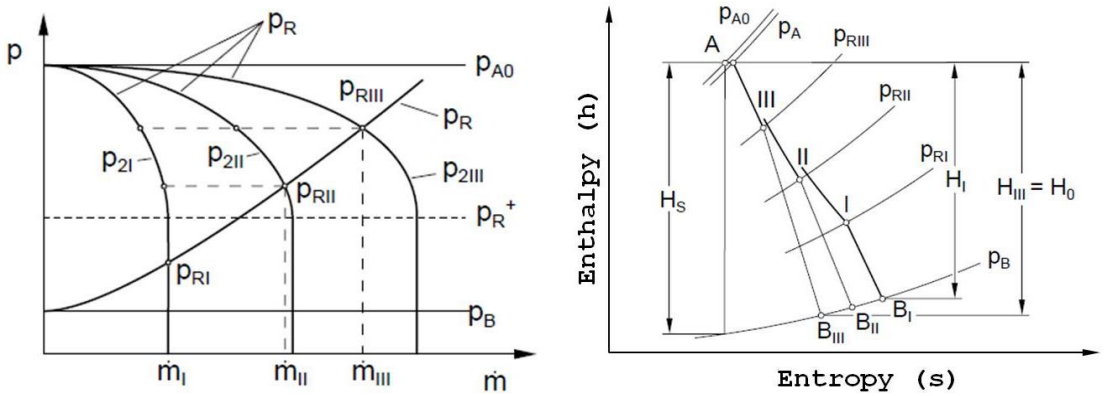

Figure 2.7 (a) Operating points in nozzle group control; (b) Expansion characteristics on the h-s diagram for a nozzle group control [49]

The expansion process with arrangement of three nozzle group control above can be expressed in the h-s diagram as shown in Fig. 2.7b. This process shows the reduction of static pressure in each throttling nozzle and causes drop in pressure at p_{RI}, p_{RII}, and p_{RIII}. In the multistage turbine, again these pressures decrease at p_{BI}, p_{BII}, and p_{BIII}. It should be noted that the significant feature of nozzle group control is that considerably less throttling of steam occurs than if a single nozzle is used.

Die approbierte gedruckte Originalversion dieser Dissertation ist an der TU Wien Bibliothek verfügbar.
The approved original version of this doctoral thesis is available in print at TU Wien Bibliothek.
TU Bibliothek Your knowledge hub WIEN

2.2.3 Adaptive control

The adaptive stage is a new valve concept proposed for the regulating steam capacity of modern extraction turbines with a flexible geometry of the stator blades. This control valve is used to get higher performances with the large capacity turbines, especially to optimize the control stage in a low-pressure part of the turbine. In the traditional control system, it is usually used the control stage mainly regulating valve since the valves are highly reliable, easy to install, and they have a fixed mechanism. However, the extraction of steam within single casing turbines for heating purposes, for example, by employing a valve to control the extraction pressure leads to complex structures which results in a negative impact on the cost, size, and efficiency as well. Thus, it is reasonable to use the adaptive stage, which can regulate the flow capacity through the circumferential passage.

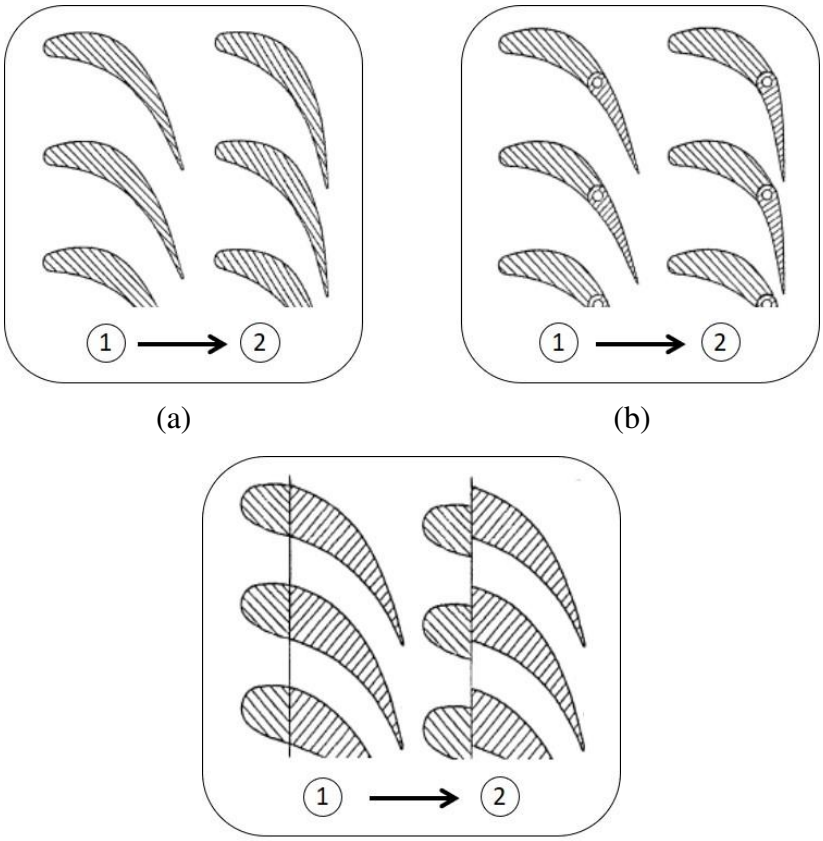

Figure 2.8 Adaptive stage: (a) rotated stator; (b) flap nozzle; (c) throttling nozzle in (1) fully opening, (2) partially closing [24]

Different designs and mechanisms of the adaptive stage have been patented and practically implemented since 1966. Based on the mechanism of the flexible geometry, there are three common types of the adaptive stage in industrial steam turbines: (a) rotated stator (Fig. 2.8a), (b) flap nozzle (Fig. 2.8b) and throttling nozzle (Fig. 2.8c). Due to using of each additional component might lead to the problems in a turbine which will force a shutdown

Die approbierte gedruckte Originalversion dieser Dissertation ist an der TU Wien Bibliothek verfügbar.
The approved original version of this doctoral thesis is available in print at TU Wien Bibliothek.
TU Bibliothek Your knowledge hub WIEN

for maintenance and inspection, thus it is pursued a simple design of adaptive stage hereby the flow energy is preserved. It is preferred from the viewpoint of reduction of technical problems which may cause efficiency decreasing. The basic working principles and a short review of state of the art for adaptive controls are given in section 2.3.

2.3 Adaptive control stage

2.3.1 Rotated stator

The rotated stator concept is based on the variable stagger with the mechanism of varying the completely rotated blade such that change the throat area of the flow passage, is preserving the continuity of the blade shape and varying throats according to changes of flow rate in the passage, thereby changing steam flow capacity. To change the stagger angle of the nozzle blade for different flow conditions, the nozzle blades must be pivoted at different operating positions. For this case, the load distribution of the blade depends on the throat opening degree of the nozzle. The rotated stator requires a driving mechanism to enable rotating of nozzles, particularly in diverging enwall/casing contour. This design has industrially implanted and is shown in Fig. 2.9.

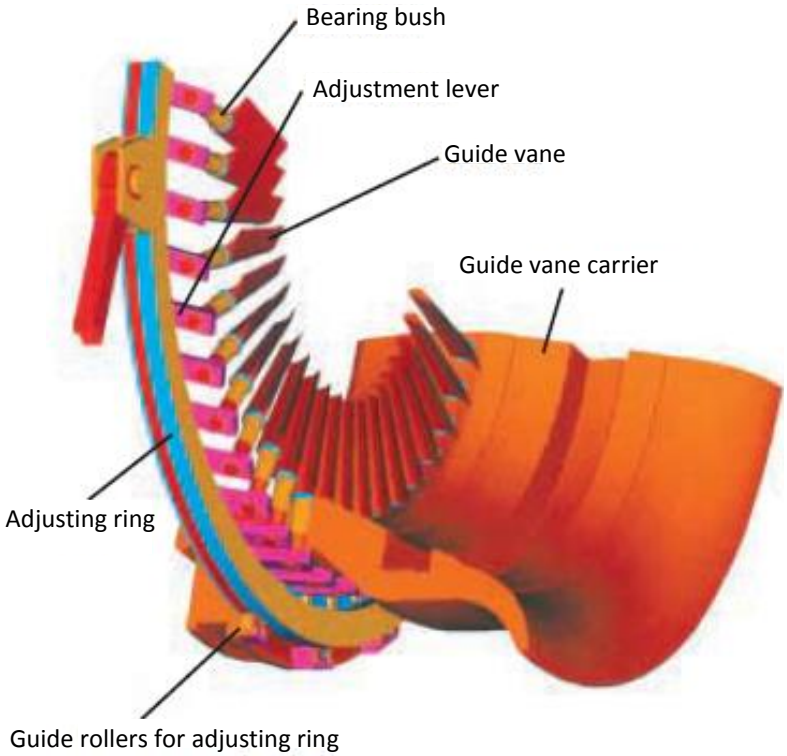

Figure 2.9 Rotated stator for adaptive stage of extraction steam turbines [30]

The working principle of this concept can be explained as follows. As the stagger angle of the nozzle blade increases, the expansion ratio of the nozzle blade decreases, therefore, the

Die approbierte gedruckte Originalversion dieser Dissertation ist an der TU Wien Bibliothek verfügbar.
The approved original version of this doctoral thesis is available in print at TU Wien Bibliothek.
TU Bibliothek Your knowledge hub WIEN

throat flow area of the nozzle increases. Therefore, the mass flow rate of the turbine stage increases, and the nozzle works at large opening position. On the contrary, as the stagger angle of the nozzle decreases, the expansion ratio of the nozzle increases, thus, the throat area of the nozzle decrease. Hence, the mass flow rate of the turbine stage decreases, and the nozzle works at the small opening position. Lampart and Puzyrewski [27] tested this type of adaptive stage by conducting a series calculation in a range of change of stator blade stagger angle. The results were found that the enthalpy losses of adaptive stage were significant decreased, especially in downstream stages. Moreover, it was shown that power in the stage was sufficiently great increased, particularly in the multi stages.

2.3.2 Flap nozzle

The purpose of this concept is to divide the nozzle into the fixed part leading edge and the movable part trailing edge at its pivoting axis as illustrated in Fig. 2.10. This concept with rotated trailing edge part, which is called a flap nozzle, it keeps the continuity of shape of the blade profile even at very large degrees of closing, but their geometrical construction is more complex. Through a proper mechanical design, the trailing edge part could be rotated to change the flow passage as well as ensure the flow rate adjustment capability at different operating conditions. Puzyrewsky et al. [35] suggested that the design of the flap nozzle should has section shapes with a higher pitch to chord ratio to reduce the number of shapes in the entire diaphragm. Furthermore, through a proper pitch chard ratio, this condition can improve the stage efficiency at the design point.

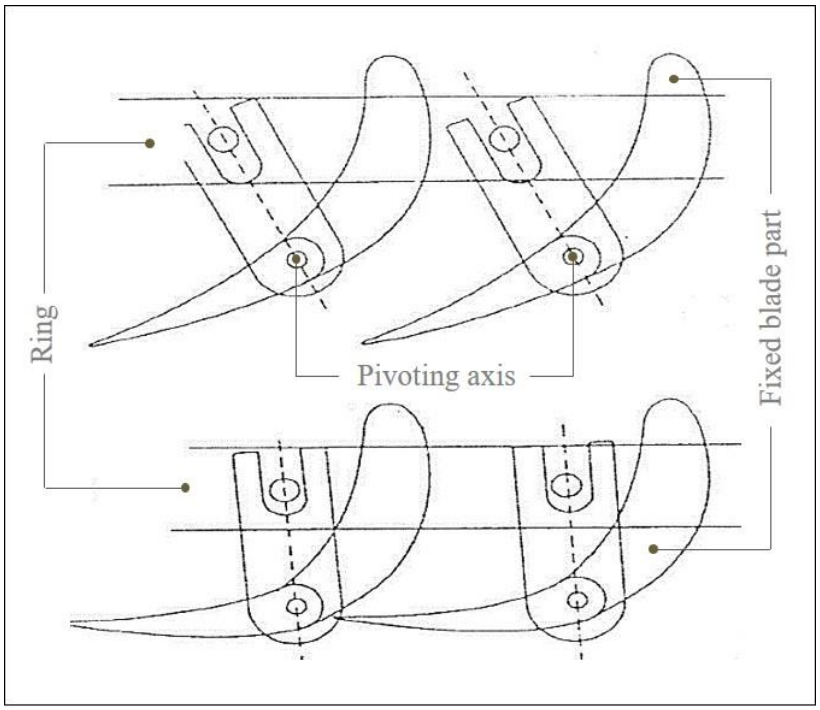

Figure 2.10 Flap nozzle for adaptive stage of extraction steam turbines [35]

Die approbierte gedruckte Originalversion dieser Dissertation ist an der TU Wien Bibliothek verfügbar.
The approved original version of this doctoral thesis is available in print at TU Wien Bibliothek.
TU Bibliothek Your knowledge hub WIEN

2.3.3 Throttling nozzle

Another typical design of an adaptive stage is a nozzle with adjustable geometry of the leading-edge part and the fixed part trailing edge as shown in Fig. 2.11 that well known as throttling nozzle. The profiles with the throttling nozzle usually have the low pitch to chord ratio and blunt leading edge. It results from the requirement to cover the distance of flow channel when closing the flow through the stage. The blade-to-blade passage is narrow and has a nearly constant width starting from the inlet of the passage. When partial closing the leading edges thus the high losses occur.

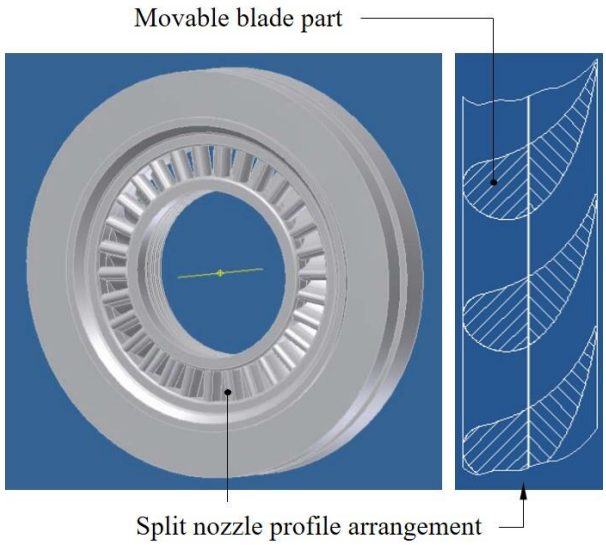

Figure 2.11 Throttling nozzle for an adaptive stage of extraction steam turbines [1]

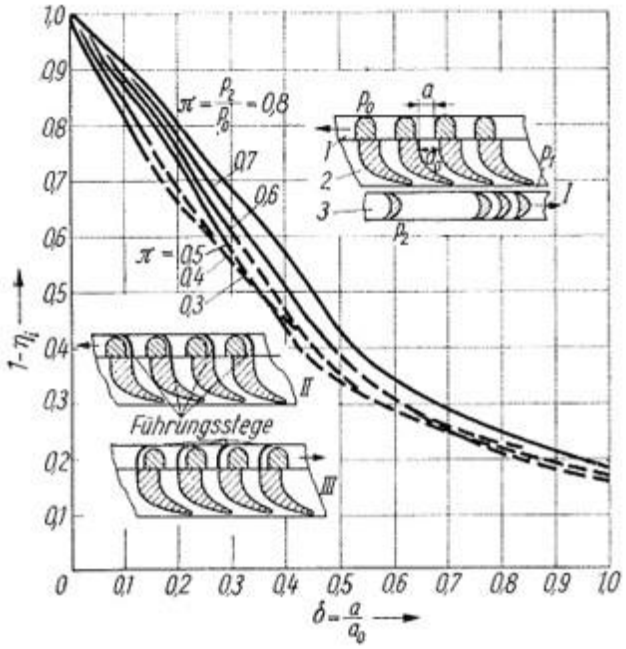

Figure 2.12 Dependence of losses in a stage with a throttling nozzle [12]

Die approbierte gedruckte Originalversion dieser Dissertation ist an der TU Wien Bibliothek verfügbar.
The approved original version of this doctoral thesis is available in print at TU Wien Bibliothek.

One of the earliest investigations on the throttling nozzle is that reported by Deych and Troyanovskiy in 1964 [12]. They carried out a series of experiments on such valves under static conditions. Laboratory work was performed on a rotary diaphragm of the turbine plant which is equivalent to single valve steam distribution. It consists of a rotary ring and a stationary diaphragm with a nozzle blade. As shown in Fig. 2.12, the main result was found that the decrease in the degree of opening could cause the cascade losses intensely increase. A considerable increase in the efficiency of a regulating stage with solid throttle and rotary diaphragm may be reached by the application of deflectors which cover the angle on the concave surface with partial openings. It was also found that a decrease of the losses in the throttle with the application of deflectors leads to an increase of the kinetic energy in the nozzle cascade, which is employed on the moving cascade.

Two main types of rotary valves used in the extraction steam turbine, i.e. axial and radial types are described in the following:

- **Axial rotary valve:** This kind of adaptive valve is constructed so that the coming steam from the high-pressure stage of the turbine flows directly into the valve. This valve can be implemented as a throttle control as well as nozzle group control. All the flow cross-section can be opened and closed simultaneously by throttle controlling, however by increasing the numbers of profile discontinuities which caused by the closing process, the throttling effect on the total mass flow is affectedly applied.

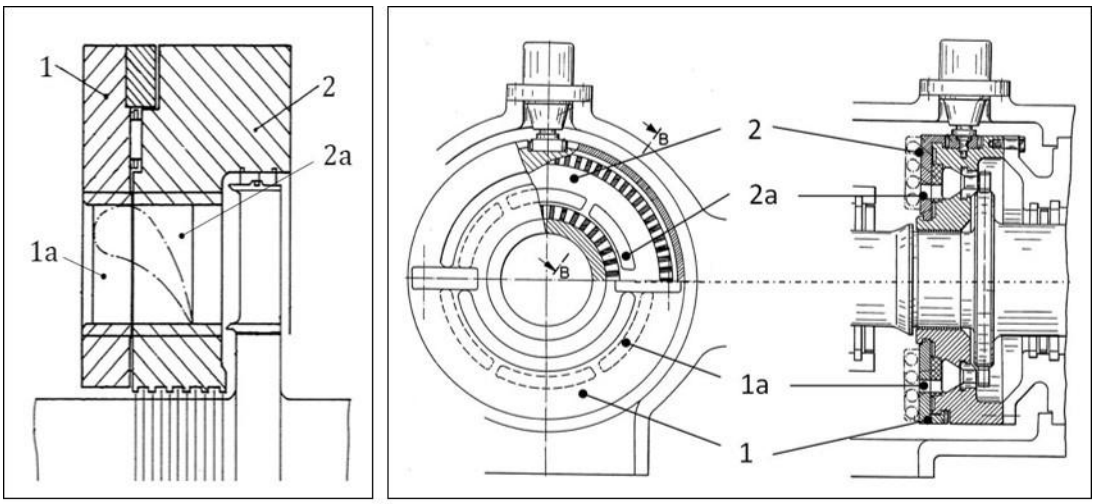

(a) (b)

Figure 2.13 Axial rotary valves (a) for throttling [15]; (b) for nozzle group control [14]

Geist and Jürke [15] have designed and patented a concept of an axial rotary valve for throttling as illustrated in Fig. 2.13a. The main components of the valve consist of a rotary ring (1) and an immovably fixed ring (2) with the respective flow channels (1a) and (2a). Through a mechanism of the rotation of rotary ring (1) from the neutral position, the coverage of flow channel in the fixed ring (2a) increases which leads to reducing of the mass flow rate.

Die approbierte gedruckte Originalversion dieser Dissertation ist an der TU Wien Bibliothek verfügbar.
The approved original version of this doctoral thesis is available in print at TU Wien Bibliothek.
TU Bibliothek Your knowledge hub WIEN

For a nozzle group control, Geist [14] developed and patented a concept of an axial rotary valve as shown in Fig. 2.13b. In this concept of the valve, the flow cross-sections are staggered with the cut blades are not displaced against each other, but through one slider, the separated nozzle channels are completely or partially opened. The rotary ring (1) is provided with at least two opposite radial control slots (1a). The underlying channel body (2) has various channel inputs (2a) which are positioned on the same orbits as the control slots. This valve would be closed through completely rotation of 180^{o} if the two orbits are in different radial distances.

- **Radial rotary valve:** The application of this kind of adaptive stage can also be used for throttle control stage or nozzle group control system. Some designs of such valve have been introduced and industrially used. In this kind valve, the steam flow is radially passed and regulated. Speicher and Mietsch [43] have proposed this concept of radial rotary valve for throttling nozzle as shown in Fig. 2.14a.

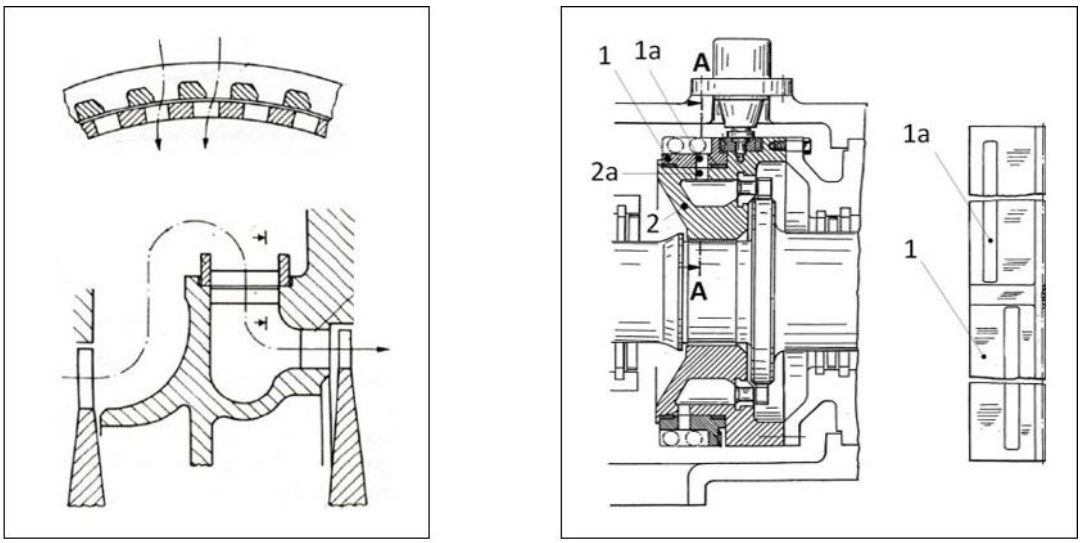

(a) (b)

Figure 2.14 Radial rotary valves (a) for throttling [43]; (b) for nozzle group control [14]

Figure 2.14b is a sample of a radial rotary valve proposed and patented by Geist [14] for nozzle group control. Here, control slots with axial offset are observed in the rotary ring (1). Like Fig. 2.13b, the channel body (2) involves several channel inputs again with side by side arrangement (2a) which are opened according to valve position. The control direction of both control slots could be rotated as 180^{o} so that it can be used for a completely closing mechanism.

In the present study, a simple design of throttling nozzle as representative of an axial rotary valve is defined and studied experimentally in a linear cascade wind tunnel. The details of geometry and dimension for the throttling nozzle are given in section 3.1.

Die approbierte gedruckte Originalversion dieser Dissertation ist an der TU Wien Bibliothek verfügbar.
The approved original version of this doctoral thesis is available in print at TU Wien Bibliothek.
TU Bibliothek Your knowledge hub WIEN

2.4 Performance of axial turbine

2.4.1 Classification of the losses

The losses in the turbomachines are generated from several sources and can be classified by their origin that therefore in general well known as a profile loss, a secondary/endwall loss, and a tip-leakage loss. These losses can be influenced by many parameters such as incidence, turbulence intensity, inlet boundary layer, blade profile, and blade-endwall configuration. These losses are reviewed as follows

- **Profile/pressure loss**. The loss is associated with the two-dimensional cascade which arises from the growth of the boundary layer, the surface friction and blockage effects, usually well away from the end walls. The loss caused by a trailing edge and the wake shed from it is usually included as profile loss. Hoheisel et al. [19] studied the effect of freestream turbulence and pressure gradient on the pressure loss for several turbine cascades. It was found that the type of the velocity distribution on the suction surface was of great importance in view of total pressure losses. The aft-loaded type with a limited rearward deceleration yields low losses. At freestream turbulence intensity, Tu > 2 %, this aft-loaded velocity distribution leads to lower losses than the front-loaded velocity distribution.
- **Secondary/endwall loss**. The loss is due to viscous effects from the interaction of the endwall and blade boundary layers. This loss is related to the three-dimensional flow structures near the endwall, is defined as the difference between the total blade row loss and the profile/pressure loss. Sharma and Butler [40] proved that this kind loss contributes a 30-50% of the total aerodynamic loss of blade cascade. Sauer et al. [39] investigated the effects of chord length on this loss and found that at velocity ratios near 1.0, the influence of the chord decreases rapidly, while at a ratio of 1.0, the endwall loss is independent of the chord.
- **Tip-leakage loss**. The loss is mostly occurred in the casing-rotors interaction. This loss is caused by the pressure difference that is formed over the blade tip between the pressure and suction sides. The pressure difference across the tip clearance will drive a leakage flow from the high pressure to low pressure side. The tip-leakage flow causes decreasing of blade work since the leakage fluid does not experience the same turning as the primary flow. Bindon [5] measured the development of tip clearance loss in a cascade and identified that tip clearance loss varies linearly with gap size with only 13% of the overall loss arises from secondary flow and of the remaining 87%, 48% is due to suction corner mixing, and 39% is due to internal gap shear.

2.4.2 Loss coefficients

In order to understand the loss relationships of a turbine stage, some basic loss equations are shortly presented. The axial turbine stage comprises a row of fixed blades (stator) and a

Die approbierte gedruckte Originalversion dieser Dissertation ist an der TU Wien Bibliothek verfügbar.
The approved original version of this doctoral thesis is available in print at TU Wien Bibliothek.
TU Bibliothek Your knowledge hub WIEN

row of moving blades (rotor). Typical velocity triangle in the axial steam turbine stage is depicted in Fig. 2.15a. The fluid flow enters the stator with absolute inlet velocity C_0 at inlet flow angle α_0 and accelerates to an absolute exit velocity C_1 at outlet flow angle α_1. From this velocity diagram, the rotor inlet relative velocity W_1, at an inlet angle β_1, is found by subtracting the blade speed U from the absolute velocity C_1. The relative flow within the rotor accelerates to velocity W_2 at an angle β_2 at rotor outlet; the corresponding absolute flow C_2 is obtained by adding the blade speed U to the relative velocity W_2 and generally expressed as

$$\vec{C} = \vec{U} + \vec{W} \tag{2. 3}$$

here $\vec{C}$ is absolute velocity, $\vec{W}$ is relative velocity and $\vec{U}$ is the blade speed along a specific streamline, and normally it is approximately constant between inlet and outlet of a rotor blade, $\vec{U}_1 = \vec{U}_2$.

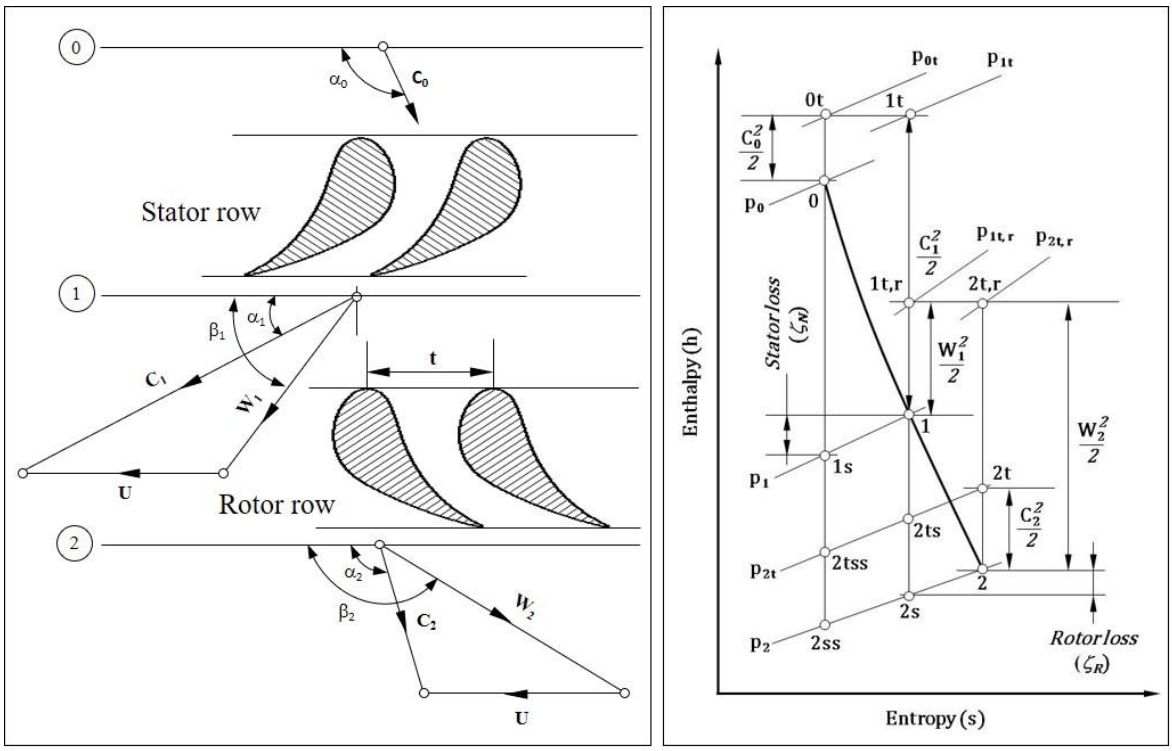

(a) (b)

Figure 2.15 (a) Schematic of velocity triangles; (b) Enthalpy-entropy diagram showing the expansion through a turbine stage

The detailed expansion process of the fluid flow in the turbine stage is illustrated in the h-s diagram as shown in Fig. 2.15b. The x-axis stands for entropy (s), the y-axis is enthalpy (h) and the constant pressure line is the expansion from each other with the slope equal to the local temperature (T). Line 0–1 and 1–2 represent the actual expansion and line 0–1s and 1–2s are the ideal expansion.

Die approbierte gedruckte Originalversion dieser Dissertation ist an der TU Wien Bibliothek verfügbar.
The approved original version of this doctoral thesis is available in print at TU Wien Bibliothek.

As drawn in the h-s diagram, a fluid flow is passing through a turbine stage from stator inlet (0) to rotor inlet (1) and out through the rotor to point (2). In the stator, the condition point moves from 0 to 1 and the static pressure reduces from p_0 to p_1. In the rotor row, the absolute static pressure decreases from p_1 to p_2. At the stator inlet the fluid has the static pressure (p_0) and a small absolute velocity (C_0) that give a total enthalpy (h_{0t}) as the sum of static enthalpy (h_0) and kinetic energy ($\frac{1}{2}C_0^2$). In the stator the fluid expands and reaches absolute velocity (C_1) much greater than C_0 but with a moderate relative velocity (W_1). In the rotor the relative velocity increases to a high level W_2 but with low absolute velocity (C_2) so that a total relative enthalpy (h_{tr}) is constant in the rotor.

Losses in axial turbomachines are usually expressed in terms of loss coefficients. That is done by relating the loss of enthalpy due to irreversibility to the total useful enthalpy drop. It is also general practice to separate the losses between the stator and rotor into two different loss coefficients. Referring the h-s diagram in Fig. 2.15b, loss coefficient in the stator ζ_S and the rotor ζ_R are defined as

$$\zeta_S = \frac{(h_1 - h_{1s})}{(h_{0t} - h_1)} \quad \text{and} \quad \zeta_R = \frac{(h_2 - h_{2s})}{(h_{2t,r} - h_2)} \tag{2.4}$$

with h_{1s} and h_{2s} are the final enthalpies of an isentropic expansion to the same final static pressure as the real process in the stator and the rotor respectively.

The loss coefficient also can be determined in terms of exit kinetic energy from each blade row. Referring to the h-s diagram in Fig. 2.15b, the enthalpy loss coefficient referred to the isentropic velocity is defined as

$$\xi_S = \frac{(h_1 - h_{1s})}{(h_{0t} - h_{1s})} = 1 - \frac{C_1^2}{C_{1s}^2} \tag{2. 5}$$

and

$$\xi_R = \frac{(h_2 - h_{2s})}{(h_{2t,r} - h_{2s})} = 1 - \frac{W_2^2}{W_{2s}^2} \tag{2. 6}$$

with ξ_S and ξ_R are kinetic energy loss coefficients in stator and rotor, respectively. The square term of velocity in the right side of equations (2.5) and (2.6) represent the kinetic energy coefficient in stator and rotor respectively.

The relationships between enthalpy loss coefficients in equations (2.4) and kinetic energy losses of equations (2.5) and (2.6) can be expressed as

$$\xi_S = \frac{\zeta_S}{1 + \zeta_S} \quad \text{and} \quad \xi_R = \frac{\zeta_R}{1 + \zeta_R} \tag{2.7}$$

where ζ_S and ζ_R represent stator and rotor loss coefficient respectively.

Die approbierte gedruckte Originalversion dieser Dissertation ist an der TU Wien Bibliothek verfügbar.
The approved original version of this doctoral thesis is available in print at TU Wien Bibliothek.
TU Bibliothek Your knowledge hub WIEN

Based on the h-s diagram in Fig. 2.15b, the slope of a constant pressure line is $(\partial h/\partial s)_p = T$, and from equations (2.4), therefore entropy loss coefficient is

$$\zeta_S = \frac{T_1\,(s_1 - s_0)}{\frac{1}{2}C_1^2} \quad \text{and} \quad \zeta_R = \frac{T_2\,(s_2 - s_1)}{\frac{1}{2}W_2^2}. \tag{2.8}$$

In a stationary system, it implies the only loss production mechanism is via entropy generation. Considering the flow is an ideal gas, the change in entropy is calculated based on Gibb´s equation (A10). Since total temperature is constant for this case, hence entropy change is only a function of the change in total pressure and therefore the change of entropy is calculated by using equation (A11).

Denton [11] used the total pressure loss coefficient to quantify the loss through a turbine stage in his studies. This coefficient is used primarily because of the ease of determining total pressure loss from cascade testing. This loss coefficient is defined as

$$Y_S = \frac{(p_{0t} - p_{1t})}{(p_{1t} - p_1)} \quad \text{and} \quad Y_R = \frac{(p_{1t,r} - p_{2t,r})}{(p_{2t,r} - p_2)} \tag{2.9}$$

with Y_S is pressure loss coefficient in the stator and Y_R is pressure loss coefficient in the rotor. For a low speed cascade and incompressible flow, it is found that $Y_S = \zeta_S$ and $Y_R = \zeta_R$. The detailed derivation of these relationships was given by Horlock [20].

2.4.3 Efficiencies of turbine

In order to study the overall turbine performance, it is also essential to define the turbine efficiency as an extension the definitions of loss above. The total-to-total efficiency should be used in multi-stage turbines where the exit velocity from a stage is not lost. The total-to-total efficiency, η_{tt} of a turbine stage is defined as

$$\eta_{tt} = \frac{h_{0t} - h_{2t}}{h_{0t} - h_{2tss}}. \tag{2.10}$$

In the total-to-total efficiency, it is considered that the kinetic energy $\frac{1}{2}C_2^2$ is possible to recover in a later stage. Particularly for a normal stage, the flow conditions are identical, i.e. $C_0 = C_2$ and $\alpha_0 = \alpha_2$ (flow angles). It implies $C_2 = C_{2ss}$ as a reasonable approximation, and the equation (2.10) for the total-to-total efficiency becomes

$$\eta_{tt} = \frac{h_0 - h_2}{h_0 - h_{2ss}} = \frac{h_0 - h_2}{(h_0 - h_2) + (h_2 - h_{2s}) + (h_{2s} - h_{2ss})}. \tag{2.11}$$

State 2ss refers to the condition when the flow is isentropic through the entire rotor-stator turbine stage.

Die approbierte gedruckte Originalversion dieser Dissertation ist an der TU Wien Bibliothek verfügbar.
The approved original version of this doctoral thesis is available in print at TU Wien Bibliothek.
TU Bibliothek Your knowledge hub WIEN

The slope of a constant pressure line on the h-s diagram is $(\partial h/\partial s)_p = T$. Thus, for a change of enthalpy in a constant pressure process, $\Delta h = T\Delta s$ and, hence, the enthalpy difference in stator is

$$h_1 - h_{1s} \cong T_1(s_1 - s_{1s}) \tag{2.12}$$

and the difference of enthalpy in rotor is

$$h_{2s} - h_{2ss} \cong T_2(s_{2s} - s_{2ss}) \tag{2.13}$$

from the h-s diagram in Fig. 2.15b, that $s_{2s} - s_{2ss} = s_1 - s_{1s}$, therefore the equation (2.12) and (2.13) can be combined to obtain

$$h_{2s} - h_{2ss} = \left(\frac{T_2}{T_1}\right)(h_1 - h_{1s}). \tag{2.14}$$

The influences of irreversibility through the stator and rotor are defined by the differences in static enthalpies, $(h_1 - h_{1s})$ and $(h_2 - h_{2s})$ respectively. Based on equations (2.4), it can be rearranged as

$$h_1 - h_{1s} = \frac{1}{2}C_1^2\zeta_S \quad \text{and} \quad h_2 - h_{2s} = \frac{1}{2}W_2^2\zeta_R \tag{2.15}$$

then, combining equation (2.11) with equation (2.14) and (2.15) supplies the total-to-total efficiency as

$$\eta_{tt} = \frac{2(h_0 - h_2)}{2(h_0 - h_2) + \left[\zeta_S c_1^2\left(\frac{T_2}{T_1}\right) + \zeta_R w_2^2\right]}. \tag{2.16}$$

Other term of total-to-total efficiency can be expressed as follows: from equation (2.10), total-to-total efficiency is

$$\eta_{tt} = \frac{(T_{0t} - T_{2t})}{(T_{0t} - T_{2tss})}. \tag{2.17}$$

from equation (A.10) can be rearranged as

$$\left(\frac{T_{2t}}{T_{0t}}\right)^{\frac{C_p}{R}} = \left(\frac{p_{2t}}{p_{0t}}\right)e^{\left(\frac{\Delta s}{R}\right)} \tag{2.18}$$

since $R = c_p - c_v = 287$ J/(kg. K), $k = c_p/c_v = 1.4$, and thus $R/c_v = k - 1$, for air: $c_p = 1004$ (J/kg. K), and the equation (2.17) becomes

$$\frac{T_{2t}}{T_{0t}} = \left[\left(\frac{p_{2t}}{p_{0t}}\right)e^{\left(\frac{\Delta s}{R}\right)}\right]^{\frac{k-1}{k}}. \tag{2.19}$$

Die approbierte gedruckte Originalversion dieser Dissertation ist an der TU Wien Bibliothek verfügbar.
The approved original version of this doctoral thesis is available in print at TU Wien Bibliothek.
TU Bibliothek Your knowledge hub WIEN

Returning to the definition of total-to-total efficiency in equation (2.10), the total-to-total efficiency therefore is related to the change of entropy $s_{2t} - s_{0t} = \Delta s$ and is expressed as

$$\eta_{tt} = \frac{1 - \left[\left(\frac{p_{2t}}{p_{0t}}\right) e^{\left(\frac{\Delta s}{R}\right)}\right]^{\frac{k-1}{k}}}{1 - \left(\frac{p_{2t}}{p_{0t}}\right)^{\frac{k-1}{k}}}. \tag{2.20}$$

Efficiency of the turbine also can be expressed in the term of total-to-static efficiency. This efficiency is used when the exit velocity is not recovered, such as in the single stage turbine and the last stage in a multi-stage turbine. Here assumes that all the kinetic energy in the exhaust flow will be lost. An example is in the last stage of a turbine where the exhaust is blown out into the surrounding environment, and all the kinetic energy that the diffuser cannot recover to pressure will be lost. Then, total-to-static efficiency, η_{ts} of the turbine is defined and calculated as

$$\eta_{ts} = \frac{h_{0t} - h_{2t}}{h_{0t} - h_{2ss}}. \tag{2.21}$$

Another term of the turbine efficiency is static-to-static efficiency. In the static-to-static efficiency, of course the static condition at both inlet and outlet is used. This static-to-static efficiency, η_{ss} is calculated as

$$\eta_{ss} = \frac{h_0 - h_2}{h_0 - h_{2ss}}. \tag{2.22}$$

For the case of a multi-stage turbine with repeating stage, meaning that both the inlet and outlet velocity is the same to both magnitude and direction, there will be no difference between total-to-total and static-to-static efficiency.

2.5 Flow fields in a turbine cascade

2.5.1 Two-dimensional flow field

In the design process, the flow of axial turbines usually is assumed to be axisymmetric and is restricted to concentrate streamtubes. It means that the flow through the blade rows is assumed to be two-dimensional, which means that the radial component of flow velocity is zero. This flow condition is usually occurred at midspan where radial effect is ignored. The main feature of midspan flow downstream of blade cascade is the formation of wakes. The wake arises from viscous effects on the blade boundary layers and involves a momentum deficit in the exit flow field. This wake has direct impact on acoustical properties of noise and mechanical vibration of turbomachines. Moreover, it produces the loss in efficiency due to an energy dissipation of the mixing of the wake with freestream.

Die approbierte gedruckte Originalversion dieser Dissertation ist an der TU Wien Bibliothek verfügbar.
The approved original version of this doctoral thesis is available in print at TU Wien Bibliothek.
TU Bibliothek Your knowledge hub WIEN

Many studies have been made to aid in understanding the behavior of wakes in the turbine cascades. Ramachandran et al. [37] measured experimentally the turbulent wake behind a cascade of `S` shaped profile at turbine and pump conditions. This study showed that the wake half width of the tested profiles and the wake momentum thickness during turbine cascade conditions was lower than that during pump cascade conditions indicating higher total pressure loss for pump. The results also presented that the distribution of turbulence intensities in the wake was asymmetric about the wake centre line.

Raj and Lakshminarayana [36] studied the wake characteristics behind a cascade of airfoils at several incidences. This wake was measured at several axial and transverse locations to study the decay behaviour of the mean velocity and turbulence along streamwise axis. This study found that the wake profiles were nearly symmetrical at a zero incidence as shown in Fig. 2.16 but exhibited appreciable asymmetry with the changes of incidence. Furthermore, it is also seen that the decay of the wake defect was strongly influenced by the downstream variation of the wake edge velocity.

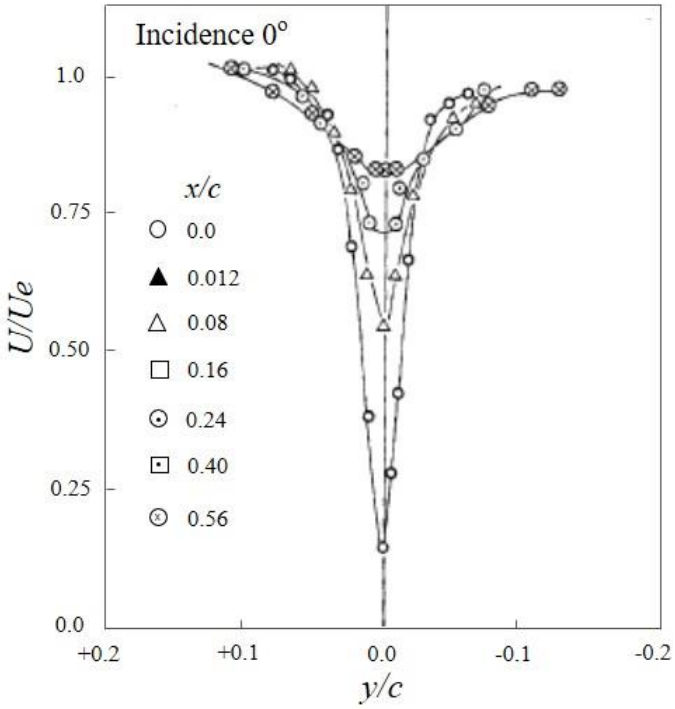

Figure 2.16 Wake profile of mean velocity at zero incidence [36]

Gao et al. [13] investigated experimentally effects of the incidence angles on the wake of turbine cascade and showed that the incidences have a significant influence on the total pressure loss distribution in the wake region. From this study, with the increasing of the incidence, the wake region broadens, and the loss peak increases. They also found that the adopting the aft-loaded blade cascade with thin trailing edge not only increased the base pressure in the wake region, but also reduced the width of the wake.

Die approbierte gedruckte Originalversion dieser Dissertation ist an der TU Wien Bibliothek verfügbar.
The approved original version of this doctoral thesis is available in print at TU Wien Bibliothek.
TU Bibliothek Your knowledge hub WIEN

Luo and Lakshminarayana [29] calculated the flow field through the nozzle passage of a single-stage turbine and compared the wake flow close to the blade trailing edge with the measurement data of Zaccaria and Lakshminarayana [53] and Zaccaria et al [54]. From this study, the calculation was in good agreement with the measurement. The wake profiles inside the endwall boundary layers were predicted better than those near the midspan. It is also observed that the predicted axial velocity profiles were in closer agreement with the measurement data than the predicted total velocity profile.

Sanz et al. [38] measured and calculated the evolution of the wake at several axial planes downstream of turbine cascade. They observed that the dip of the wake in the velocity distribution was very large as the flow transition from the blade boundary layer to the wake. Moreover, they observed that further downstream, the velocity defect decays and the wake spreads due to mixing and exchange of the momentum and energy with freestream flow. The measured wake widens, and the velocity defect reduces to about 10% in the farther downstream, at a distance of about 75% axial chord length. It is also interesting to note that both measurements and calculations show an asymmetry of the wake profile, but on different sides of the wake. The measurements showed a wider wake on the pressure side, which indicates a thicker surface boundary layer on the blade pressure side, whereas the calculations show the opposite trend.

Effects of the wake on the boundary layer behaviour of the turbine cascade at different circumferential positions of two stators were investigated experimentally by Heinke et al. [18]. Using two stators in clocking position, it was shown that a change in total pressure loss coefficient downstream of tested stator of about 11% between the minimum and the maximum value, depending on the clocking position. The loss minimum occurs if the impingement point of the upstream stator wake is shifted by 6% of the pitch toward the suction side of tested stator. The loss maximum occurs if the impingement point is shifted by 25% of the pitch toward the pressure side

2.5.2 Three-dimensional flow field

In fact, the flow in the axial turbines is highly three-dimensional with the variation of flow orientation along the blade span. Three-dimensionality of the flow develops due to the interaction between the blade pressure and endwall boundary layer. Since the endwall boundary layer has lower momentum than the mainstream fluid, once it enters the passage it is turned more strongly by the blade-to-blade pressure difference than mainstream. As the result, the flow is driven towards the convex surface of the blade passage that is well-known as the secondary flow.

Several investigations have been made to understand of complex secondary flow in the turbine cascade. Came and Marsh [8] proposed a theoretical study of secondary flow

Die approbierte gedruckte Originalversion dieser Dissertation ist an der TU Wien Bibliothek verfügbar.
The approved original version of this doctoral thesis is available in print at TU Wien Bibliothek.
TU Bibliothek Your knowledge hub WIEN

developed on the basis of Kelvin's circulation theorem and Helmholtz law to flow through blade cascade and found that total secondary circulation per unit pitch of the flow downstream of blade cascade was always zero when the blades were closely spaced. Until today, the fundamental concept of secondary flow theory is developed from a relatively complex analysis of Horlock and Lakshminarayana [21].

Some studies of secondary flows were reviewed by Langston [28] and Sieverding [41] who provided detailed summaries of the research on secondary flows. The basic features of the flow are now adequate well understood and verified by experimental measurements as well as numerical computations. Although the appearance of secondary flow strength and its structures depend on the individual geometry of the turbine, some of the flow features that are typically seen include the following that is summarized in a physical model describing secondary flows of Langston [28] is depicted in Fig. 2.17. Three kind secondary flows seen in the turbine cascade are passage vortex, horseshoe vortex, and corner/counter-rotating vortex. These vortex structures are reviewed as follows:

- **Passage vortex:** The passage vortex is the most dominant and largest secondary flow structure at the exit of a turbine blade row. The profiles of a turbine blade row cause a turning of the incoming flow and create a pressure gradient across the blade to blade passage. Under the effect of this pressure gradient the endwall boundary layer of the inlet flow is turned on a smaller radius than the main flow due to its low momentum fluid. As a result, within the passage an endwall cross passage flow from the pressure to the suction side is generated and then rolls up into a passage vortex. As shown in Fig. 2. 18, Wang et al. [47] described that under the action of a cross-passage pressure gradient, the pressure side leg of the horseshoe vortex migrates towards the suction surface of the blade. Consequently, the pressure side leg of the horseshoe vortex entrains low momentum fluid from the endwall boundary layer to form the passage vortex. The growth of passage vortex is amplified by a streamwise adverse pressure gradient, following the suction peak inside the passage. It ultimately reaches the suction surface of the adjacent blade and shows a strong interaction with the two-dimensional blade-surface boundary layer.
- **Horseshoe vortex:** The strong interaction between the inlet boundary layer on the endwalls and the blade leading edge causes the formation of the three-dimensional separation in the form of saddle point upstream of blade leading edge. This interaction results the so-called horseshoe vortex forms between the blade leading edge and the separation saddle point. At the upstream leading edge, the boundary layer rolls up into a system of two counter-rotating vortices that pass along each side of the leading edge. The pressure side leg of the horseshoe vortex has the same sense of rotation as the passage vortex. Both vortices merge within the passage, transfer across the passage towards the adjacent blade and appear as one vortex downstream of the profile. The suction side leg of the horseshoe vortex stays close to the blade and then travels up the suction surface. Hah [17] analysed and predicted that the centre of flow motions was found further from the blade suction surface. Using flow visualization method, Wang et

Die approbierte gedruckte Originalversion dieser Dissertation ist an der TU Wien Bibliothek verfügbar.
The approved original version of this doctoral thesis is available in print at TU Wien Bibliothek.
TU Bibliothek Your knowledge hub WIEN

al. [47] described that inlet flow encounters an adverse pressure gradient in streamwise direction ahead of the blade leading edge, as a result, the inlet boundary layer rolls up at the saddle point of separation to form a horseshoe vortex as depicted in Fig. 2.18. This horseshoe vortex consists of a pressure side leg and suction side leg and these vortices develop in size and strength inside the passage under the effects of tangential and radial pressure gradient and freestream pressure gradient.

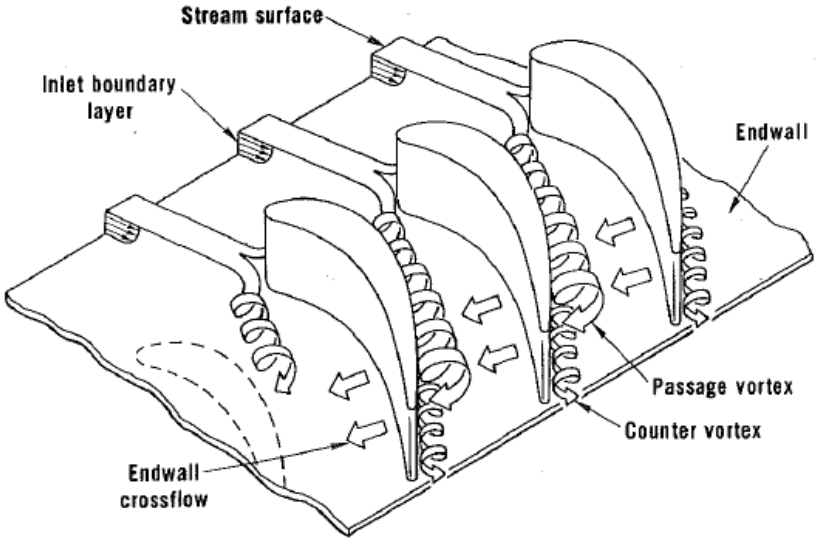

Figure 2.17 Description of the three-dimensional flows in the turbine cascade [28]

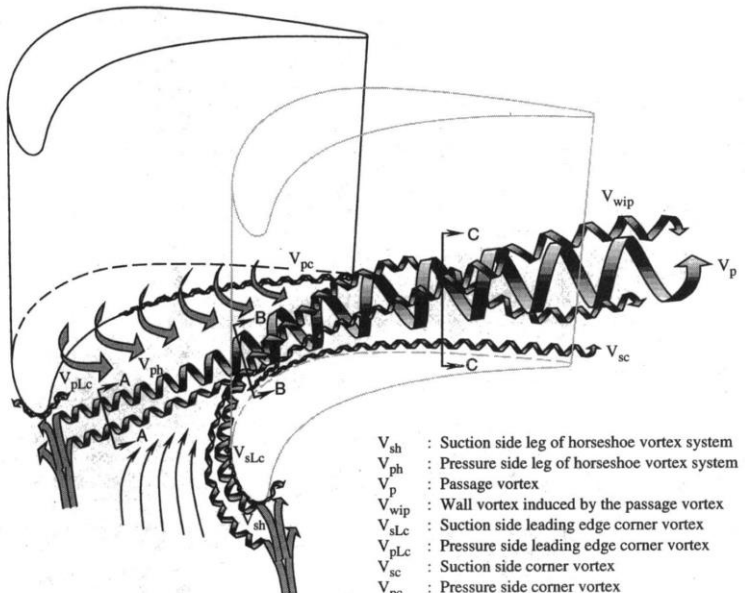

Figure 2.18 Interpretation of the vortex flow pattern in the turbine cascade [47]

- **Corner/counter-rotating vortex:** The corner vortex is a secondary flow rotating in the opposite direction of the passage vortex and formed in the endwall suction side corner

Die approbierte gedruckte Originalversion dieser Dissertation ist an der TU Wien Bibliothek verfügbar.
The approved original version of this doctoral thesis is available in print at TU Wien Bibliothek.
TU Bibliothek Your knowledge hub WIEN

region. This vortex is generated at the intersection region of the endwalls and suction surface of the cascade, due to the interaction process of low momentum boundary-layer fluid flowing into the corner region with the blade suction-side boundary layer. Thus, the corner vortex is rotating about the axis of the passage vortex. The position of the corner vortex compared to a passage vortex may be different depending on the turning and the blade geometry. This feature is relatively very small and that is the reason why it is rarely seen in experimental studies. Wang et al. [47] interpreted that the suction side leg of the horseshoe vortex, has negative sense vorticity and wrap around the passage vortex as depicted in Fig. 2.18. The suction side leg of horseshoe vortex may remain close to the suction side corner or grow towards midspan depending on the strength and the location of passage vortex.

Starting from general description of these flow physics, many papers have been published to understand these complex flows in turbine cascade with a wide range of the influential parameters. Zaccaria and Lakshminarayana [53] and Zaccaria et al [54] studied three-dimensional flow field at the exit of turbine cascade. Using five-hole probe, they measured the nozzle wake, secondary flows and losses. The results showed that strong radial inward flow, which was more pronounced in the wake. Secondary flow vortices were identified to dominate near casing and hub. These structures were on the suction side of the wake and were made up of either the passage vortex or a combination of the passage vortex and the pressure side leg of the horseshoe vortex.

Using pressure and hot wire probes, Perdichizzi [32] tested experimentally effects of Mach number on the flow field of turbine cascade. It was found that as increased Mach number, the passage vortex was found to migrate toward the endwall. Findings also presented that the secondary flow effect was confined in the endwall region. Moreover, at high Mach number both underturning and overturning were found to be smaller than in low velocity flows. The effects of the incidence and solidity on secondary flows downstream of turbine cascade were studied by Perdichizzi and Dossena [33]. The experiments were conducted for incidence from -60^{o} to $+35^{o}$. The important results showed that the level of secondary vorticity and the crossflow at the endwall to be strictly associated to the blade loading taking place in the blade incoming region.

Weiss and Fottner [48] examined experimentally the influence of load distribution on the secondary flow structure of the turbine cascade. It was confirmed that the passage vortex dominates the secondary flows. A corner vortex occurs, and a developed suction side leg of the horseshoe vortex is detectable. Close to the endwall, both cascades become strongly unloaded because of the secondary flows. Recently, Xu and Amano [51] analysed effects of pitch/chord ratio on the secondary flows of turbine blades. The results were seen that the t/b had a strong influence in producing secondary flows and losses. A smaller pitch/chord ratio affects a relatively large separation region on the meridional plane which forces a saddle-point to move forward and develops slowly the suction side vortex core to produce

Die approbierte gedruckte Originalversion dieser Dissertation ist an der TU Wien Bibliothek verfügbar.
The approved original version of this doctoral thesis is available in print at TU Wien Bibliothek.
TU Bibliothek Your knowledge hub WIEN

small total pressure losses in the turbine cascade. However, the small pitch/chord ratio generates more blockage for the flow field thereby strengthens the friction losses.

Gregory-Smith and Cleak [16] studied the effect of inlet turbulence on the secondary flow structure in the turbine cascade. The main conclusion of their studies was that the high inlet turbulence has little effect on the secondary loss of the cascade. High values of turbulent Reynolds stresses were seen in the loss core and vortex region with separation lines on the endwall and suction surface feed loss into the main flow. Using similar cascade model [16], Walsh and Gregory-Smith [46] evaluated experimentally the effects of inlet skew on the flow field and concluded that the inlet skew changes the whole flow field and vorticity distribution at exit from the cascade. Moreover, this inlet skew significantly alters the level of measured losses in the cascade.

Experimentally, Moore and Adhye [31] studied the behavior of secondary flow and the loss mechanism downstream of the linear cascade. Using three-hole and five-hole probe, they found that the secondary flow at each measurement plane was dominated by single large passage vortex, which decayed in strength because of the mixing occurring in the flow. In addition, it was shown that more than one-third of the losses were found to occur downstream of the blade cascade trailing edge. Benner at al. [3] measured the influence of leading-edge geometry on the secondary losses at the design incidence and suggested that the strength of the passage vortex plays an important role in the downstream flow field and loss behavior. It was also found that the profile loading distribution has a more significant influence on the vortex strength.

Yamamoto [52] studied effect of secondary flow on the loss through a straight turbine cascade. It was found that a weak counter-rotating vortex, the suction-side leg of the horseshoe vortex, appeared at the suction surface/endwall corner upstream of the cascade but had no significant effects on the secondary loss. A high-loss region was found on the endwall near the pressure side inlet region within the cascade, probably caused by the pressure side leg of the leading-edge horseshoe vortex. Moreover, most of the secondary loss produced within the cascade was due to the interaction of passage vortices with the suction surface downstream throat of the cascade.

Die approbierte gedruckte Originalversion dieser Dissertation ist an der TU Wien Bibliothek verfügbar.
The approved original version of this doctoral thesis is available in print at TU Wien Bibliothek.
TU Bibliothek Your knowledge hub WIEN

3 Experimental facilities and methods

3.1 Cascade geometry

Several the high-pressure blades which have rounded leading edge were used in the experimental measurements. These blades were made of aluminum fabricated by a CNC-machining (a numerically controlled milling machine). Each blade was made with a chord length of 100 mm and a span of 150 mm. Figure 3.1 shows the cross section of the blade profile. The cascade consists of the fixed and moving assembly, two slotted L shape profiles for fitting two assemblies and L shape profiles for connecting the fixed part to the wind tunnel. The blades were fixed at both Plexiglas wall sides by screwing in blind holes and were connected to downstream of the wind tunnel by two L shaped steel profiles. The Plexiglas sidewalls were used to make ease for the observation.

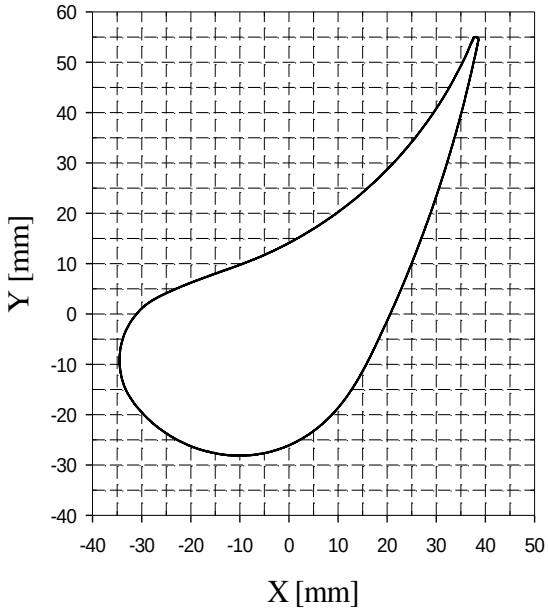

Figure 3.1 T100 profile for the blade cascade

The fixed and moving blades were mounted between two Plexiglas side walls thickness of 20 mm as two separated sections. They could be fitted together using two slotted L shape profiles and nut-bolt for avoiding axial gap effect. A support structure for the blades was made of two adjustable walls at both the top and bottom sides of the inlet channel of the cascade. Thereby in different measurements, purposed closing position of the blades could be reached through manually vertical movement of the moving assembly relative to a fixed one. The flow uniformity in the cascade was achieved using a sufficient number of blades, especially seven blades for this investigation. These seven blades have been arranged in 80 mm pitch distance for this cascade. The definition and nomenclature of the cascade for the current research is depicted in Fig. 3.2.

Die approbierte gedruckte Originalversion dieser Dissertation ist an der TU Wien Bibliothek verfügbar.
The approved original version of this doctoral thesis is available in print at TU Wien Bibliothek.
TU Bibliothek Your knowledge hub WIEN

To obtain the flow characteristics, the total and static pressures of the flow were measured by using pressure probes across downstream measurement plane of the cascade. Therefore, positioning of measurement plane with pitchwise traversing of the probe has an important role in reducing the forgoing measurement errors. Since the probe was exposed to various velocity gradients, depending on its distance from the trailing edge, hence the measurement was made at 0.3b downstream of the cascade to guarantee the smoother deviations in the measurement results. For this investigation, the traversing of probe was being done across one pitch downstream of the turbine cascade.

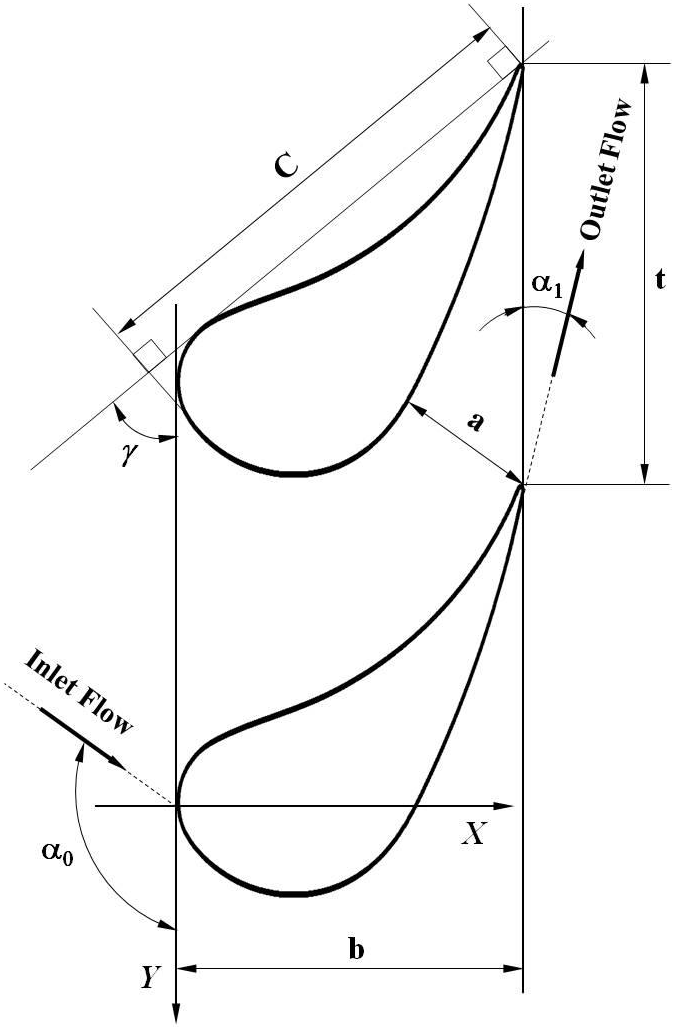

Figure 3.2 Cascade model and nomenclature

The recent study adopts a method of Kariman [23] in determining the profile of blade that is summarized as follows: the first step, 10 different blades were selected by literature survey on the turbine blades because of the consideration of the availability of the blade coordinates. Subsequently, the requirement of suitable profile shape for steam turbines, mainly the possibility for using the blade as a stator blade, was considered. Blades of the desired size and shape were assembled in a straight line according to the cascade required

Die approbierte gedruckte Originalversion dieser Dissertation ist an der TU Wien Bibliothek verfügbar.
The approved original version of this doctoral thesis is available in print at TU Wien Bibliothek.
TU Bibliothek Your knowledge hub WIEN

in two different fixing and moving parts. To assemble the blades, pitch length and stagger angle were defined. The optimization configuration of the cascade geometry is based on the criteria of Zweifel [55]. This criterion is determined as

$$\Psi = 2\left(\frac{t}{b}\right)\sin^2\alpha_1\,(\cot\alpha_0 - \cot\alpha_1) \tag{3.1}$$

where t = pitch length, b = axial chord length, α_0 = inlet flow angle, α_1 = exit flow angle, Ψ = Zweifel coefficient which is between 0.8 and 1.2 for optimum geometry. The dimension of blade cascade is given in Tab. 3.1.

Table.3.1 Dimension of turbine cascade

Axial chord, b	73.05	(mm)
Blade chord, C	100	(mm)
Pitch, t	80	(mm)
Span, l	150	(mm)
Throat, a	26.74	(mm)
Solidity, σ	1.25	(-)
Stagger angle, γ	51.5	(°)
Exit flow angle, α_1	20	(°)
Aspect ratio, AR	1.50	(-)
Pitch/axial chord ratio, t/b	1.1	(-)

Since the pitch length of the proposed geometry should be equal to or less than cut length on the blade to make the complete closing of the flow passage, therefore T100 blade with a pitch length of 80 mm was selected. This blade has a suitable profile turning shape and proper leading-edge radius to fulfill the required condition of flow blockage.

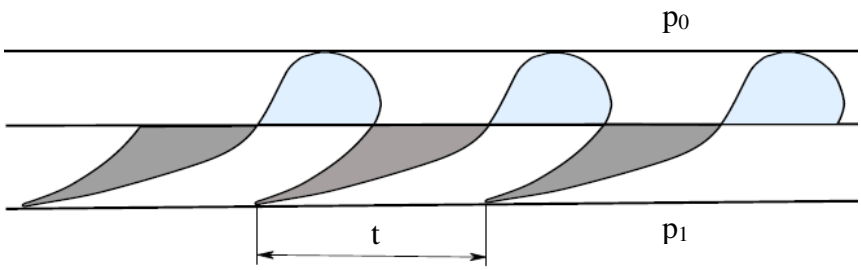

Figure 3.3 Blades cascade in fully closing condition

Cutting line position: The main consideration to determine the cutting line location on the blade is based on compatibility situation between the movable and stationary part in critical state, i.e. the fully closed passage. In other words, the maximum deflection of the fixed and movable part should be identical to justify the mentioned compatibility. The

Die approbierte gedruckte Originalversion dieser Dissertation ist an der TU Wien Bibliothek verfügbar.
The approved original version of this doctoral thesis is available in print at TU Wien Bibliothek.
TU Bibliothek Your knowledge hub WIEN

fixed and movable part of the blade arrangement is shown in Fig. 3.3 for a totally closed position. The pressure difference between upstream and downstream of blades causes axial force which leads to a deflection in both fixed and moving part. Based on the calculation of Kariman [23], the cutting line was located at 0.495 mm from the blade's centroid in the horizontal distance as shown in Fig. 3.4. The details of physical properties for movable part and fixed part of the blade used for the construction of a throttling nozzle are given in Tab. 3.2 and 3.3, respectively.

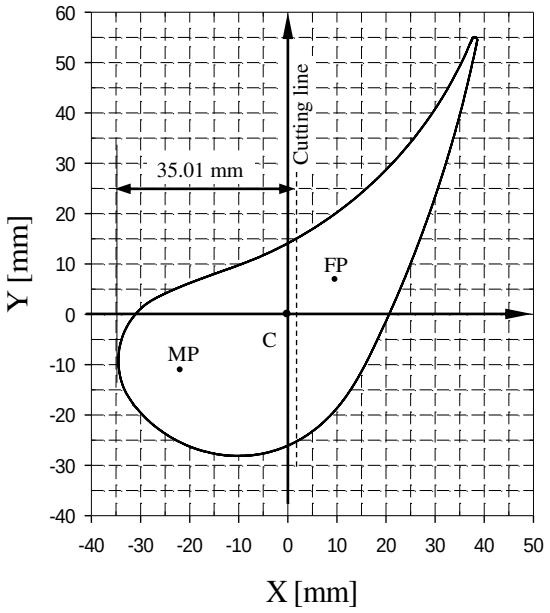

Figure 3.4 Movable part (MP) and fixed part (FP) with position of a cutting line and a centroid (C)

Table 3.2 Physical properties of movable part for nozzle blade

Area (mm^2)	A = 1106.78
Inertia moment at its centroid (mm^4)	I_{xx} = 111767.99; I_{yy} = 96240.23; I_{xy} = -8869.65
Centroid relative to blade origin (mm)	X = -14.49; Y = -8.97
Polar inertia moment at the centroid (mm^4)	I_p = 2080008.22
Angle blade's axes to principal axes (°)	φ = 65.60
Principal inertia moment at the centroid (mm^4)	I_{min} = 92216.46; I_{max} = 115791.75

Table 3.3 Physical properties of fixed part for nozzle blade

Area (mm^2)	A = 1060.28
Inertia moment at its centroid (mm^4)	I_{xx} = 296774.02; I_{yy}= 96240.23; I_{xy} = -134303.98
Centroid relative to blade origin (mm)	X = 15.13; Y = 9.36
Polar inertia moment at the centroid (mm^4)	I_p = 393014.26
Angle blade's axes to principle axes (°)	φ = 63.37
Principal inertia moment at the centroid (mm^4)	I_{min} = 28903.40; I_{max} = 364110.86

Die approbierte gedruckte Originalversion dieser Dissertation ist an der TU Wien Bibliothek verfügbar.
The approved original version of this doctoral thesis is available in print at TU Wien Bibliothek.
TU Bibliothek Your knowledge hub WIEN

3.2 Linear cascade wind tunnel

For this investigation, the measurements were taken at a linear turbine cascade wind tunnel in the thermal laboratory of Institute for Energy Systems and Thermodynamics, Technical University of Vienna. The test rig is an open type circuit wind tunnel with the downstream tunnel is hosted the testing cascade as shown in Fig. 3.5. The wind tunnel has main components involving an axial fan, inlet guide vanes, diffuser, settling chamber, nozzle and a working section at the end of the tunnel exit. An axial fan rotated by an AC motor with a power of 30 kW drives an air flow through filtering systems from the outside building so that pressure rise of the air can reach approximately 15 mbar with the flow rate is about 2.70 m^3/s at the rotational speed of 3000 rpm. Specification blade of the fan at exit plane is 60 mm long and its outer diameter 630 mm. This wind tunnel is also equipped with variable inlet guide vanes to control the volume flow rate. In the measurements, the inlet guide vanes were always positioned in the fully opening condition.

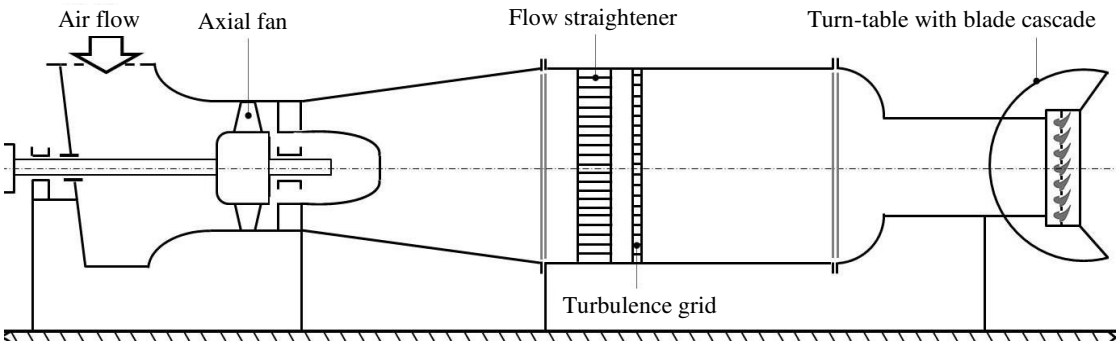

Figure 3.5 Schematic of a subsonic linear cascade wind tunnel

The diffuser with the outer diameter of 1200 mm positioned after the axial fan is used to further homogenize the flow with probably small pressure loss. The air passes through the settling chamber where a flow straightener is placed to generate the air flow uniform. After flowing through a turbulence grid and a settling chamber, the gradually changing from circular to the rectangular cross-section with dimensions of 150 mm x 480 mm occurs and then the air flow entering the nozzle reveals the strong flow acceleration due to reducing the surface area by a ratio factor of about 18.8. The turbulence grid in the settling chamber is used to create freestream turbulence intensity at the exit of contraction. At the end of the downstream channel, the working section is placed. Different inlet flow angles to the blades cascade could be adjusted by free rotation of a turn-table. Especially for this study, the inlet flow angle was kept constant at 90^o if measurement where it is corresponding to a completely vertical alignment of the blades cascade.

The outlet flow parameters were measured in an axial plane placed at 30% axial chord downstream of the cascade as depicted in Fig. 3.6. The inlet flow conditions of the test section were measured at x = -180 mm for static pressure and at x = -225 mm for total

Die approbierte gedruckte Originalversion dieser Dissertation ist an der TU Wien Bibliothek verfügbar.
The approved original version of this doctoral thesis is available in print at TU Wien Bibliothek.
TU Bibliothek Your knowledge hub WIEN

pressure and temperature. This is equal to -1.065b and -1.385b respectively, so it could be expected, that the flow was not influenced by the cascade, which was situated downstream at x = 0. The conditions of the inlet boundary layer of the test section have been measured by Willinger [50], which have a thickness of boundary layer, $\delta = 22.9$ mm, a displacement thickness, $\delta^* = 2.0$ mm, a momentum thickness, $\delta^{**} = 1.5$ mm, shape factor, H = 1.3 and freestream turbulence intensity, Tu = 5%.

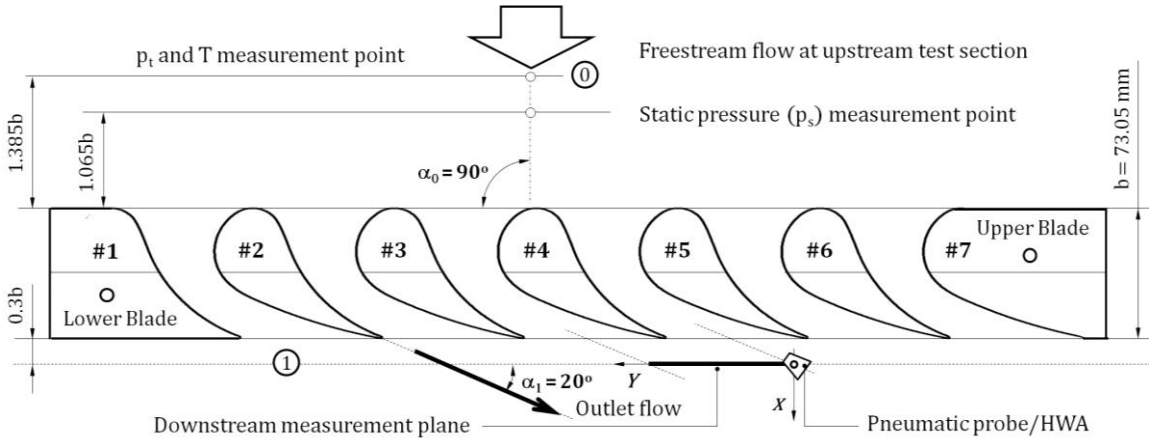

Figure 3.6 Schematic of the throttling nozzle in the linear turbine cascade

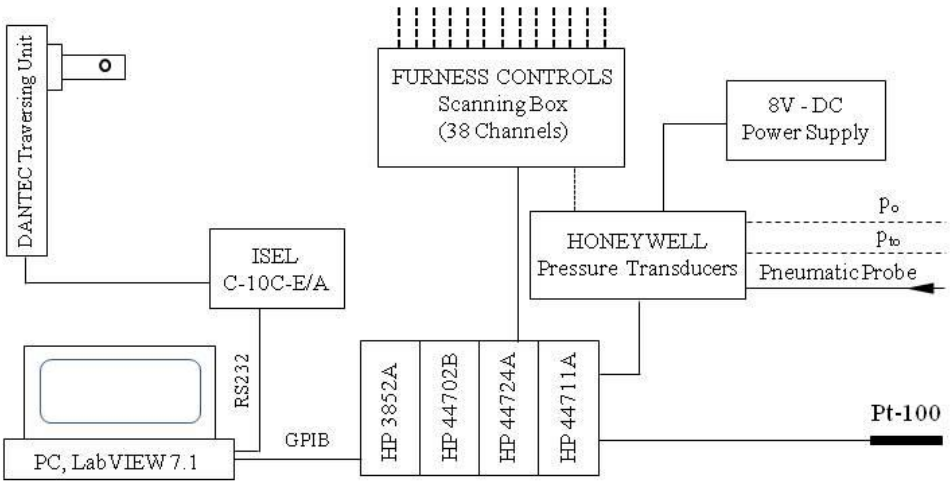

Figure 3.7 Block diagram of measuring instrumentation

Instrumentation: The pressures of purposed measuring points downstream of the blades cascade also static and total pressure of the inflow were done based on piezoresistive differential pressure. For this purpose, the pneumatic probe was connected to the control system by flexible and elastic rubber tubes, which enable a larger displacement and rotation of the pressure probe with no functionality limitations. To define the absolute pressure values, ambient pressure measured by a separate device must be added to the measured values. Switching between the different channels for measuring the pressure by

Die approbierte gedruckte Originalversion dieser Dissertation ist an der TU Wien Bibliothek verfügbar.
The approved original version of this doctoral thesis is available in print at TU Wien Bibliothek.
TU Bibliothek Your knowledge hub WIEN

each selected line of the probe was done by the scanning box (FURNESS CONTROLS) which was controlled through the digital output HP 44724A with 16-channel digital output of the HP 3852A unit. Figure 3.7 illustrates the schematic of the instrumentation.

Pressure transducers require a DC supply voltage of 8 volts, which is ensured by an external power supply. The data acquisition unit HP 3852A, which is controlling the measurement, contains a 13-bit high speed-voltmeter HP 44702B and a 24-channel high speed-multiplexer-unit HP 44711A as well which record the transmitted voltages from resistance thermometer Pt-100 to measure inflow temperature and HONEYWELL pressure sensors. Recorded voltage data are transmitted to the personal computer for processing and converting in pressure values by LabVIEW7.1 program.

Traversing mechanism: A traversing system was used for this linear cascade wind tunnel with an automated mechanism of the DANTEC traversing unit (Fig. B.2b). Traversing device is used to move the pressure probes or hot-wire probe in a parallel way at the exit measurement plane of the cascade. The traversing system arrangement could be moved and mounted at the required downstream position. The change of the probe position above the pitch of the cascade is achieved by an electrically driven stepper motor which is controlled through the ISEL C10C-E/A controlling unit. All controlling components are connected to the PC (personal computer), which controls the whole process by making use of the LabVIEW7.1 program from National Instruments.

Measurement procedures: Current research is aimed to investigate the characteristic of the throttling nozzle that is tested in a linear turbine cascade. Experiments are focused on the measurement plane at 0.30 axial chord length downstream of the cascade. Seven blades were used in the cascade design which was marked up to down from #7 to #1 respectively. In this step, the value of 20^{o} was considered as reference setting angle for probe.

The measurements were conducted in two steps. The first experiment was done in the fully opening condition to investigate the basic flow features of the cascade. Then, the second step was setting the closing position for further measurement. For the closing mechanism, the movable part of the cascade was moved. It was being arranged manually with respect to the fixed part and being set by visual observation of an installed ruler on the Plexiglas side wall. The variations of closing degree (δ) are listed in the following Tab. 3.4.

Table 3.4 Dimension of two closing models and closing degree variation measured

Parameter	Full Opening	CPS	CSS
Pitch, t (mm)	80	80	80
Passage depth at cut-line, a = t/2 (mm)	40	40	40
Closing length, a´ (mm)	0	2, 4, 6, 8, 12	2, 4, 6, 8, 12
Closing degree, δ = a´/a (%)	0	5, 10, 15, 20, 30	5, 10, 15, 20, 30

Die approbierte gedruckte Originalversion dieser Dissertation ist an der TU Wien Bibliothek verfügbar.
The approved original version of this doctoral thesis is available in print at TU Wien Bibliothek.
TU Bibliothek Your knowledge hub WIEN

The closing directions of closing toward pressure side (CPS) and toward suction side (CSS) are schematically illustrated in Fig. 3.8. For the two-dimensional field, this study used a three-hole pressure probe to obtain data traversed over one pitch of cascade. In this work, each pitch was split into 32 equal divisions, i.e., the distance between the measuring points for each traversed pitch was Δy = 2.5 mm thus, 33 points were being measured entirely during the experiment.

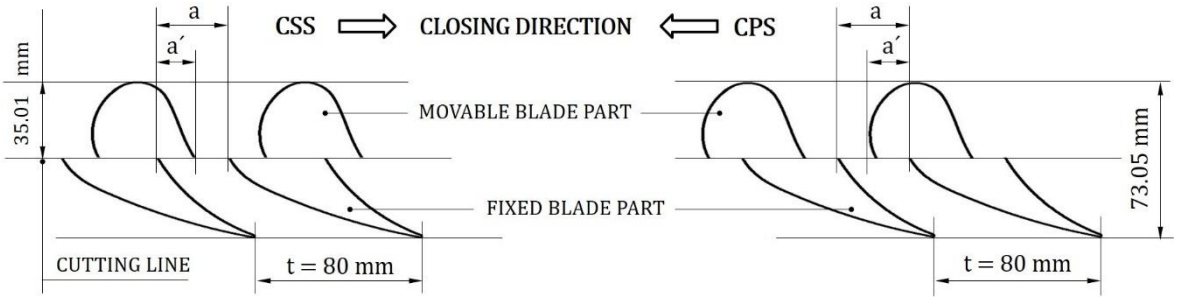

Figure 3.8 Definition of two different closing models of closing to pressure side (CPS) and closing to suction side (CSS)

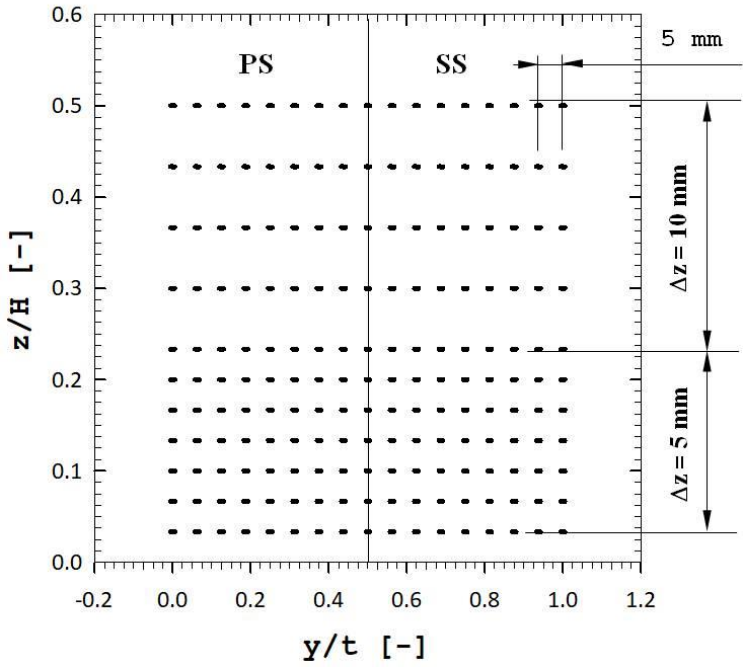

Figure 3.9 Measurement grids and coordinate system downstream of the cascade

To obtain a description of the three-dimensional flow field, the five-hole pressure probe was used. This probe was traversed over one pitch and over half the span to collect data at 11 spanwise locations with step size varies beginning at 50% span and moving towards the endwall, with the end location at approximately 3.3% span. At every spanwise location, 17 evenly spaced pitchwise data points with a constant increamental space of Δy = 5 mm are used to give a considerable measurement grid of around 187 data points, while keeping the

Die approbierte gedruckte Originalversion dieser Dissertation ist an der TU Wien Bibliothek verfügbar.
The approved original version of this doctoral thesis is available in print at TU Wien Bibliothek.
TU Bibliothek Your knowledge hub WIEN

wind tunnel operational duration acceptable. The contoured grids were developed so that the perturbations from the endwall reduce towards midspan. The midspan to endwall distance would be 75 mm meaning that ratio z/H required is 0.5. A contoured measurement grid is shown in Fig. 3.9.

Corresponding data to each measuring point were being automatically recorded for 50 times with a time interval of 0.01 seconds to deduct the random errors of measuring. Also, before starting the measuring in each point, it needed a short delay time to stabilize the new position of the probe. The same delay was occurred after each switching to new measurement line of the probe to calm down the vibration in pneumatic line. After sending data to the personal computer, the mean values of the sensed parameters, such as pressures by each hole of the probe, were analyzed with the aim of LabVIEW 7.1 program.

3.3 Free jet facility

In using pneumatic probes for flow pressure measurement, all probes are aerodynamically calibrated against a known reference. These probes are calibrated against pitch angle, yaw angle, and total and static pressure at a given Reynolds number. During the calibration process, the calibration coefficients are determined. They are required to derive the two or three-dimensional flow properties in the data reduction. The probe calibration was taken in the free jet facility as shown in Fig. 3.10.

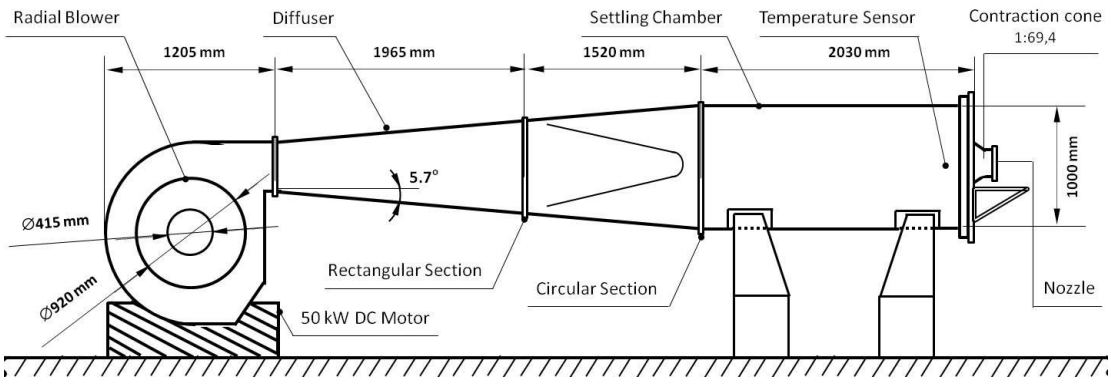

Figure 3.10 Schematic of free jet facility for the pneumatic probe calibration

The free jet facility is made up of the converging nozzle which has a throat diameter of 120 mm with the ratio of convergent of the cone is 1:69.4 and the settling chamber with a diameter of 1000 mm and its length is 2030 mm. The free jet flow is driven by a 50 kW DC motor with the variable speed control transmission. The motor rotates a radial blower with a diameter of 1115 mm and moves air flow into the wind tunnel with a flow rate of 10800 m^3/h. The assembling of motor and blower is installed on a fixed base of concrete material as vibration absorber, and it is separated from diffuser which has a divergence angle of 5.7°. The free jet facility also is equipped with screens of nylon to make for a

Die approbierte gedruckte Originalversion dieser Dissertation ist an der TU Wien Bibliothek verfügbar.
The approved original version of this doctoral thesis is available in print at TU Wien Bibliothek.
TU Bibliothek Your knowledge hub WIEN

uniform and parallel flow with low turbulence intensity about 1% measured by using a single hot-wire probe DANTEC 55P11.

During the calibrations, precautions are taken to ensure that the probes are in the potential core of the jet. The assembly keeps the probe tip at the centerline for all movements. In each case, the probe head blockage ranges between 1.6% and 3% of the nozzle exit area. The total pressure of the calibration region from free jet was measured upstream of the nozzle. The static pressure at the probe head is derived from the atmospheric pressure. The definition of the pressure calibration coefficients is probe specific and can be found in the associated section of the probe in use.

Coulon [10] studied the free jet characteristic downstream of the nozzle exit and proved that there was a homogenous flow field up to $0.6d_n$ and up to a distance of about $2.5d_n$ (d_n = diameter of nozzle exit); outside this core regime the local total pressure rapidly decreases down to 75% of its value in the settling chamber. Hence, when the probe tip position equal to the diameter of nozzle exit, it is accepted that the flow quantities such as speed, turbulence, pressure, etc, are the most convenient to measure the desired values. Therefore, the pneumatic probe was placed at 130 mm downstream of the nozzle exit and it was mounted in a support device as shown in Fig. B.3.

Instrumentation: The measurements were conducted in atmospheric air states of free jet discharging. The probes calibration was done at different Reynolds numbers as well as considering an interval of flow angles. At each calibration point, the pneumatic probes provide pressure measurements. These pressure signals are transformed become electrical signals on the pressure transducer (HONEYWELL). Collecting data was taken by using the HP 3852A data acquisition system which was linked to a PC through GPIB bus and processed using the LabVIEW 7.1 program made by National Instruments as illustrated in a block diagram of Fig. 3.11. The 8V DC power supply was used to drive all piezoresistive pressure transducers. The voltage was measured by a 13-bit-high speed voltmeter HP 44702B. The flow temperature was recorded with resistor thermometer Pt-100. The other equipment of data transmission components comprises a 16-channel HP 44724A digital output device and 24-channel HP 44711A multiplexer.

It is commonly used to simplify the measurement of pressure from a multi-tube probe. The total pressure of free stream p_t and the stagnation pressure p_1 both are measured using two identical piezoresistive transducers. In this case, the pressure range of the measuring work for the instrument is from 0 up to +138 mbar. The outer hole of pressures p_2 and p_3 for the three-hole probe and p_2, p_3, p_4, and p_5 for the five-hole probe are all measured using a single transducer with a scanning box (FURNESS CONTROLS). Since these pressures are relative to the atmospheric one, in which they can be a positive, and negative value. Thus, a differential piezoresistive transducer is needed. This piezoresistive transducer has a range of working pressure from -69 mbar up to +69 mbar. For this measurement, the reference

Die approbierte gedruckte Originalversion dieser Dissertation ist an der TU Wien Bibliothek verfügbar.
The approved original version of this doctoral thesis is available in print at TU Wien Bibliothek.
TU Bibliothek Your knowledge hub WIEN

total pressure was measured in the upstream settling section, and atmospheric pressure was used as a reference static pressure.

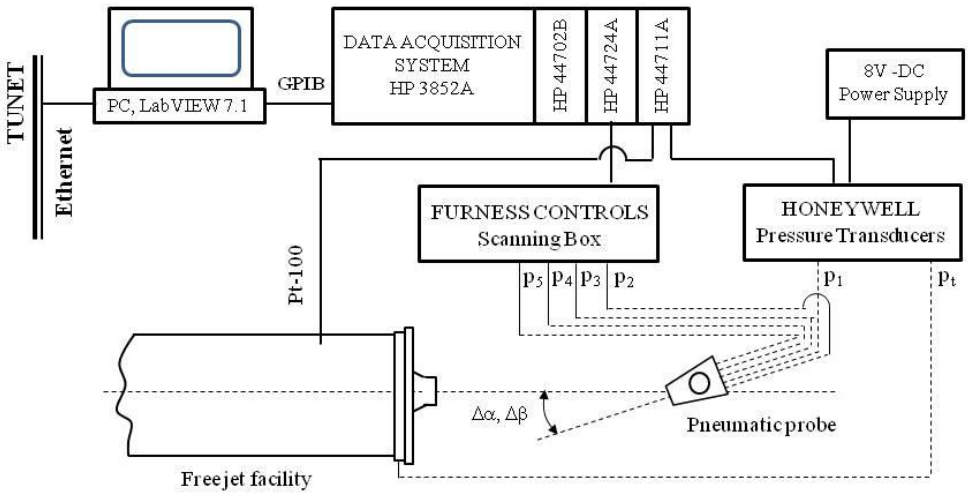

Figure 3.11 Block diagram of instrumentation for the calibration process

3.4 Pneumatic measurement system

3.4.1 Total and static pressure probe

The approach freestream velocity was measured using a total pressure probe with its tip 240 mm above the bottom wall, and 75 mm from the sidewall, at 225 mm upstream of the leading edge of the blade #4. The inlet total pressure was measured with a total pressure probe as in Fig. 3.12 with the dimension of 3 mm outer and 1 mm inner diameter.

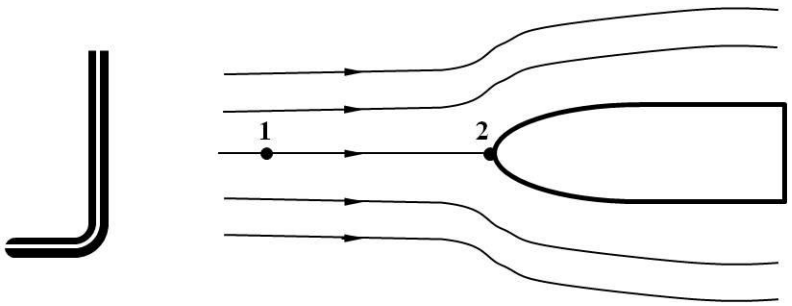

Figure 3.12 Total pressure probe and its streamline

A separate reference wall static pressure tap was used to measure the static pressure of the upstream test section. To measure the static pressure, a hole of 2 mm diameter in the sidewall of the wind tunnel was used to connect a tube which was further connected to a piezoresistive differential pressure sensor.

Die approbierte gedruckte Originalversion dieser Dissertation ist an der TU Wien Bibliothek verfügbar.
The approved original version of this doctoral thesis is available in print at TU Wien Bibliothek.
TU Bibliothek Your knowledge hub WIEN

At two different points along the same streamline as shown in Fig. 3.12, Bernoulli's equation is expressed as

$$\frac{p_1}{\rho g} + \frac{C_1^2}{2g} + z_1 = \frac{p_2}{\rho g} + \frac{C_2^2}{2g} + z_2. \tag{3.2}$$

This equation gives the correlation between dynamic pressure and flow velocity along a streamline given that the value of the density of the medium is known.

Given that $z_1 = z_2$, therefore the difference between total and static pressure is the dynamic pressure, considering the assumption of incompressible flow, the inlet flow velocity (C_0) could be calculated as

$$C_0 = \sqrt{\frac{2(p_{0t} - p_{0s})}{\rho}} \tag{3.3}$$

with ρ is the density. From measurement data, the inlet mean velocity for this study was about 23 m/s which corresponds to Mach numbers around 0.073. In the inlet test section, this condition is substantially incompressible.

The air density used for recent experiment is developed from the isentropic condition and determined by using the equation as

$$\rho = \frac{p_t}{RT_t}\left(\frac{p}{p_t}\right)^{1/k} \tag{3.4}$$

with k is specific heat ratio. From the experimental measurement data, the average air density for this study is 1.23 kg/m^3.

The operating condition of linear cascade wind tunnel is set to fulfill a certain Reynolds number (Re) based on the inlet flow velocity (C_0), and axial chord of the blade (b). Then, the Reynolds number is calculated as

$$Re = \rho \frac{C_0\, b}{\mu} \tag{3.5}$$

where ρ is the air flow density and μ is the air dynamic viscosity. From equation (3.5), the Reynolds number used for current investigation is about 1.14 x 10^5.

The dynamic viscosity for this investigation was calculated by using an equation that was found by Sutherland [44]. This equation is an empirical correlation and expressed as

$$\mu = \mu_o \left(\frac{T}{T_o}\right)^{3/2} \frac{T_o + S}{T + S} \tag{3.6}$$

Die approbierte gedruckte Originalversion dieser Dissertation ist an der TU Wien Bibliothek verfügbar.
The approved original version of this doctoral thesis is available in print at TU Wien Bibliothek.
TU Bibliothek Your knowledge hub WIEN

where $\mu_o = 1.716.10^{-5}$ kg/m.s is reference viscosity, $T_o = 273.15$ K is reference temperature and S = 110.4 K is Sutherland temperature constant. Based on the equation (3.6) the dynamic viscosity of working fluid for current investigation is about 1.814×10^{-5} kg/m.s.

3.4.2 Static pressure taps

Static pressure taps were drilled into the blade along pressure and suction surface, which were used to measure surface static pressure. These pressure taps were screwed into the blade surfaces such that ensure smooth flow over the pressure port. The ports were then connected to pressure transducers using plastic tubing. Due to the limited numbers of available surface pressure taps in the measurements, thus there was just a total of 29 static pressure taps used to measure this pressure distribution, 15 of which were located along the suction surface, 13 of which were positioned along the pressure surface and one of which was at the leading edge. The locations of these pressure taps are shown in Fig. 3.13.

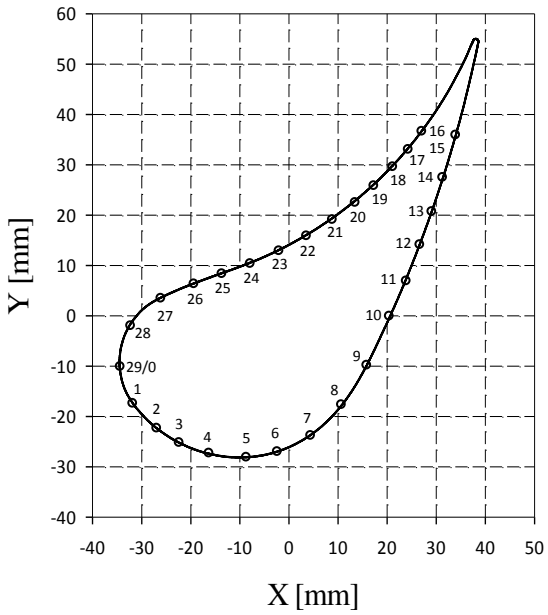

Figure 3.13 Coordinates of pressure taps in midspan of the blade cascade

3.4.3 Three-hole pneumatic probe

Measurements of the two-dimensional flow field were mainly obtained by a three-hole pneumatic probe which is schematically shown in Fig. 3.14. The probe has a head with a cross-sectional area of 0.8 mm x 2.4 mm and the front fences of holes 2 and 3 having a wedge angle of 30°. The shaft of the probe has a diameter of 6 mm with the inner diameter of each hole is 0.5 mm. The probe was placed downstream of the center test blade and oriented in the primary flow direction, in a non-nulling mode. The non-nulling technique

Die approbierte gedruckte Originalversion dieser Dissertation ist an der TU Wien Bibliothek verfügbar.
The approved original version of this doctoral thesis is available in print at TU Wien Bibliothek.
TU Bibliothek Your knowledge hub WIEN

allows the determination of direction and velocity magnitude of the flow with respect to the probe's axis coordinates. This means that the axis of the hole 1 is not aligned in stream direction at every measuring point. The probe head is inclined as a well-defined difference expected to occur at holes 2 and 3. This setup angle Δβ has to be observed when evaluating the results of experiment by either adding or subtracting the setup angle to the yaw angle, solely depending on the coordinate system used for the examination.

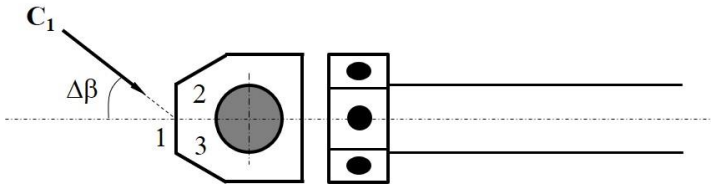

Figure 3.14 Schematic of three-hole probe and diagram of the port position

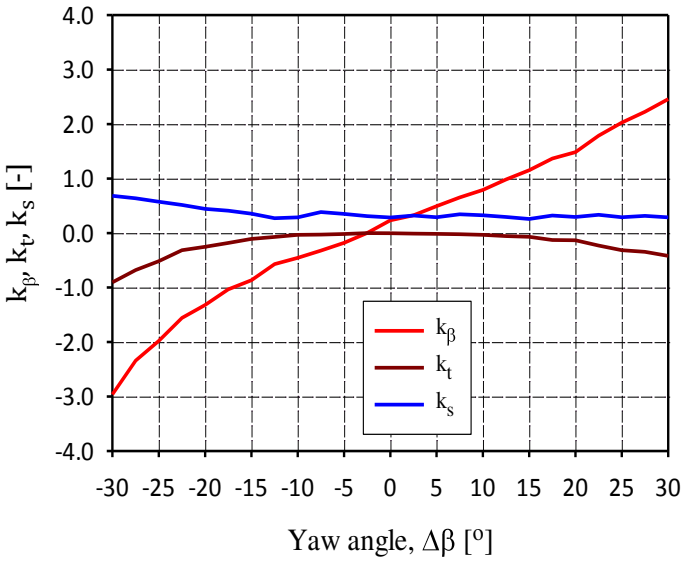

Figure 3.15 Calibration curves of the pneumatic three-hole probe

Calibration procedures: The calibration results applied here aimed to describe calibration coefficient curves for direction (k_β), total (k_t) and static pressure (k_s). These calibration coefficients were plotted against yaw angle ($\Delta\beta$) as shown in Fig. 3.15. The probe was calibrated in the free jet tunnel at Re = 1.3 $\times 10^4$ based on the probe head. Using a method of Treaster and Yocum [45], the coefficient of direction is expressed as

$$k_\beta = \frac{p_2 - p_3}{p_1 - \bar{p}} \tag{3.7}$$

with k_β is direction coefficient. Then k_β gives a relation between the yaw angle and the pressure difference at holes 2 and 3. Location of intersection points for each line on this line related to one calibration point.

Die approbierte gedruckte Originalversion dieser Dissertation ist an der TU Wien Bibliothek verfügbar.
The approved original version of this doctoral thesis is available in print at TU Wien Bibliothek.
TU Bibliothek Your knowledge hub WIEN

Total and static coefficients over the range of interpolated angles and pressures are calculated by

$$k_t = \frac{p_1 - p_t}{p_1 - \bar{p}} \quad \text{and} \quad k_s = \frac{\bar{p} - p_s}{p_1 - \bar{p}} \tag{3.8}$$

where p_t is total pressure, p_s is static pressure, k_t and k_s represent total and static pressure coefficient. While average pressure is calculated as follows

$$\bar{p} = \frac{1}{2}(p_2 + p_3) \tag{3.9}$$

where $\bar{p}$ stands for average-hole pressure reading between the pressure in the port 2 and port 3 position as shown in Fig. 3.14.

The probe was rotated through an incremental angle of 2.5° with the measurement range of yaw angle $\Delta\beta = \pm 30°$. At the central probe hole, pressure p_1 is measured, while p_2 and p_3 were measured in the yaw plane. Yawing of pressure probe caused the changes of pressure for holes 2 and 3 in the yaw direction. For the calibration, measurements of total pressure p_t and static pressure p_s along with the probe pressures p_1 through p_3 were conducted. Using linear interpolation, the total and static pressure coefficient are calculated by using the coefficient of direction from Fig. 3.15. Further from the calibration coefficient equations (3.8) were substituted to get the calibration-corrected total and static pressure at the interest point. Then, the local velocity was calculated from total and static pressure using Bernoulli´s equation.

3.4.4 Five-hole pneumatic probe

Three-dimensional flow fields were documented using a five-hole pneumatic probe. This probe consists of four tubes arranged around a center tube with the port numbering definition follows the method introduced by Treaster and Yocum [45]. Subscripts ‘2’ and ‘3’ denote the two-side static ports on the probe, while ‘4’ and ‘5’ represent the upper and lower static ports on the probe. Subscript ‘1’ is the total pressure port on the probe. The presence of five holes makes it possible to measure the yaw angle in the yaw plane as well as pitch angle in the pitch plane of the flow, along with the total and static pressures. In this way, the five-hole probe can capture the entire three-dimensional flow.

The probe used for this measurement as illustrated in Fig. 3.16 has a tip diameter of 3 mm is shaped as a conical shape with a wedge angle of 30° (between the probe axis and the direction parallel to the probe head sides). Additionally, the diameter of each hole is 0.5 mm, and the distance between the center of the side holes on each axis is 1.85 mm. The center hole is placed in a surface which is orthogonal to the probe tip axis. The advantage

Die approbierte gedruckte Originalversion dieser Dissertation ist an der TU Wien Bibliothek verfügbar.
The approved original version of this doctoral thesis is available in print at TU Wien Bibliothek.
TU Bibliothek Your knowledge hub WIEN

of the cone-head shape is that all holes on the circumference of the probe head show a similar pressure sensitivity to angle variations.

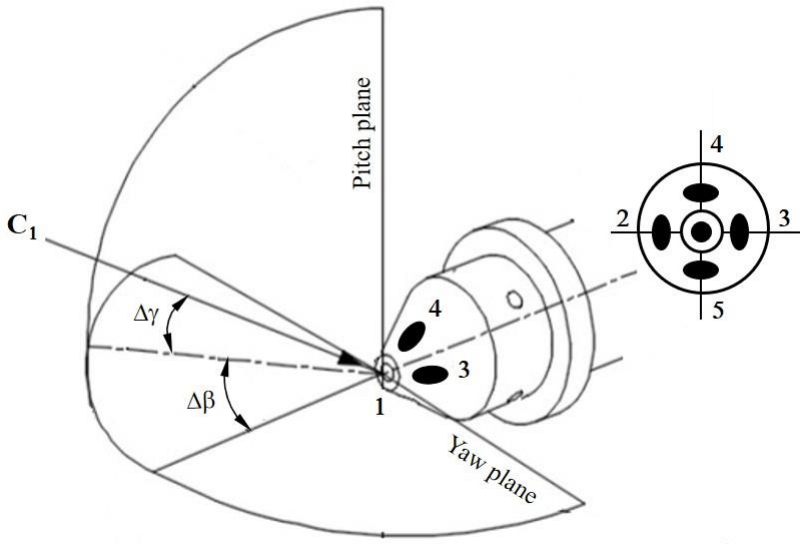

Figure 3.16 Schematic of five-hole pneumatic probe and hole definition

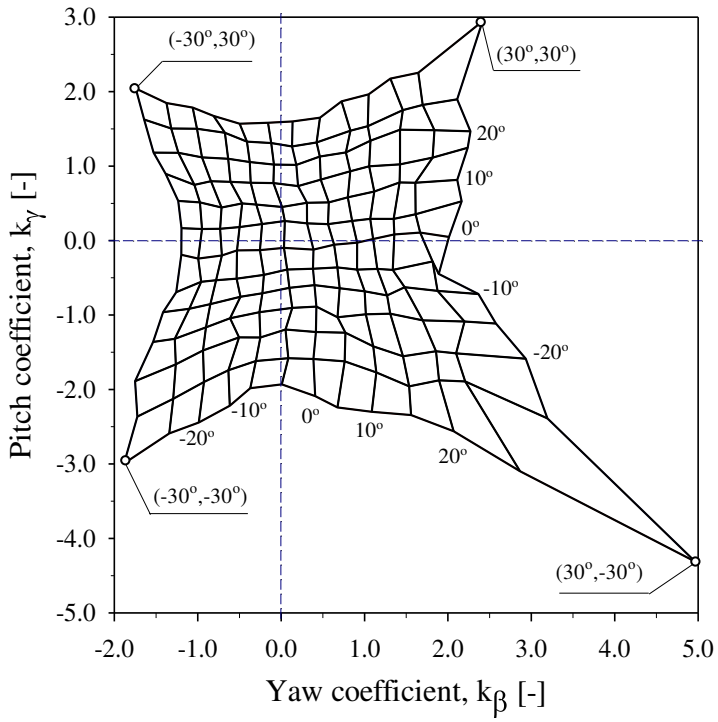

Figure 3.17 Calibration map of k_β versus k_γ for the five-hole pneumatic probe

Calibration procedures: The purpose of this calibration is to develop a correlation between the five measured pressures, and the directional coefficients obtained from them, and the flow angles and total pressure and static pressure coefficients. The pneumatic

Die approbierte gedruckte Originalversion dieser Dissertation ist an der TU Wien Bibliothek verfügbar.
The approved original version of this doctoral thesis is available in print at TU Wien Bibliothek.
TU Bibliothek Your knowledge hub WIEN

probes are used to measure these quantities. The relationship between them and each the yaw angle ($\Delta\beta$) and pitch angle ($\Delta\gamma$) is described by the calibration coefficients. The calibration consists of rotating the probe over a range of yaw angle from $\Delta\beta$ = -30° up to $\Delta\beta$ = +30° and range of pitch angle from $\Delta\gamma$ = -30° up to $\Delta\gamma$ = +30° with respect to a known one-dimensional flow field and recording all five port pressures, namely p_1, p_2, p_3, p_4 and p_5 for each combination of yaw angle and pitch angle.

The pressure coefficients must be defined so that they are independent of velocity and are a function only of the flow angularity. For this case, they showed that an indicated dynamic pressure formed by the difference between the indicated total pressure p_1, and the mean value of the four indicated static pressures p_2, p_3, p_4, and p_5, is a satisfactory normalizing parameter. The difference between the two pressures is consequently taken to represent the dynamic pressure, which is used to make the calibration coefficients.

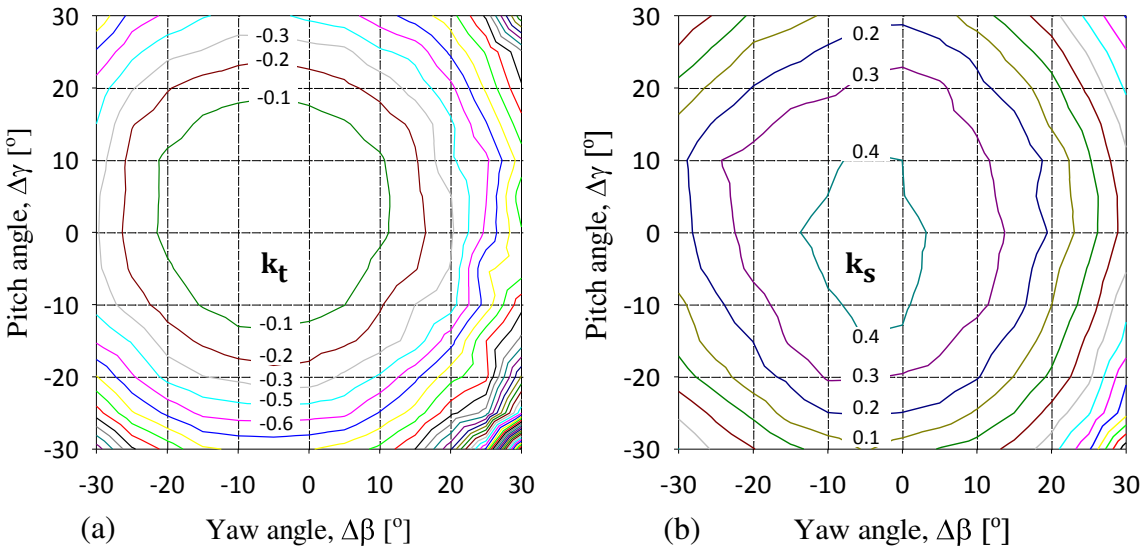

Figure 3.18 Calibration graphs of five-hole pneumatic probe: (a) total pressure coefficient (k_t); (b) static pressure coefficient (k_s)

In the calibration process of the five-hole probe, yawing of the probe caused changes in the side port pressures 2 and 3 while pitching of the probe caused changes in the upper and lower port pressures 4 and 5. A calibration map which correlated the pitch and yaw angles to the change in port pressures was then created and is depicted in Fig. 3.17. Each dot on this map corresponded to one calibration point, and the lines connecting each dot are lines of constant $\Delta\beta$ or constant $\Delta\gamma$. Yaw and pitch angle then were interpolated by using functions that relate the angles to the port pressures, given by equations as follows

$$k_\beta = \frac{p_2 - p_3}{p_1 - \bar{p}} \quad \text{and} \quad k_\gamma = \frac{p_4 - p_5}{p_1 - \bar{p}}. \tag{3.10}$$

Total and static pressure coefficients over the range of interpolated flow angles and pressures are calculated by

Die approbierte gedruckte Originalversion dieser Dissertation ist an der TU Wien Bibliothek verfügbar.
The approved original version of this doctoral thesis is available in print at TU Wien Bibliothek.
TU Bibliothek Your knowledge hub WIEN

$$k_t = \frac{p_1 - p_t}{p_1 - \bar{p}} \quad \text{and} \quad k_s = \frac{\bar{p} - p_s}{p_1 - \bar{p}} \tag{3.11}$$

here, $\bar{p}$ is mean pressure and calculated as

$$\bar{p} = \frac{1}{4}(p_2 + p_3 + p_4 + p_5). \tag{3.12}$$

When the probe is subjected to unknown flow velocity at a point in the flow, the five-hole probe port pressures are sequentially recorded using the pressure transducer, as described previously. With the five determined pressures for each measuring point, k_β and k_γ are determined by using equation (3.10). From these five pressure values, the flow angles $\Delta\beta$ and $\Delta\gamma$ are interpolated from Fig. 3.17 by using the bilinear interpolation. This method is explained in the following section.

Bilinear interpolation method: To conduct the interpolation on an arbitrary quad as shown in Fig. 3.19, it needs to obtain a mapping function. It is purposed to come up with a function such that (x, y) = f (r, s) with r = [0, 1] and s = [0, 1] describes the entire point space enclosed by the quadrilateral. Hence, the corresponding function in each point is f (0, 0) = (x_1, y_1), f (1, 0) = (x_2, y_2), f (1, 1) = (x_3, y_3) and f (0, 1) = (x_4, y_4). This function forms a map that allows the transformation from the natural coordinate as illustrated in Fig. 3.19a set to a transformed coordinate space as shown in Fig. 3.19b.

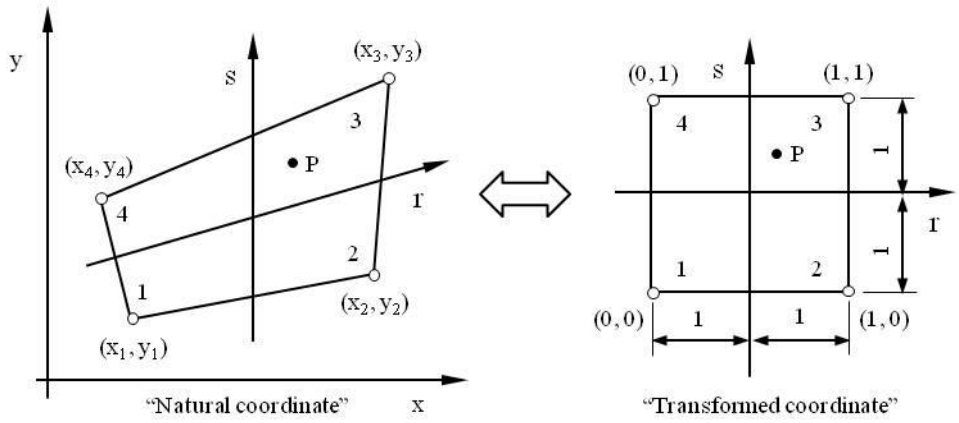

(a) (b)

Figure 3.19 Element with 4 nodes: (a) natural coordinate; (b) transformed coordinate for bilinear interpolation

Based on the mentioned method above, the trapezoid where the arbitrary point P was situated in the intersection of $\Delta\beta$ and $\Delta\gamma$ values (Fig. 3.19a) was transformed into a quadrilateral shape with a side length of 2 (Fig. 3.19b). In this transformed coordinate therefore the exact position of P in the relevant quadrilateral was determined by using the

Die approbierte gedruckte Originalversion dieser Dissertation ist an der TU Wien Bibliothek verfügbar.
The approved original version of this doctoral thesis is available in print at TU Wien Bibliothek.
TU Bibliothek Your knowledge hub WIEN

method of bilinear interpolation for a four-node element with the equations that can be expressed as

$$\bar{\varphi} = \begin{pmatrix} \varphi_1(r,s) \\ \varphi_2(r,s) \\ \varphi_3(r,s) \\ \varphi_4(r,s) \end{pmatrix} = \begin{pmatrix} \frac{1}{4}(1-r)(1-s) \\ \frac{1}{4}(1+r)(1-s) \\ \frac{1}{4}(1+r)(1+s) \\ \frac{1}{4}(1-r)(1+s) \end{pmatrix} \tag{3.13}$$

where φ_1, φ_2, φ_3, φ_4 represent functions for the four corner nodes of the quadrilateral in the transformed space. This equation (3.13) can be solved for r and s with any suitable equation solving method. The coordinates of any arbitrary point P then was determined by equations as

$$x_p = \sum_{i=1}^{4} \varphi_i(r,s) x_i \tag{3.14}$$

and

$$y_p = \sum_{i=1}^{4} \varphi_i(r,s) y_i \,. \tag{3.15}$$

After getting the determined values of r and s, the relevant quadrilateral in the calibration grid of k_β versus k_γ, and therefore $\Delta\beta$ and $\Delta\gamma$ at the edges of the quadrilateral, thus the angles $\Delta\beta$ and $\Delta\gamma$ for point P can be found. Knowing the flow angles $\Delta\beta$ and $\Delta\gamma$, the total and static pressure coefficients were determined using Fig. 3.18a and 3.18b, respectively. From these two coefficients, equations (3.11) were inverted to get the calibration-corrected total pressure and static pressure at the point of interest. Later, the velocity was computed from these two pressures using Bernoulli's equation.

3.5 Hot-wire anemometry

Hot-wire anemometry is one of the techniques that can be applied to measure local mean velocity and condition on turbulence level. This probe has extremely high frequency-response and fine spatial resolution, provides a continuous signal. In addition, it can give reliable information on the fluctuating flow component in both the space and time domains. In this research, single hot-wire probe as shown in Fig. 3.20 was used to measure the turbulence intensity of the exit flow. This probe is a constant temperature anemometer (CTA) DANTEC 55P11 with a diameter of 5 μm and a length of 1.25 mm. Moreover, this probe measured the time varying velocity downstream of the cascade trailing edge at the

Die approbierte gedruckte Originalversion dieser Dissertation ist an der TU Wien Bibliothek verfügbar.
The approved original version of this doctoral thesis is available in print at TU Wien Bibliothek.
TU Bibliothek Your knowledge hub WIEN

location of 0.3 axial blade chord. As measurements were conducted, hot-wire was traversed across the downstream measurement plane using a DANTEC traversing mechanism. Instructions for the operation systems of the controller were provided by StreamWare3 software from the PC (personal computer).

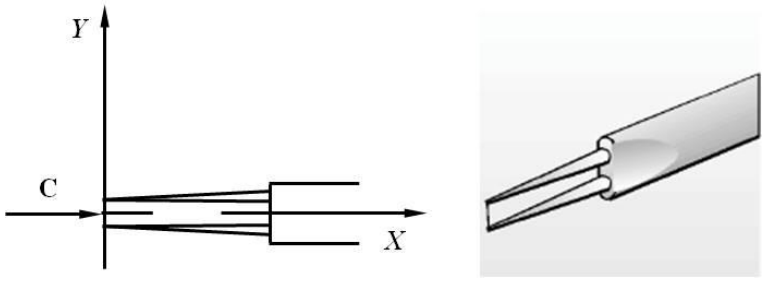

Figure 3.20 CTA single probe and coordinate system

The hot wire is heated by an electric current and convectively cooled by the heat transfer generated by the low temperature of the incident flow. The electrical resistance of the hot wire is affected by its temperature. King [25] gave a relation among these parameters for subsonic incompressible flows as

$$\frac{RI^2}{R - R_{ref}} = A + BC^{0.5} \tag{3.16}$$

where R is the sensor resistance at the operating temperature T during the calibration, R_{ref} is the resistance at the ambient temperature T_{ref} during the calibration and I is the electrical current passing through the hot wire.

The calibration is needed in the measuring that uses heat transfer to deduce local instantaneous velocity components. It is usually conducted under flow conditions and for fluid properties different from those in the experiments where the calibrated hot-wire is used. The traditional calibration equation of single normal probe based on the King's law as shown by Bruun [7] is expressed as

$$E^2 = A + BC^n \tag{3.17}$$

with King's evaluation predicting n as 0.5. The constant-exponent power law in this equation has three variable parameters A, B and n.

The constant temperature anemometer is designed with the purpose of eliminating the effect of the thermal inertia of the wire in fluctuating flows. As the constant temperature anemometry signal from a turbulent flow will be of random nature, a statistical description of the signal is necessary. A single velocity time series gives mean, mean square and higher

Die approbierte gedruckte Originalversion dieser Dissertation ist an der TU Wien Bibliothek verfügbar.
The approved original version of this doctoral thesis is available in print at TU Wien Bibliothek.
TU Bibliothek Your knowledge hub WIEN

order moments. To determine the turbulence intensity in the flow velocity measurements by 1D hot-wire, the method used in this research refers to Jorgensen [22].

From the hot-wire measurement data, mean velocity of the outlet flows downstream of the cascade is calculated as

$$\bar{C} = \frac{1}{N}\sum_{1}^{N} C_i \tag{3.18}$$

where N is the number of C values. The standard deviation of the set of random velocity fluctuation is formulated by

$$C_{rms} = \sqrt{\frac{1}{N-1}\sum_{1}^{N}(C_i - \bar{C})^2}. \tag{3.19}$$

Turbulence intensity is given as the standard deviation and determined as

$$Tu = \frac{C_{rms}}{\bar{C}} x\ 100\% \tag{3.20}$$

with the subscript rms stands for root-mean-square. A larger C_{rms} indicates a higher level of the turbulence.

3.6 Uncertainty analysis

3.6.1 Statistical uncertainty

In the experimental research, it is important to analyse the measurement uncertainties to obtain correct information, to validate the numerical tools, to perform an evaluation of the components, and to interpret the reported results correctly. The measurement accuracy of a probe is determined by several sources of uncertainty, which must be quantified to get the individual uncertainty of the probe. Most of these uncertainties occur during measurement and calibration process including the uncertainties in probe position, data acquisition, and calibration data.

The uncertainty of probe position covers the difference of the actual probe position from the reference position, because of positioning uncertainty during probe installation. The uncertainty in pressure data acquisition is resulted by the probe pressure data acquisition system. It is related to an uncertainty depending on factors for instance accuracy, stability, the sensitivity of pressure sensor and resolution scanning boards, etc. The uncertainty of calibrated data is produced during the calibration process.

Die approbierte gedruckte Originalversion dieser Dissertation ist an der TU Wien Bibliothek verfügbar.
The approved original version of this doctoral thesis is available in print at TU Wien Bibliothek.
TU Bibliothek Your knowledge hub WIEN

Standard deviation: In general, uncertainty is determined as a measurement range of possible true values. This parameter is very important information in the describing an experimental accuracy for measurement data. Some interesting parameters are commonly expressed on two parts, i.e., estimated true value as mean value and its uncertainty. The statement about the value of x based on measurements is that with 95% confident that the true value of x lies within the interval

$$\bar{x} \pm \sigma_x \tag{3. 21}$$

with $\bar{x}$ is usually assumed to be the mean value of N repeated measurement and defined as

$$\bar{x} = \frac{1}{N}\sum_{i=1}^{N} x_i \tag{3. 22}$$

and $\sigma_x$is the uncertainty in x with 95% confidence. Then, the uncertainty represented by the standard deviation of repeated N values in a measurement can be expressed

$$\sigma_X = \sqrt{\frac{1}{N-1}\sum_{i=1}^{N}(x_i - \bar{x})^2}\,. \tag{3.23}$$

The uncertainty has given here is an absolute uncertainty. Another way to express uncertainty is relative uncertainty (ε), defined as the absolute uncertainty divided by the estimated true value.

$$\varepsilon = \frac{\sigma_x}{\bar{x}} x\ 100\%. \tag{3.24}$$

Propagation of uncertainty: The uncertainty calculation is estimated on the method of Coleman and Steele [9] and Kline and McClintock [26]. A quantity, P is a function of individual error sources as independent variables $q_1, q_2, q_3, \ldots, q_n$ such that

$$P = f(q_1, q_2, q_3, \ldots, q_n). \tag{3.25}$$

If each error source on P has uncertainty σq_1, σq_2, $\sigma q_3, \ldots$, σq_n, therefore uncertainty propagation of P can be calculated as

$$\sigma(P) = \sqrt{\left(\frac{\partial P}{\partial q_1}\sigma q_1\right)^2 + \left(\frac{\partial P}{\partial q_2}\sigma q_2\right)^2 + \left(\frac{\partial P}{\partial q_3}\sigma q_3\right)^2 + \cdots + \left(\frac{\partial P}{\partial q_n}\sigma q_n\right)^2}\,. \tag{3.26}$$

The uncertainty for each kind of experiment in this investigation will be quoted in relation to the description of the equipment employed to measure it below.

Die approbierte gedruckte Originalversion dieser Dissertation ist an der TU Wien Bibliothek verfügbar.
The approved original version of this doctoral thesis is available in print at TU Wien Bibliothek.
TU Bibliothek Your knowledge hub WIEN

3.6.2 Uncertainties of operating condition

This section presents a calculation of uncertainties related to several operating parameters measured during the experiment such as the total and static pressures, density and inlet velocity. The raw data values used in this evaluation include the pressure values collected by the total pressure probe and wall pressure tap. For the data collection, the pressure scanner functions such that, at each measurement point, 50 different values were measured, and the averages of these values were taken as the data value for that location.

Uncertainty in total and static pressure: The statistical or random uncertainty for each of the pressure values was calculated by using equation (3.23) taking the standard deviation at each measurement point. Based on this calculation, the uncertainty in measuring the total pressure was calculated as ±7.4 Pa (±0.007%) and the uncertainty in the static pressure was calculated as ±9.6 Pa (±0.01%).

Uncertainty in air density: The density of working fluid for each measurement in the upstream section of the linear cascade for the current study is determined from the relation

$$\rho = \frac{p_t}{RT_t}\left(\frac{p}{p_t}\right)^{1/k}. \tag{3.27}$$

The propagation of uncertainty in density value $\sigma(\rho)$ can be expressed as

$$\sigma(\rho) = \sqrt{\left(\frac{\partial\rho}{\partial p_t}\sigma p_t\right)^2 + \left(\frac{\partial\rho}{\partial p}\sigma p\right)^2 + \left(\frac{\partial\rho}{\partial R}\sigma R\right)^2 + \left(\frac{\partial\rho}{\partial T_t}\sigma T_t\right)^2} \tag{3.28}$$

where

$$\frac{\partial\rho}{\partial p_t} = \frac{k-1}{kRT_t}\left(\frac{p}{p_t}\right)^{\frac{1}{k}},$$

$$\frac{\partial\rho}{\partial p} = \frac{1}{kRT_t}\left(\frac{p}{p_t}\right)^{\frac{(1-k)}{k}},$$

$$\frac{\partial\rho}{\partial R} = -\frac{p_t}{R^2T_t}\left(\frac{p}{p_t}\right)^{\frac{1}{k}},$$

and

$$\frac{\partial\rho}{\partial T} = -\frac{p_t}{RT_t{}^2}\left(\frac{p}{p_t}\right)^{\frac{1}{k}}.$$

The uncertainties in R and T_t are considered zero and are neglected in this case, therefore after replacing the partial derivatives, equation (3.28) is given as

Die approbierte gedruckte Originalversion dieser Dissertation ist an der TU Wien Bibliothek verfügbar.
The approved original version of this doctoral thesis is available in print at TU Wien Bibliothek.
TU Bibliothek Your knowledge hub WIEN

$$\sigma(\rho) = \sqrt{\left[\left(\frac{k-1}{kRT_t}\sqrt[k]{\left(\frac{p}{p_t}\right)}\right)\sigma p_t\right]^2 + \left[\left(\frac{1}{kRT_t}\sqrt[k]{\left(\frac{p}{p_t}\right)^{1-k}}\right)\sigma p\right]^2}. \quad (3.29)$$

According to the propagation of uncertainty rules as expressed in equation (3.29) above, the uncertainty in measuring the flow density through the upstream test section of linear cascade was calculated as $\pm 8.5 \times 10^{-5}$ kg/m^3 ($\pm 0.007\%$).

Uncertainty in inlet velocity: The fluid flow at the upstream passes through a strong inlet contraction fitted with flow straighteners and is uniform. The axial freestream velocity of the flow inlet to the linear cascade can then be calculated from the relation as

$$C_0 = \sqrt{\frac{2(p_{0t} - p_{0s})}{\rho}} \quad (3.30)$$

with C_0 is inlet flow velocity upstream of the linear cascade. The absolute uncertainty in inlet velocity $\sigma(C_0)$ can then be expressed as

$$\sigma(C_0) = \sqrt{\left(\frac{\partial C_0}{\partial p_{0t}}\sigma p_{0t}\right)^2 + \left(\frac{\partial C_0}{\partial p_{0s}}\sigma p_{0s}\right)^2 + \left(\frac{\partial C_0}{\partial \rho}\sigma\rho\right)^2} \quad (3.31)$$

where

$$\frac{\partial C_0}{\partial p_{0t}} = \sqrt{\frac{1}{2\rho(p_{0t} - p_{0s})}},$$

$$\frac{\partial C_0}{\partial p_{0s}} = -\sqrt{\frac{1}{2\rho(p_{0t} - p_{0s})}},$$

and

$$\frac{\partial C_0}{\partial \rho} = -\frac{1}{2}\sqrt{\frac{2(p_{0t} - p_{0s})}{\rho^3}}.$$

by replacing the partial derivatives, the equation (3.31) can be expressed as

$$\sigma(C_0) = \sqrt{\left[\sqrt{\frac{\sigma p_{0t}}{2\rho(\Delta p)}}\right]^2 + \left[-\sqrt{\frac{\sigma p_{0s}}{2\rho(\Delta p)}}\right]^2 + \left[-\frac{1}{2}\sqrt{\frac{2(\Delta p)}{\rho^3}}\sigma\rho\right]^2} \quad (3.32)$$

Die approbierte gedruckte Originalversion dieser Dissertation ist an der TU Wien Bibliothek verfügbar.
The approved original version of this doctoral thesis is available in print at TU Wien Bibliothek.
TU Bibliothek Your knowledge hub WIEN

with $\Delta p = (p_{0t} - p_{0s})$ is the difference in total and static pressure in the inlet test section of the wind tunnel

Substituting typical values met in the experiment for the uncertainty in measuring these flow parameters with pressure probe device, one can calculate the uncertainty in measuring the inlet flow velocity. Based on the equation (3.32), the uncertainty value in measuring the velocity was calculated as ±2.4%.

Limitations of uncertainty: Because the systematic uncertainties present in measurements are unknown, therefore, these uncertainties have been ignored in current calculation. These unknown values have the systematic uncertainties in the relative humidity factor, total temperature, and total pressure measured at the inlet test section. Involving the systematic uncertainties of these quantities would serve to increase the uncertainty in the density, as these values are used for calculating the gas constant, which is in turn used to calculate the flow density. Combining the systematic uncertainty in the density would increase the entire uncertainty in inlet velocity.

3.6.3 Uncertainty of outlet flow parameter

In this study, the uncertainty of total pressure coefficient is evaluated. The total pressure coefficient is among the most important parameters to quantify the losses in the turbine cascade. This coefficient contains several parameters made up of fluid flow density, inlet velocity, static pressure, inlet and outlet total pressure. This coefficient of total pressure is calculated as

$$C_{pt} = \frac{(p_{1t} - p_{0t})}{\frac{1}{2}\rho C_0^2}. \tag{3.33}$$

From equation (3.33), it is seen clearly that the uncertainty of the total pressure coefficient is affected by uncertainties of density, inlet velocity and the total pressures in the inlet and the outlet. The uncertainties of the inlet condition such as density, inlet velocity, and total pressure have been calculated in the earlier section hence this step is specifically devoted for calculating the uncertainty of total pressure in the outlet through relationships between measured pressures in the holes of pressure probes.

Uncertainties from the linear cascade: The definition of the pressure coefficients k_t and k_s is probe specific and can be found through a relation in equations (3.8) for three-hole probe (3H-P) and (3.11) for five-hole probe (5H-P). Therefore, the total pressure at the exit downstream of the cascade is calculated as

$$p_t = p_1 - k_t(p_1 - \bar{p}) \tag{3.34}$$

Die approbierte gedruckte Originalversion dieser Dissertation ist an der TU Wien Bibliothek verfügbar.
The approved original version of this doctoral thesis is available in print at TU Wien Bibliothek.
TU Bibliothek Your knowledge hub WIEN

In this formula, p_1 is the pressure measured by the central of the probe, while $\bar{p}$ is the average of the pressure measured by two holes at 3H-P or four holes at 5H-P. The constant k_t is calculated based on the probe calibration. Then, the uncertainty in total pressure $\sigma(p_t)$ value can be calculated as

$$\sigma(p_t) = \sqrt{\left(\frac{\partial p_t}{\partial p_1}\sigma p_1\right)^2 + \left(\frac{\partial p_t}{\partial \bar{p}}\sigma \bar{p}\right)^2} \tag{3.35}$$

with

$$\frac{\partial p_t}{\partial p_1} = 1 - k_t,$$

and

$$\frac{\partial p_t}{\partial \bar{p}} = k_t.$$

after substituting the partial derivatives, the equation (3.35) can be written as

$$\sigma(p_t) = \sqrt{[(1 - k_t)\sigma p_1]^2 + [(k_t)\sigma \bar{p}]^2}. \tag{3.36}$$

The static pressure at the exit flow downstream of the cascade is expressed as

$$p_s = \bar{p} - k_s(p_1 - \bar{p}) \tag{3.37}$$

where constant k_s is static pressure coefficient based on the probe calibration. Thus, the uncertainty in static pressure (σ_{ps}) can be expressed as

$$\sigma(p_s) = \sqrt{\left(\frac{\partial p_s}{\partial p_1}\sigma p_1\right)^2 + \left(\frac{\partial p_s}{\partial \bar{p}}\sigma \bar{p}\right)^2} \tag{3.38}$$

with

$$\frac{\partial p_s}{\partial p_1} = -k_s,$$

and

$$\frac{\partial p_s}{\partial \bar{p}} = 1 + k_s.$$

Substituting the partial derivatives, the equation (3.38) is expressed as

$$\sigma(p_s) = \sqrt{[(-k_s)\sigma p_1]^2 + [(1 + k_s)\sigma \bar{p}]^2}. \tag{3.39}$$

Here, constant k_t and k_s are considered not change in all calculations from linear cascade data because not include the uncertainty in the calibration process.

Die approbierte gedruckte Originalversion dieser Dissertation ist an der TU Wien Bibliothek verfügbar.
The approved original version of this doctoral thesis is available in print at TU Wien Bibliothek.
TU Bibliothek Your knowledge hub WIEN

where the uncertainty in the average pressure ($\bar{p}$) is

$$\sigma(\bar{p}) \begin{cases} = \frac{1}{2}\sqrt{\sigma_{p_2}^2 + \sigma_{p_3}^2} & \text{for } 3H - P \\ \\ = \frac{1}{4}\sqrt{\sigma_{p_2}^2 + \sigma_{p_3}^2 + \sigma_{p_4}^2 + \sigma_{p_5}^2} & \text{for } 5h - P \end{cases} \tag{3.40}$$

Then, the uncertainty in total pressure coefficient, $\sigma(C_{pt})$ can be expressed as

$$\sigma(C_{pt}) = \sqrt{\left(\frac{\partial C_{pt}}{\partial p_{0t}}\sigma p_{0t}\right)^2 + \left(\frac{\partial C_{pt}}{\partial p_{t2}}\sigma p_{1t}\right)^2 + \left(\frac{\partial C_{pt}}{\partial C_0}\sigma C_0\right)^2 + \left(\frac{\partial C_{pt}}{\partial \rho}\sigma \rho\right)^2} \tag{3.41}$$

where

$$\frac{\partial C_{pt}}{\partial p_{0t}} = \frac{2}{\rho {C_0}^2},$$

$$\frac{\partial C_{pt}}{\partial p_{1t}} = \frac{-2}{\rho {C_0}^2},$$

$$\frac{\partial C_{pt}}{\partial C_0} = \frac{-4(p_{1t} - p_{0t})}{\rho {C_0}^3},$$

and

$$\frac{\partial C_{pt}}{\partial \rho} = \frac{-2(p_{1t} - p_{0t})}{\rho^2 {C_0}^2}.$$

Replacing the partial derivatives, the equation (3.41) becomes

$$\sigma(C_{pt}) = \sqrt{\left[\frac{2\sigma p_{0t}}{\rho {C_0}^2}\right]^2 + \left[\frac{-2\sigma p_{1t}}{\rho {C_0}^2}\right]^2 + \left[\frac{-4\Delta p_t}{\rho {C_0}^3}\sigma C_0\right]^2 + \left[\frac{-2\Delta p_t}{\rho^2 {C_0}^2}\sigma \rho\right]^2} \tag{3.42}$$

with $\Delta p_t = (p_{1t} - p_{0t})$. After substituting the respective values for the uncertainty of inlet and outlet total pressure, fluid density, and flow velocity in equation (3.42) give an overall uncertainty of the total pressure coefficient. The results of this calculation are presented in Fig. 3.21 for the midspan flow and in Fig. 3.22 for the endwall flow.

Figure. 3.21 shows a typical trend of absolute uncertainty in the total pressure coefficient measured by the three-hole probe. The uncertainty is very low outside the wake region but its value significant increases in the wake. Moreover, it is seen that the peak values of absolute uncertainty increase with increasing closing degree. These absolute uncertainty values are about 0.28 at fully opening cascade and increases to about 0.34 and around 0.47 at δ = 10% for CPS and CSS, respectively.

Die approbierte gedruckte Originalversion dieser Dissertation ist an der TU Wien Bibliothek verfügbar.
The approved original version of this doctoral thesis is available in print at TU Wien Bibliothek.
TU Bibliothek Your knowledge hub WIEN

Figure 3.22 is a typical result of uncertainty in the total pressure coefficient documented by the five-hole probe. It is seen that high uncertainty dominates the endwall region with its peak absolute value is approximately 0.38. This is often related to the accumulation effect of positive and negative vorticity in this region. Outside the endwall region, the uncertainty decreases in the other region where the total pressure coefficient is very large, especially in freestream and midspan region.

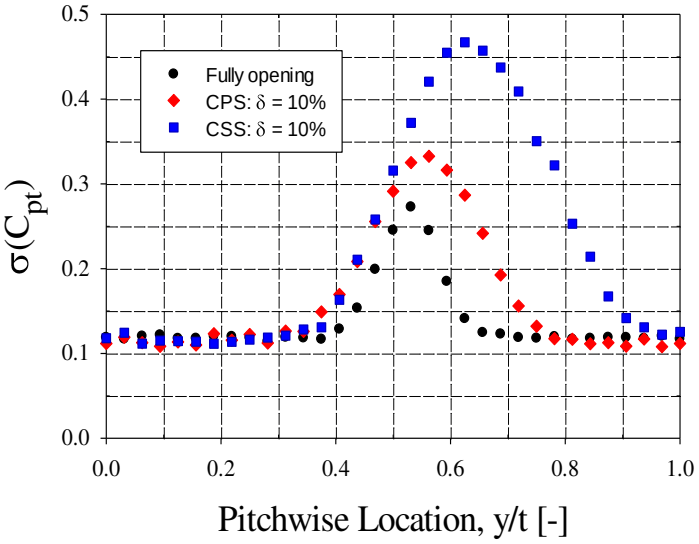

Figure 3.21 Distribution of uncertainty in total pressure coefficient at fully opening cascade, and at δ = 10% for CPS and CSS from the three-hole probe

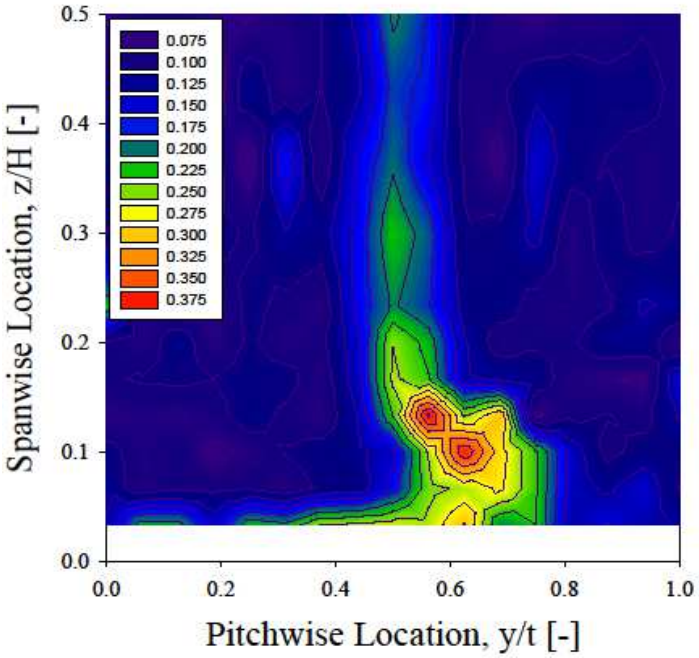

Figure 3.22 Distribution of uncertainty in total pressure coefficient at fully opening cascade (δ = 0%) from the five-hole probe

Die approbierte gedruckte Originalversion dieser Dissertation ist an der TU Wien Bibliothek verfügbar.
The approved original version of this doctoral thesis is available in print at TU Wien Bibliothek.
TU Bibliothek Your knowledge hub WIEN

It should be noted that the calculations neglected the uncertainties that arise during the calibration process. As the calibration data are used to calculate the total and static pressure at the outlet, involving these uncertainties into the calculation would influence the overall uncertainty of the total pressure coefficient.

Uncertainties from the calibration: Before detailing the method to calculate uncertainty in the calibration measurements, the calibration process must first be understood. The pressure probes must be calibrated for a range of different operating points before it can be used to investigate unknown flow fields. In the probe calibration procedure, for different dimensionless coefficients are calculated for each operating point, which can then be used in determining the flow parameters of unknown flow fields, is presented in section 3.4.3 (for three-hole probe) and 3.4.4 (for five-hole probe).

During the calibration process, five different pressures for three-hole probe data and seven different pressures for five-hole probe data are measured. These pressures are the total pressure in the flow channel, the static pressure in the test section, and the three-hole probe pressures and five-hole probe pressures. The three and five pressures measured in the probe are defined according to Fig. 3.14 for 3H-P and Fig. 3.16 for 5H-P. Once the data has been measured, the calibration coefficients can be calculated by

$$k_t = \frac{\bar{p} - p_t}{p_1 - \bar{p}}, k_s = \frac{\bar{p} - p_s}{p_1 - \bar{p}}, k_\beta = \frac{p_2 - p_3}{p_1 - \bar{p}}, \text{and } k_\gamma = \frac{p_4 - p_5}{p_1 - \bar{p}} \tag{3.43}$$

where k_β and k_γ are direction coefficients for yaw angle and pitch angle, respectively, k_t and k_s are total pressure and static pressure coefficient. Meanwhile, average pressure can be determined using equation (3.9) for 3H-P and equation (3.12) for 5H-P. These parameters are the values collected during the calibration process.

As seen in the earlier section, the calibration coefficients k_t and k_s calculated during the calibration process are used to calculate the total pressure and static pressure at the outlet for the measurement data. To incorporate the uncertainty from the calibration process into these values, the uncertainty in calibration coefficients k_t and k_s must be calculated. The uncertainty in k_t is calculated by

$$\sigma(k_t) = \sqrt{\left(\frac{\partial k_t}{\partial p_t}\sigma p_t\right)^2 + \left(\frac{\partial k_t}{\partial p_1}\sigma p_1\right)^2 + \left(\frac{\partial k_t}{\partial \bar{p}}\sigma \bar{p}\right)^2} \tag{3.44}$$

where

$$\frac{\partial k_t}{\partial p_t} = -\frac{1}{(p_1 - \bar{p})},$$

$$\frac{\partial k_t}{\partial p_1} = -\frac{(\bar{p} - p_t)}{(p_1 - \bar{p})^2},$$

Die approbierte gedruckte Originalversion dieser Dissertation ist an der TU Wien Bibliothek verfügbar.
The approved original version of this doctoral thesis is available in print at TU Wien Bibliothek.

and

$$\frac{\partial k_t}{\partial \bar{p}} = \frac{(p_1 - p_t)}{(p_1 - \bar{p})^2}.$$

Substituting the partial derivatives, the equation (3.44) becomes

$$\sigma(k_t) = \sqrt{\left[-\frac{1}{(p_1 - \bar{p})}\sigma p_t\right]^2 + \left[-\frac{(\bar{p} - p_t)}{(p_1 - \bar{p})^2}\sigma p_1\right]^2 + \left[\frac{(p_1 - p_t)}{(p_1 - \bar{p})^2}\sigma \bar{p}\right]^2} \tag{3.45}$$

with average pressure is calculated by using equations (3.40).

The equipment used to measure the pressures are the same as for the linear cascade hence the statistical uncertainties of these pressure variables can be determined in the same manner as described for the linear cascade in the previous section. The uncertainty in k_s is calculated by using equation

$$\sigma(k_s) = \sqrt{\left(\frac{\partial k_s}{\partial p_s}\sigma p_s\right)^2 + \left(\frac{\partial k_s}{\partial p_1}\sigma p_1\right)^2 + \left(\frac{\partial k_s}{\partial \bar{p}}\sigma \bar{p}\right)^2} \tag{3.46}$$

with

$$\frac{\partial k_s}{\partial p_s} = -\frac{1}{(p_1 - \bar{p})},$$

$$\frac{\partial k_s}{\partial p_1} = -\frac{(\bar{p} - p_s)}{(p_1 - \bar{p})^2},$$

and

$$\frac{\partial k_s}{\partial \bar{p}} = \frac{(p_1 - p_s)}{(p_1 - \bar{p})^2}.$$

after replacing the partial derivatives, the equation (3.46) can be written as

$$\sigma(k_s) = \sqrt{\left[-\frac{1}{(p_1 - \bar{p})}\sigma p_s\right]^2 + \left[-\frac{(\bar{p} - p_s)}{(p_1 - \bar{p})^2}\sigma p_1\right]^2 + \left[\frac{(p_1 - p_s)}{(p_1 - \bar{p})^2}\sigma \bar{p}\right]^2}. \tag{3.47}$$

after the uncertainties in the total pressure and static pressure coefficients have been calculated, the method used to calculate the uncertainty in total pressure and static pressure in the linear cascade rig must be recalculated. Then the total pressure at the outlet in the linear cascade was calculated as

$$p_t = p_1 - k_t(p_1 - \bar{p}). \tag{3.48}$$

The uncertainty in outlet total pressure should now be calculated by

Die approbierte gedruckte Originalversion dieser Dissertation ist an der TU Wien Bibliothek verfügbar.
The approved original version of this doctoral thesis is available in print at TU Wien Bibliothek.
TU Bibliothek Your knowledge hub WIEN

$$\sigma(p_t) = \sqrt{\left(\frac{\partial p_t}{\partial k_t}\sigma k_t\right)^2 + \left(\frac{\partial p_t}{\partial p_1}\sigma p_1\right)^2 + \left(\frac{\partial p_t}{\partial \bar{p}}\sigma \bar{p}\right)^2} \tag{3.49}$$

where

$$\frac{\partial p_t}{\partial k_t} = \bar{p} - p_1,$$

$$\frac{\partial p_t}{\partial p_1} = 1 - k_t,$$

and

$$\frac{\partial p_t}{\partial \bar{p}} = k_t.$$

by substituting the partial derivatives, the equation (3.49) can be expressed as

$$\sigma(p_t) = \sqrt{[(\bar{p} - p_1)\sigma k_t]^2 + [(1 - k_t)\sigma p_1]^2 + [(k_t)\sigma \bar{p}]^2}. \tag{3.50}$$

Then, as described in the section 3.6.3, the static pressure at the outlet in the linear cascade was then calculated as

$$p_s = \bar{p} - k_s(p_1 - \bar{p}). \tag{3.51}$$

The uncertainty in outlet static pressure should now be calculated by

$$\sigma(p_s) = \sqrt{\left(\frac{\partial p_s}{\partial k_s}\sigma k_s\right)^2 + \left(\frac{\partial p_s}{\partial p_1}\sigma p_1\right)^2 + \left(\frac{\partial p_s}{\partial \bar{p}}\sigma \bar{p}\right)^2} \tag{3.52}$$

with

$$\frac{\partial p_s}{\partial k_s} = \bar{p} - p_1,$$

$$\frac{\partial p_s}{\partial p_1} = -k_s,$$

and

$$\frac{\partial p_s}{\partial \bar{p}} = 1 + k_s.$$

by replacing the partial derivatives, the equation (3.52) can be written as

$$\sigma(p_s) = \sqrt{[(\bar{p} - p_1)\sigma k_s]^2 + [(-k_s)\sigma p_1]^2 + [(1 + k_s)\sigma \bar{p}]^2}. \tag{3.53}$$

The analysis above for the calculating the uncertainty in the calibration process has not been involved in the overall calculations in this investigation. This method is introduced for calculating these uncertainties into future works.

Die approbierte gedruckte Originalversion dieser Dissertation ist an der TU Wien Bibliothek verfügbar.
The approved original version of this doctoral thesis is available in print at TU Wien Bibliothek.
TU Bibliothek Your knowledge hub WIEN

4 Results of the fully opening cascade

4.1 Two-dimensional flow field

The aerodynamically midspan flow features of the turbine blade cascade were evaluated experimentally through the downstream measurement plane, and the results are presented in this section prior to discussing the flow behaviors. All data presented in the later result chapters were taken at the inlet flow angle 90°. Measurements were performed by pressure taps at the blade surfaces, and the three-hole probe at 30% axial chord downstream of the cascade in one pitch location.

4.1.1 Blade loading

Blade loading distribution in term of blade static pressures along the blade surfaces were measured by mean of pressure taps. The measurement procedures and the probe position details are outlined in section 3.4.2. Experimental description of blade pressure distribution at midspan is expressed as a pressure coefficient, C_p, which is defined as

$$C_p = \frac{(p_s - p_0)}{\frac{1}{2}\rho C_0^2}. \tag{4.1}$$

This distribution of C_p is plotted along the blade chord at various axial positions given by the x/b ratio and shown in Fig. 4.1. Some important observations can be drawn based on this figure as follows:

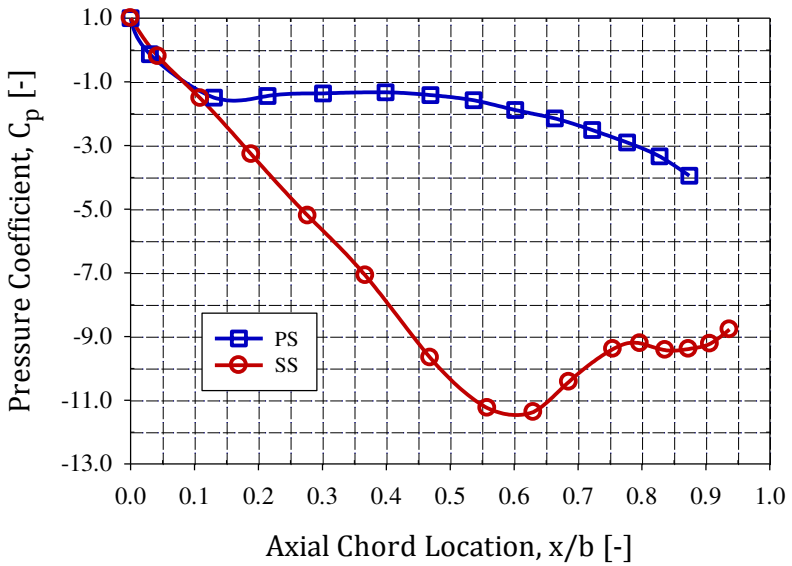

Figure 4.1 Static pressure distribution on the blade surface at inlet flow angle 90°

Die approbierte gedruckte Originalversion dieser Dissertation ist an der TU Wien Bibliothek verfügbar.
The approved original version of this doctoral thesis is available in print at TU Wien Bibliothek.
TU Bibliothek Your knowledge hub WIEN

On the pressure surface, a strong favorable pressure gradient occurs in a limited area of pressure side from leading edge up to x/b = 0.1 which indicates the flow undergoes strong acceleration, then followed slowly decreases of favorable pressure gradient up to x/b = 0.6, and from this location the onset of boundary layer is again moderately accelerated with the static pressure decreases slightly towards the trailing edge.

On the suction surface, the favourable pressure gradient extends from the leading edge to the suction peak, apart from a weak inflection point at around x/b = 0.6. Downstream of the suction peak displays strong adverse pressure with increase static pressure up to x/b = 0.75, and the flow is decelerated in this location. Then, again the adverse pressure gradient slightly grows towards trailing edge. The lowest suction surface static pressure coefficient is about -11.5 and occurred at x/b = 0.6.

In the leading edge, the exact position of a stagnation point cannot be determined by the measurement result, because of the limited number of the measurement points. According to the definition, the stagnation point locates at the point where the static pressure is at its maximum value. For this investigation, the C_p at the stagnation point is approximately 1.0 at about x/b = 0.0 as depicted in the plot.

4.1.2 Exit flow angle

The exit flow angle is one of the most crucial parameters that substantially influence the performance of the cascade. The changes of exit flow angle were measured using the three-hole probe and are plotted in Fig. 4.2. It can be seen that that in the wake region a large variation and deviation of the flow angle occur. The reason for higher deflection angle on the suction side wake is transport process caused by the flow meets high velocity gradient across the wake behind blade. Moreover, the distribution shows that the high nonuniform of the flow covers area in the wake from about y/t = 0.35 to 0.75. Outside this region, the flow is slightly more uniform in the undistributed freestream region at both the pressure side and suction side downstream of the cascade.

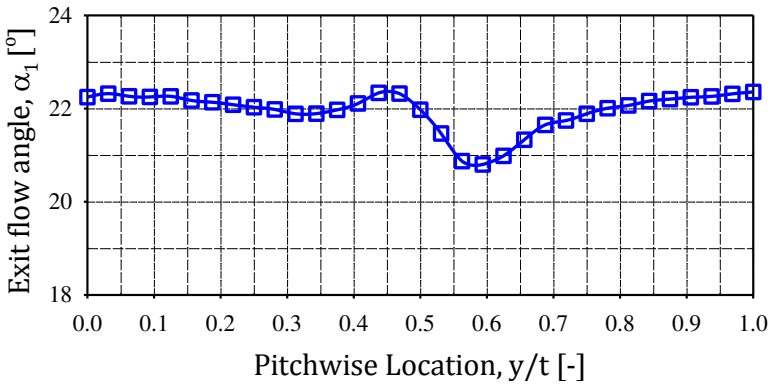

Figure 4.2 Exit flow angle distribution of the cascade at inlet flow angle 90°

Die approbierte gedruckte Originalversion dieser Dissertation ist an der TU Wien Bibliothek verfügbar.
The approved original version of this doctoral thesis is available in print at TU Wien Bibliothek.
TU Bibliothek Your knowledge hub WIEN

4.1.3 Nondimensional velocity

The wake profile in term of nondimensional velocity distribution was measured by using of three-hole probe downstream of cascade and is shown by the top plot in Fig. 4.3. The velocity was normalized by dividing by the inlet velocity at midspan. The wake can be associated with the high defect region of the velocity in the pitchwise location. In this plot, the small asymmetry of the wake is occurred. This asymmetry is depicted by the suction side wake which is thicker than the pressure side wake. This is mostly because of different growth and development of boundary layers in both blade surfaces. On the pressure side, the thickness of boundary layer is much smaller than on the suction side due to the local flow undergoes continuous acceleration. On the suction side, local freestream velocities are higher, and the boundary layers strongly developed, which causes a thicker wake at once downstream of trailing edge. Moreover, it is seen that the velocity distribution is very nearly unchanged in undistributed region, and it drastically decreases in the wake with minimum value of C_1/C_0 reaches 2.54 at the wake axis about y/t = 0. 53.

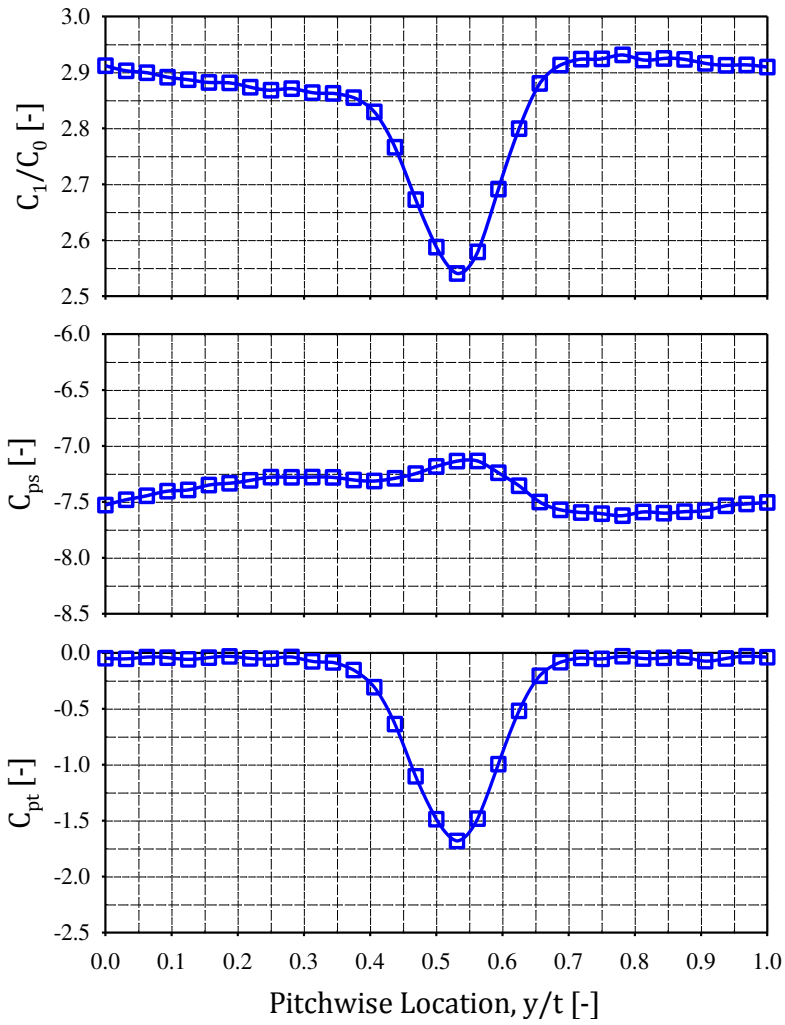

Figure 4.3 Wake profile downstream of the cascade at inlet flow angle 90°

Die approbierte gedruckte Originalversion dieser Dissertation ist an der TU Wien Bibliothek verfügbar.
The approved original version of this doctoral thesis is available in print at TU Wien Bibliothek.
TU Bibliothek Your knowledge hub WIEN

4.1.4 Static pressure coefficient

The distribution of static pressure coefficient downstream of the cascade is given by middle plot in Fig. 4.3. The static pressure was obtained from the three-hole probe data at each point in the measurement plane. The static pressure was normalized by the dynamic pressure at the inlet test section and is defined as

$$C_{ps} = \frac{(p_{1s} - p_{0s})}{\frac{1}{2}\rho C_0^2} \tag{4.2}$$

with p_{1s} is the static pressure at the outlet, p_{0s} is the static pressure at the inlet, C_0 is the inlet flow velocity at midspan, and C_{ps} is static pressure coefficient. From the plot, it is noticeable that the static pressure is not quite uniform along pitchwise location. There is a gradual increase in static pressure toward the wake centre which can be attributed to the potential flow process occurred outside of wake. Then, static pressure is rapidly decreasing then followed by gradually increasing at $0.7 < y/t < 1.0$.

4.1.5 Total pressure coefficient

The total pressure coefficient is among the most important parameter to quantify the losses in the turbine cascade. This parameter is defined as a difference of total pressure between exit and inlet station divided by the dynamic pressure at the test section inlet as

$$C_{pt} = \frac{(p_{1t} - p_{0t})}{\frac{1}{2}\rho C_0^2} \tag{4.3}$$

where p_{1t} is the total pressure at outlet station, p_{0t} is the total pressure at inlet station, C_0 is inlet freestream velocity at midspan, and C_{pt} is total pressure coefficient. The distribution of total pressure coefficient was measured by using the three-hole probe and is illustrated by the bottom plot in Fig. 4.3. The wake is represented by the high-pressure deficit regions along the pitch location. This wake is strongly influenced by the history of the pressure gradient from upstream leading edge to downstream trailing edge and condition of blade boundary layers. From this plot, the minimum value of total pressure coefficient is around -1.75 located in the wake.

4.1.6 Turbulence intensity

Figure 4.4 is the turbulence intensity downstream of the cascade measured by a single hot-wire anemometry. This plot describes a root mean square velocity fluctuation normalized based on the inlet velocity and plotted against normalized pitchwise location. The curve shows typical feature of turbulence intensity of the flow with a peak at the large velocity

Die approbierte gedruckte Originalversion dieser Dissertation ist an der TU Wien Bibliothek verfügbar.
The approved original version of this doctoral thesis is available in print at TU Wien Bibliothek.
TU Bibliothek Your knowledge hub WIEN

defect region. The asymmetric turbulence profile with maxima at the wake reflects the different sizes of the blade boundary layers. From this plot, increased turbulence intensity due to the growth and developed of the boundary layers can be seen from 35% to 70% pitchwise location. This intensity remained uniform in the undistributed region until the wake was reached and its value is around 1.5%, and it increases up to 5.25% in the wake. The profile shows a double peak which is reaching maximum of 3.75% at about y/t = 0.47 in the pressure side, and 5.25% at y/t = 0.6 in the suction side.

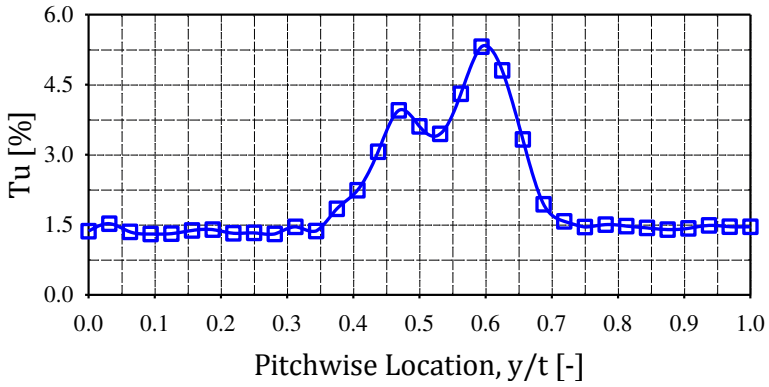

Figure 4.4 Turbulence intensity distribution of the cascade at inlet flow angle 90°

4.2 Three-dimensional flow field

The discussions in this section are primarily based on the measurement results of various flow parameters such as flow angles in the pitchwise and spanwise direction, flow velocity, secondary kinetic energy, vorticity and total pressure coefficient. Area traverses were performed with a five-hole pneumatic probe downstream of the cascade. The measurement region extends in the horizontal direction from y/t = 0 to 1 over one pitch of the passage, and in the vertical direction from z/H = 0 to 0.5 which corresponds to the endwall and midspan, respectively. The blade trailing edge is positioned at y/t = 0.5, where t denotes the cascade spacing (pitch).

4.2.1 Pitchwise flow angle

Figure 4.5a shows the result of pitchwise flow angle distribution, obtained by the five-hole probe downstream of the cascades. The measurement procedures and the probe details are outlined in section 3.5. In this plot, the flow field is dominated by a passage vortex which is responsible for the overturning in the endwall region below z/H = 0.2. Large gradient of the pitch flow angles is occurred in the area occupied by the passage vortex with local pitch angle is greater than mean flow angle on one side of the vortex, and less on the other side. Based on the isoclinal method that was introduced by Binder and Romey [4], the core

Die approbierte gedruckte Originalversion dieser Dissertation ist an der TU Wien Bibliothek verfügbar.
The approved original version of this doctoral thesis is available in print at TU Wien Bibliothek.
TU Bibliothek Your knowledge hub WIEN

of this passage vortex is located between maximum and minimum value of the parallel isoclines at about y/t = 0.55 and about z/H = 0.13. Even though this plot can be used to identify vortices and its cores, however, they have their limitations. This isoclinal plot cannot determine the sign, size and intensity of the vortex.

4.2.2 Spanwise flow angle

Distribution of spanwise flow angle downstream of the cascade was measured by the five-hole probe and is plotted in Fig. 4.5b. Again, the probe details and experimental methods are presented in section 3.5. This plot describes the isoclines contours of spanwise flow angle caused by secondary flow and endwall boundary layer interaction. From this plot, the results confirm that a strong effect of endwall boundary layer at about the endwall to z/H = 0.20, showing the large gradient of spanwise flow angle occur in this region. It also is seen that the locations of vortex core are less clear for spanwise flow angle than they were for pitchwise flow angle. However, using a similar isoclinal method of Binder and Romey [4] as mentioned in previous case, the position of vortex core still can be seen, and it is concentrated at the point in the parallel isoclines where spanwise flow angle $\beta_1 = 0^o$, which is between minimum $\beta_1 = -2.5^o$ and maximum $\beta_1 = 2.5^o$.

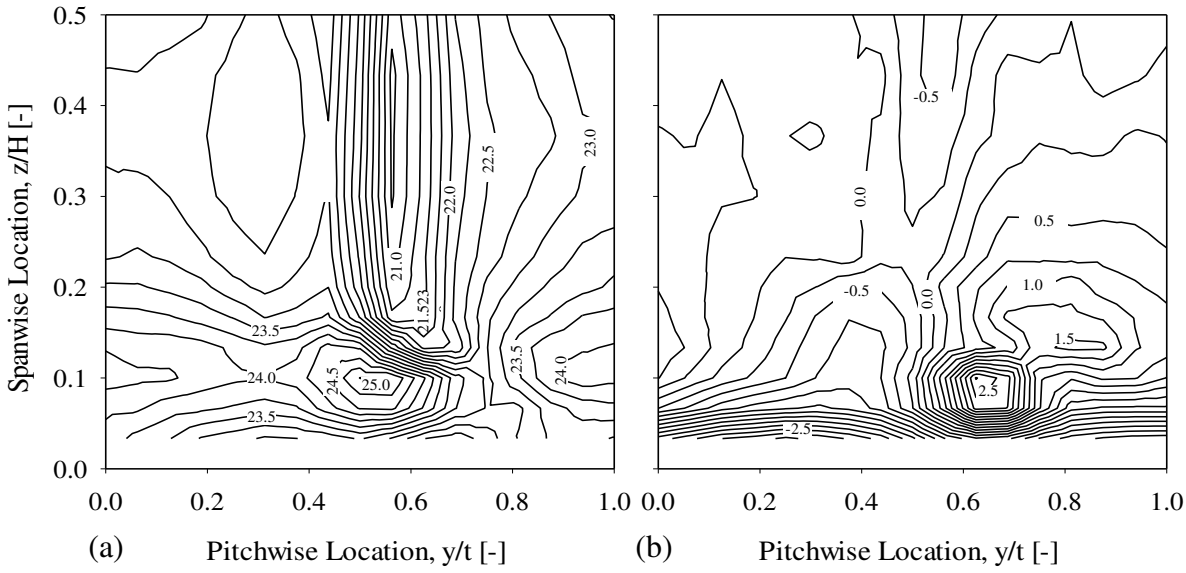

Figure 4.5 Contour plot: (a) pitchwise flow angle and (b) spanwise flow angle for a fully opening condition at inlet flow angle 90°

4.2.3 Nondimensional velocity

Figure 4.6a presents exit velocity contours downstream of blade #4 normalized with the inlet freestream velocity and measured by using the five-hole probe from midspan to the

Die approbierte gedruckte Originalversion dieser Dissertation ist an der TU Wien Bibliothek verfügbar.
The approved original version of this doctoral thesis is available in print at TU Wien Bibliothek.
TU Bibliothek Your knowledge hub WIEN

endwall. Further details measurement technique and probe features are described in section 3.5. Contour labels on the plots show the value of the normalized quantity. The contour plot shows the reduction in exit velocity as the wake is approached and increasing in complexity structures as the endwall is approached. This plot reveals the wake which is the vertically oriented regions of velocity defect and extends from z/H = 0.15 up to midspan. The secondary flow effect from blade #3 dominate the endwall region, revealed as the region of high velocity defect, and occupying the area downstream of blade #4 from the lower endwall up to z/H = 0.15. The highest value of this velocity defect is seen near the endwall at y/t = 0.6 and z/H = 0.1, which is due to the secondary flows.

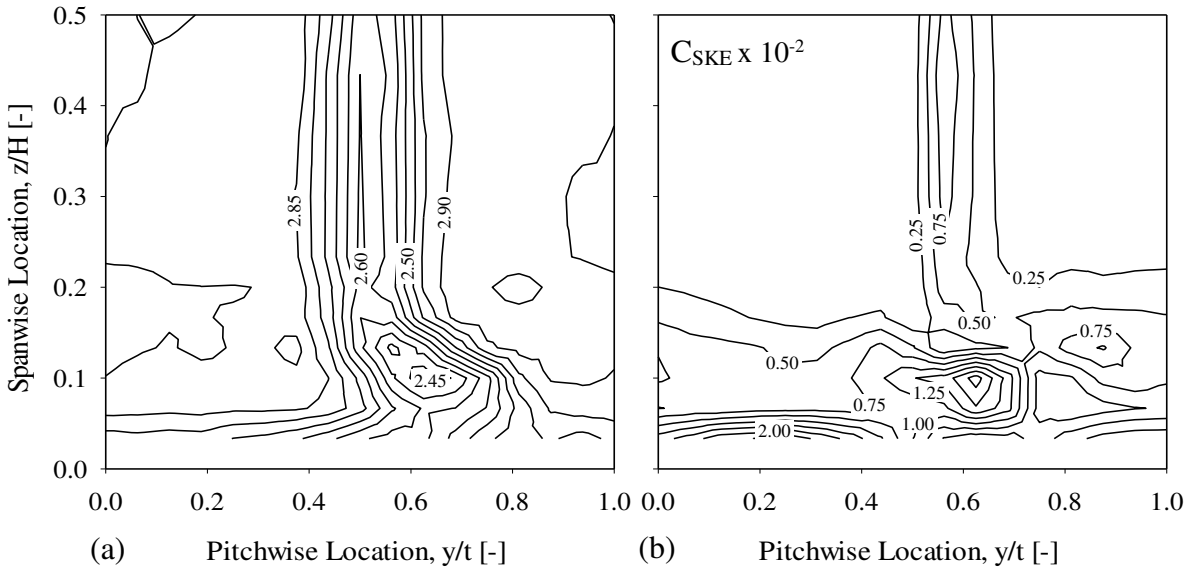

Figure 4.6 Contour plot: (a) nondimensional velocity and (b) secondary kinetic energy coefficient for fully opening condition at inlet flow angle 90°

4.2.4 Secondary kinetic energy coefficient

Secondary kinetic energy is an important parameter associated with the secondary flow structures as well as related to the production of secondary loss in the cascade. This parameter is predominantly a function of the secondary velocities. The secondary kinetic energy is calculated as

$$\mathrm{SKE} = \frac{1}{2}\rho\left(C_{ys}^2 + C_{zs}^2\right) \tag{4.4}$$

where $C_{ys} = C_1 \cos\beta_1 \sin\left(\alpha_1 - \overline{\alpha}_{1MS}\right)$, $C_{zs} = C_1 \cos\beta_1$, with α_1 is measured exit flow angle, $\overline{\alpha}_{1MS}$ is the reference flow angle at midspan and $\beta_1$is spanwise flow angle.

The secondary kinetic energy is normalized by the kinetic energy on the inlet center line of the cascade and defined as

Die approbierte gedruckte Originalversion dieser Dissertation ist an der TU Wien Bibliothek verfügbar.
The approved original version of this doctoral thesis is available in print at TU Wien Bibliothek.
TU Bibliothek Your knowledge hub WIEN

$$C_{SKE} = \frac{\left(C_{ys}^2 + C_{zs}^2\right)}{C_0^2} \tag{4.5}$$

with C_{SKE} is the secondary kinetic energy coefficient, and C_0 is the inlet velocity measured in midspan of the blade cascade.

Figure 4.6b depicts the distribution of secondary kinetic energy coefficient downstream of the cascade. This contour shows the strength of the pitchwise crossflow near the endwall associated with vortex structures. It is seen that a high value of secondary kinetic energy resulting from the overturning driven by these vortices in the passage. The peak value of secondary kinetic energy coefficient is about 1.25 x 10^{-2} at y/t = 0.65 and z/H = 0.1 from the endwall surface. From this plot, the horseshoe vortex produced the level of secondary kinetic energy coefficient as high as 2.0 x 10^{-2} closer to the endwall. These results are irrecoverable loss downstream of the cascade.

4.2.5 Nondimensional vorticity

The complex structure of three-dimensional flow downstream of the cascade and endwall region can be seen by examining the vorticity. Such interesting parameters are determined here due to it is a property that is useful for identifying secondary flow structures and quantifying their strength and sense of rotation. The vorticity is defined as the curl of the velocity vector and is mathematically expressed as

$$\vec{\omega} = \nabla \times \vec{C} \tag{4.6}$$

where $\vec{\omega}$ stands for the vorticity and $\vec{C}$ is velocity vector.

$$\vec{C} = \begin{pmatrix} C_x \\ C_y \\ C_z \end{pmatrix}. \tag{4.7}$$

The first step in determining the axial vorticity is to calculate the velocity vector in the Cartesian coordinate. The axial vorticity is determined from the velocity gradients as

$$\omega_x = \frac{\partial C_z}{\partial y} - \frac{\partial C_y}{\partial z} \tag{4.8}$$

here, C_z and z are the spanwise velocity and its direction, while C_y and y are the pitchwise velocity and its direction. In this coordinate system, positive vorticity occurs where the secondary flow has a counterclockwise rotation. So, it is essential to understand the physical meaning of the axial vorticity. A negative vorticity means that the rate of change of the pitchwise velocity is higher than the rate of change of spanwise velocity, therefore this results in a clockwise rotating vortex. Otherwise, positive vorticity means that the rate of change of the pitchwise is less than the rate of change of the spanwise velocity, and this

Die approbierte gedruckte Originalversion dieser Dissertation ist an der TU Wien Bibliothek verfügbar.
The approved original version of this doctoral thesis is available in print at TU Wien Bibliothek.
TU Bibliothek Your knowledge hub WIEN

results in a counterclockwise rotating vortex. The pitchwise vorticity cannot be determined directly from the measurement. However, this vorticity can be estimated using a Helmholtz equation as follows

$$\vec{C} \times \vec{\omega} = \frac{1}{\rho} \nabla p_t \tag{4.9}$$

where p_t is the total pressure and ρ is the air density. Thus, y-component of this relation for the vorticity are expressed as

$$\omega_y = \frac{1}{C_x}\left(\frac{1}{\rho}\frac{\partial p_t}{\partial z} + C_y \omega_x\right) \tag{4.10}$$

The y-component of this relation can be applied to determine the pitchwise vorticity. Thus, the streamwise vorticity is resultants of axial and pitchwise vorticity in the streamwise direction which is calculated by

$$\omega_s = \omega_x \sin \bar{\alpha}_{1MS} - \omega_y \cos \bar{\alpha}_{1MS} \tag{4.11}$$

where ω_s is streamwise vorticity and $\bar{\alpha}_{1MS}$ is average exit flow angle in midspan. The nondimensional streamwise vorticity, therefore, is expressed as

$$\Omega_S = \frac{\omega_s C}{C_0} \tag{4.12}$$

with C is the chord length of blade cascade. The plot of nondimensional streamwise vorticity can be used for finding the motion of the fluid flow. The position of measured peak vorticity is applied to find the center of passage vortex.

Contour plot of nondimensional streamwise vorticity downstream of the cascade used to describe secondary flow structure is shown in Fig. 4.7a. Even though the velocity vectors of the vortex flow have not been documented in the present study, however, some analyses about their formation within the passage can still be drawn based on the vorticity contour plots. The vortex core can be found which is defined as the point where the vorticity is a maximum, and the circulating flow is seen rotating around the core of the vortex. Based on the contour plot, three distinct secondary flow structures can be identified in the endwall region around downstream of the blade #4. These vortex structures are the passage vortex, the counter-rotating vortex, and the suction side leg of the horseshoe vortex. The passage vortex with highest core strength about -3.15 is found at about y/t = 0.75 and z/H = 0.1 above the endwall surface extends to about z/H = 0.2. The counter-rotating vortex with largest core intensity +1.40 is detected at around y/t = 0.5 and z/H = 0.15. The suction side leg of the horseshoe vortex with maximum intensity -2.8 occupies around z/H < 0.1. The passage vortex and suction side leg of the horseshoe vortex have negative vorticity (clockwise circulation) while the counter-rotating vortex has positive vorticity (counter-clockwise circulation). These results confirm that the endwall flow downstream of the cascade is highly complex three-dimensional flow.

Die approbierte gedruckte Originalversion dieser Dissertation ist an der TU Wien Bibliothek verfügbar.
The approved original version of this doctoral thesis is available in print at TU Wien Bibliothek.
TU Bibliothek Your knowledge hub WIEN

Referring to the fundamental analysis in the work of Langston [28] and Wang et al. [47], the existence of these various vortices is interpreted. The endwall boundary layer flow approaching the leading edge of blade #4 separates and rolls up into the familiar horseshoe vortex found around leading edge standing out of a shear flow. The leg of the vortex on the suction side is moved spanwise away from the endwall by the secondary flow in the passage, and the leg of the vortex on the pressure side is convected across the passage to join the suction surface of an adjacent blade. The result of this convection in the endwall suction surface corner generates a counter-rotating vortex. Moreover, the pressure side leg of horseshoe vortex of blade #3 migrated from the pressure side to the next suction side of blade #4 due to the cross-passage pressure gradient. The passage vortex generated by the traverse pressure gradient creates an endwall flow with or without the pressure side leg of horseshoe vortex from neighboring blade #3. The suction side leg of horseshoe vortex moved up over the passage vortex due to forces exerted by the passage vortex. The suction side leg of horseshoe vortex of blade #4 may remain attached at the suction side and then eventually interact with both passage vortex and suction side boundary layer to generate corner or counter-rotating vortex.

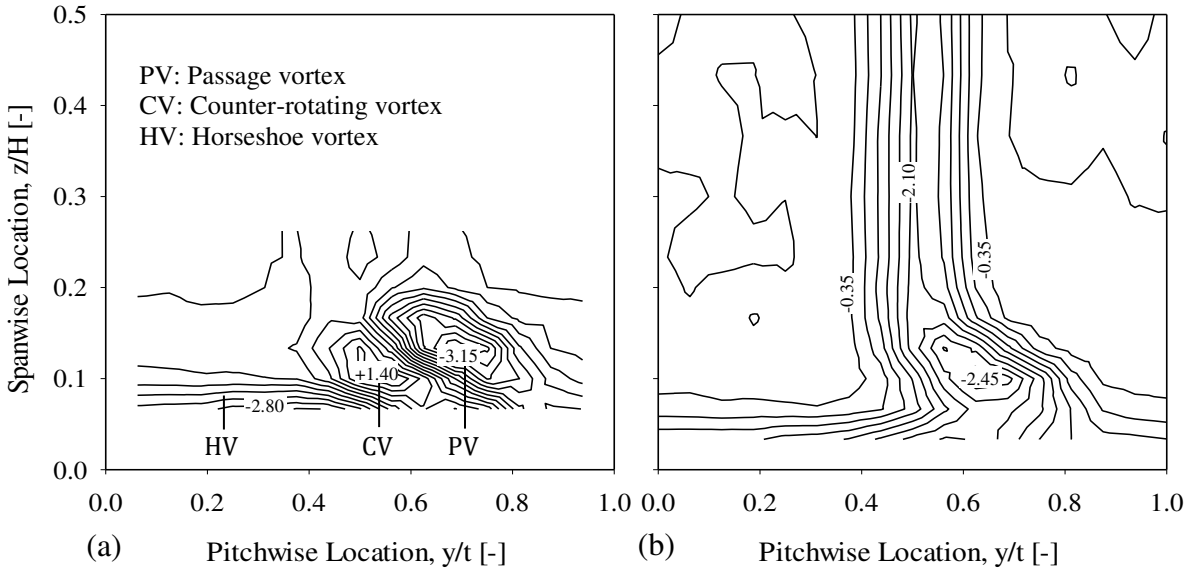

Figure 4.7 Contours plots: (a) nondimensional vorticity and (b) total pressure coefficient for fully opening cascade at inlet flow angle 90°

4.2.6 Total pressure coefficient

Another method to analyze the three-dimensional flows is through total pressure field. It is defined as total pressure coefficient, which can be noted as the losses due to dissipation of kinetic energy caused by viscous and mixing effects in the flow. Figure 4.7b illustrates the contour map of total pressure coefficient downstream of the cascade. The values for the contours are created in similar manner to equation (4.3). This contour plot can be used to

Die approbierte gedruckte Originalversion dieser Dissertation ist an der TU Wien Bibliothek verfügbar.
The approved original version of this doctoral thesis is available in print at TU Wien Bibliothek.
TU Bibliothek Your knowledge hub WIEN

find locations of vortex core where it corresponds to the peak of total pressure deficit. It is seen that secondary flow region covers at least 20% of span from the endwall. Moreover, a well-developed two-dimensional uniform flow appears from 20% of span to midspan. This plot shows that low-pressure deficit of C_{pt} = -0.35 from freestream as well as high-pressure deficit of C_{pt} = -2.45 from boundary layer of the endwall are being pulled by a passage vortex exiting near suction side downstream of the blade #4. The maximum total pressure deficit associated with vortex core is found at y/t near 0.70 and z/H about 0.10. It is highest loss caused by secondary flow vortices and their dissipation.

4.2.7 Pitchwise-averaged distribution

The use of pitchwise averaging in a three-dimensional flow such as in this analysis releases much of the flow detail. Any spanwise distribution of a flow feature will considerably change the pitchwise-averaged value. It is important to compare the results in this way, so that any specific characteristics may be noted. The flow angles along with nondimensional velocity, total pressure and secondary kinetic energy coefficient are presented.

Figure 4.8 displays averaged pitchwise flow angle downstream of the cascade measured along span with the endwall is at z/H = 0.0 and midspan is at z/H = 0.5. This plot is useful to understand the flow uniformity along span from midspan to the endwall. Pitchwise flow angle distribution was determined through pitchwise-averaging the pitchwise flow angle and is calculated as

$$\bar{\alpha}_1 = \frac{\int_0^t \alpha_1 \, C_1 \cos \beta_1 \sin \alpha_1 \, dy}{\int_0^t C_1 \cos \beta_1 \sin \alpha_1 \, dy}. \tag{4.13}$$

The presented plot shows a typical of the endwall flow with overturning occurs near the endwall and followed underturning towards midspan. The presence of secondary flows and their interaction cause a peak of underturning at about z/H = 0.1.

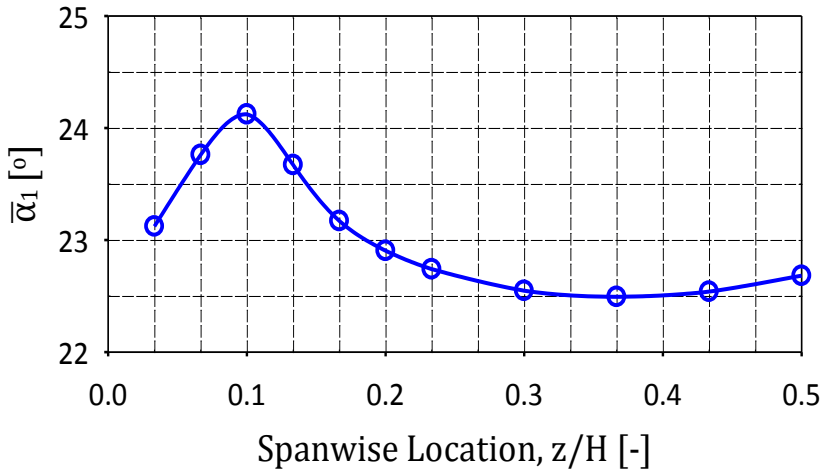

Figure 4.8 Averaged pitchwise flow angle as a function of span at fully opening cascade

Die approbierte gedruckte Originalversion dieser Dissertation ist an der TU Wien Bibliothek verfügbar.
The approved original version of this doctoral thesis is available in print at TU Wien Bibliothek.
TU Bibliothek Your knowledge hub WIEN

Other parameter which characterizes the endwall flow is averaged spanwise flow angle presented in Fig. 4.9. In this plot, as before the endwall is at z/H = 0.0 and midspan is at z/H = 0.5. This curve distribution was calculated by the pitchwise-averaging the spanwise flow angle as

$$\bar{\beta}_1 = \frac{\int_0^t \beta_1 \, C_1 \cos \beta_1 \sin \alpha_1 \, dy}{\int_0^t C_1 \cos \beta_1 \sin \alpha_1 \, dy}. \tag{4.14}$$

The spanwise flow angle plot shows the quite typical secondary flow structure downstream of the cascade. From this plot, it is shown that the distortion and deflection produced by the passage vortex is relatively large in the region near the endwall. Effect of the secondary flows is significantly accumulated at z/H = 0.1.

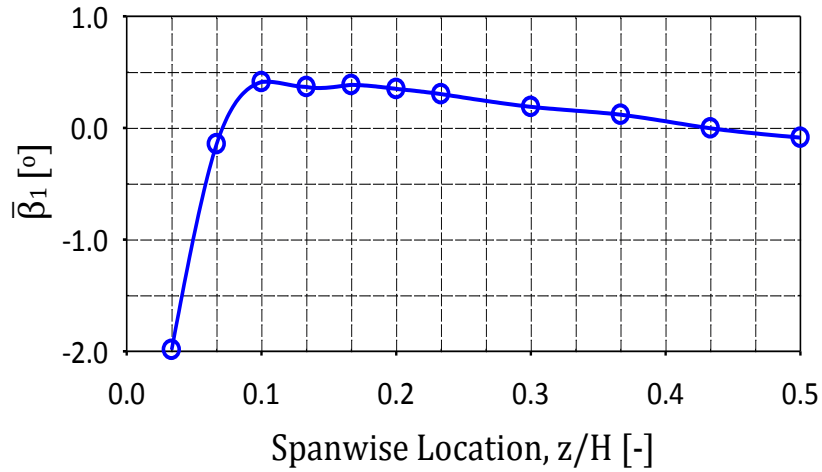

Figure 4.9 Averaged spanwise flow angle as function of span at fully opening cascade

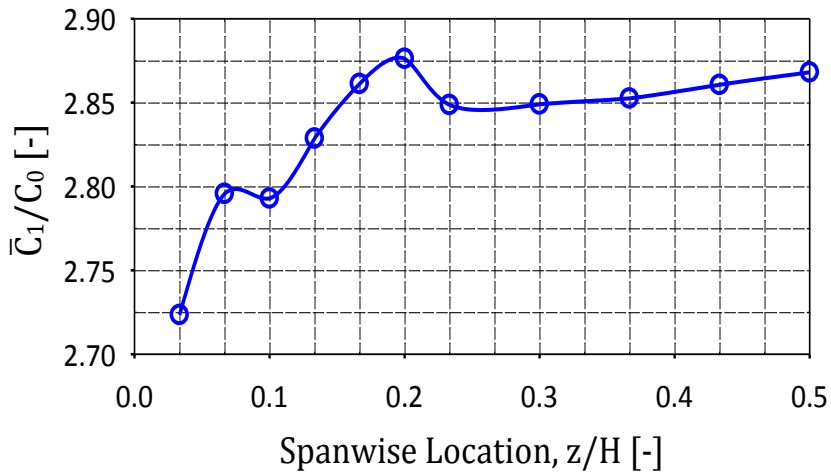

Figure 4.10 Averaged nondimensional velocity as a function span at fully opening cascade

Figure 4.10 depicts the distribution of pitchwise-averaged nondimensional velocity along span, measured downstream of the cascade. Again, the endwall is positioned at z/H = 0,0

Die approbierte gedruckte Originalversion dieser Dissertation ist an der TU Wien Bibliothek verfügbar.
The approved original version of this doctoral thesis is available in print at TU Wien Bibliothek.
TU Bibliothek Your knowledge hub WIEN

and z/H = 0.5 is midspan. The distribution of nondimensional velocity is expressed by the pitchwise-averaging nondimensional velocity as

$$\frac{\bar{C}_1}{C_0} = \frac{\int_0^t \left(\frac{C_1}{C_0}\right) C_1 \cos \beta_1 \sin \alpha_1 \, dy}{\int_0^t C_1 \cos \beta_1 \sin \alpha_1 \, dy}. \tag{4.15}$$

Based on the plot, nondimensional velocity greatly increases in region from the endwall up to peak value at z/H = 0.2. This region is mostly occupied by secondary flows and their interaction, especially passage vortex with counter-rotating vortex. From the peak location towards midspan, the effect of secondary flows significantly reduces.

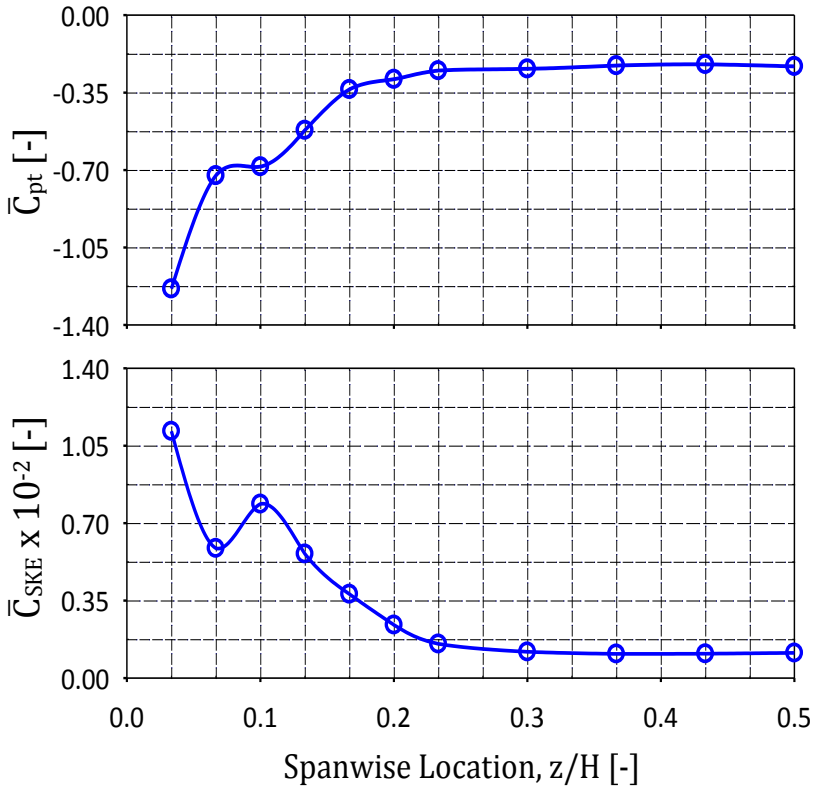

Figure 4.11 Averaged total pressure coefficient and secondary kinetic energy coefficient as a function span at fully opening cascade

Figure 4.11 is the distribution of pitchwise-averaged total pressure and secondary kinetic energy coefficient along span. Like before, the endwall is at z/H = 0.0 and z/H = 0.5 is midspan. The distribution of total pressure coefficient is determined through pitchwise-averaging the total pressure coefficient as

$$\bar{C}_{pt} = \frac{\int_0^t C_{pt} C_1 \cos \beta_1 \sin \alpha_1 \, dy}{\int_0^t C_1 \cos \beta_1 \sin \alpha_1 \, dy}. \tag{4.16}$$

From the top plot in the Fig. 4.11, it shows the variation of the averaged total pressure coefficient in spanwise direction. It is seen that the total pressure deficit is high at endwall

Die approbierte gedruckte Originalversion dieser Dissertation ist an der TU Wien Bibliothek verfügbar.
The approved original version of this doctoral thesis is available in print at TU Wien Bibliothek.
TU Bibliothek Your knowledge hub WIEN

region up to 20% span due to the endwall boundary layers and is associated with the vortex structures downstream of the cascade.

Another important distribution is the loss quantity expressed through a pitchwise-averaging secondary kinetic energy coefficient and defined as

$$\bar{C}_{SKE} = \frac{\int_0^t C_{SKE}\, C_1 \cos\, \beta_1 \sin\, \alpha_1\, dy}{\int_0^t C_1 \cos\, \beta_1 \sin\, \alpha_1\, dy}. \tag{4.17}$$

The averaged secondary kinetic energy coefficient is presented by the plot in the bottom of Fig. 4.11. The secondary kinetic energy coefficient is almost near zero in the region from z/H = 0.25 to 0.5, showing that the flow is void of secondary flow and flow field is a pure primary flow. The high secondary kinetic energy coefficient is seen near the endwall, a probably result from the direct impact of flow overturning in this region.

The overall mentioned plot results in this fully opening cascade measurement provide the basis of analysis for the variable closing degree position in both closing types of closing to pressure side (CPS) and closing to suction side (CSS) of the cascade. The primary quantity presented in the contours will be the same, but the overall description of the plots will change. The result details are given in Chapter 5.

Die approbierte gedruckte Originalversion dieser Dissertation ist an der TU Wien Bibliothek verfügbar.
The approved original version of this doctoral thesis is available in print at TU Wien Bibliothek.

5 Results of the partially closing for CPS and CSS

5.1 Two-dimensional flow field

Interesting parameters influenced the flow performance of throttling nozzle in the two-dimensional flow are discussed in this section. Characteristics of the wake downstream are studied by analyzing the pattern of pitchwise flow angle, normalized velocity distribution, static and total pressure coefficient, as well as turbulence intensity. Effects of three partial closing conditions on these parameters for two closing models of closing to pressure side (CPS) and closing to suction side (CSS) are presented.

5.1.1 Exit flow angle

The exit flow angle distributions of the cascade were made across one pitch location at three different closing positions of 10%, 20% and 30% for both closing types of CPS and CSS are presented in Fig. 5.1. The closing degree of the cascade increases from top to bottom. Based on this result, the plots show downstream flow angle variation, especially in the wake region. This variation is expected since the wake is filling through the diffusion process of blades boundary layer into the wake. It is seen that for both closing cases tested, the pitchwise flow angles at higher closing degrees are lower under the same pitch position than at lower closing degree. This is caused by the effect of flow separation forming over the blade passage due to the flow encounters an abrupt change in areas of the passage. This separation makes reduction of the momentum resulting in low deviation at the suction side of the blade passage. From this plot, it also shows that for both closing cases examined, the nonuniformity of the flow increases with increasing closing degree.

5.1.2 Nondimensional velocity

Figure 5.2a compares the nondimensional velocity profiles for two closing types of CPS and CSS at three partial closing positions. The upper curves of the figure are for a closing degree of 10% while the middle and bottom curves of the plot are for a closing degree of 20% and 30% respectively. The distribution provides a general concept of how the wake spreads and wake axis shift with the increasing closing degree. From this plot, the nondimensional velocity in the freestream and in the wake increase with increasing closing degree positions. At δ = 10%, the flow in both closing cases follows similar wake profile to that of fully opening condition but with a slightly higher velocity coefficient value. At higher closing degrees, δ = 20% and 30%, it shows a larger wake stretching and the wake axis shift to pressure side. Generally, broader wakes with increased the degree of closing possibly caused by the growth of different boundary layer and increased turbulent diffusion

Die approbierte gedruckte Originalversion dieser Dissertation ist an der TU Wien Bibliothek verfügbar.
The approved original version of this doctoral thesis is available in print at TU Wien Bibliothek.
TU Bibliothek Your knowledge hub WIEN

within the wake. The boundary layer changes resulting from increased the forward and backward facing step of flow passage generally include earlier separation, augmented mixing and turbulent transport, more rapid boundary layer streamwise development, and thicker boundary layers at blade trailing edge.

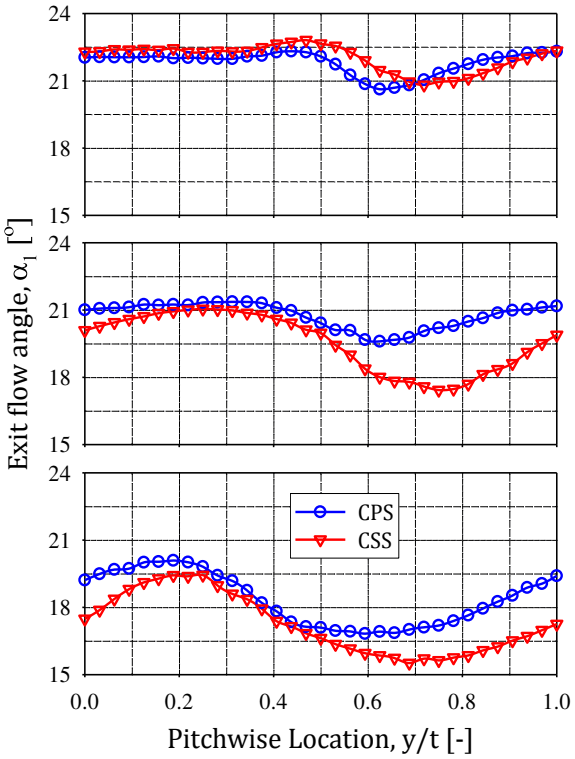

Figure 5.1 Exit flow angle distribution at the three different closing δ = 10%, 20%, and 30% for both CPS and CSS

5.1.3 Static pressure coefficient

Distributions of static pressure coefficient traverse downstream of the cascade for the two closing directions of CPS and CSS at three different closing conditions are given in Fig. 5.2b. As before, the closing degree of the cascade increases from top to bottom. Compared with the velocity defect and total pressure loss variation through the wake region, the static pressure variation was relatively small. From this plot, it can be seen for both closing cases investigated that the distribution of static pressure coefficients is quite uniform across the whole pitch location. For CSS case, the static pressure coefficient decreases quickly with increasing closing degree from -8.6 at δ = 10% down to -15.0 at δ = 30%. For the CPS case, its values also decrease, although not as drastically as for the CSS case. The general conclusion that can be drawn based on the plots is that an increase in the closing degree of the cascade results in a decrease of static pressure coefficient while a decrease in the closing degree results in an increase of static pressure coefficient as can be seen in the middle and the bottom plots of the presented figures.

Die approbierte gedruckte Originalversion dieser Dissertation ist an der TU Wien Bibliothek verfügbar.
The approved original version of this doctoral thesis is available in print at TU Wien Bibliothek.
TU Bibliothek Your knowledge hub WIEN

5.1.4 Total pressure coefficient

The total pressure coefficient distributions for both closing directions of CPS and CSS at three partial closing conditions are examined in Fig. 5.3a. As before, the upper curves of the figure are for a closing degree of 10% while the middle and bottom curves of the plot are for a closing degree of 20% and 30% respectively. These plots illustrate how the total pressure deficits increase as the extended closing degree. The results at δ = 10% show that the wakes of the two closing types compared appear quite similar to one another with the wake at the case of CSS being slightly wider and having a larger maximum pressure deficit than that of CPS case. Pressure side of the wake is mostly coincident for bot closing cases tested. This result shows that the variation of the pressure deficit generated by both closing directions is dominated by changes to the suction surface boundary layer.

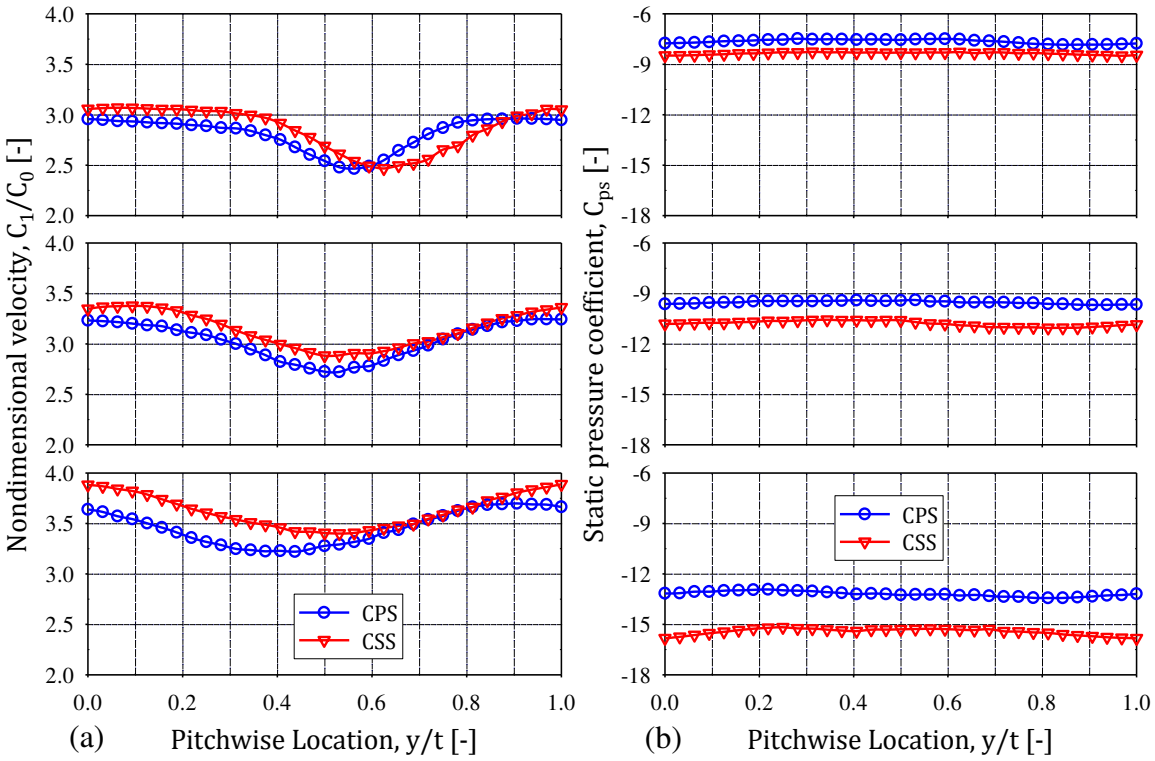

Figure 5.2 (a) Nondimensional velocity; (b) Static pressure coefficient at the three different closing δ = 10%, 20%, and 30% for both CPS and CSS

At higher closing degrees, δ = 20% and 30%, an increase in the degree of closing results in an increase of total pressure deficit and a tangential broadening of the wake. The increase of pressure deficit is mainly due to a more entropy production within the blade boundary layers. It is understood that the early separation has a major impact on the low momentum of blade boundary layers within the wake. The stretching of the wake in both pressure and suction side is in accord with the exit flow angle distribution presented previously which shows an increased flow nonuniformity at higher closing degrees. From these plots, it is seen that the wakes in the CSS are deeper than those in the CPS.

Die approbierte gedruckte Originalversion dieser Dissertation ist an der TU Wien Bibliothek verfügbar.
The approved original version of this doctoral thesis is available in print at TU Wien Bibliothek.
TU Bibliothek Your knowledge hub WIEN

5.1.5 Turbulence intensity

Distribution of turbulence intensity measurements at three partial closing degrees for both closing types of CPS and CSS are shown in Fig. 5.3b. Again, the upper curves of the figure are for a closing degree of 10% while the middle and bottom curves of the plot are for a closing degree of 20% and 30% respectively. Generally, the plots of turbulence intensity show the wake asymmetry most clearly about the trailing edge axis at y/t = 0.5 and turbulence intensity peaks are distinctly different with the more significant differences are seen between both CPS and CSS cases in the suction side. The asymmetric profile reflects the different sizes of boundary layers exiting from the passage. Turbulence intensities were considerably higher in the wake containing suction side boundary layer.

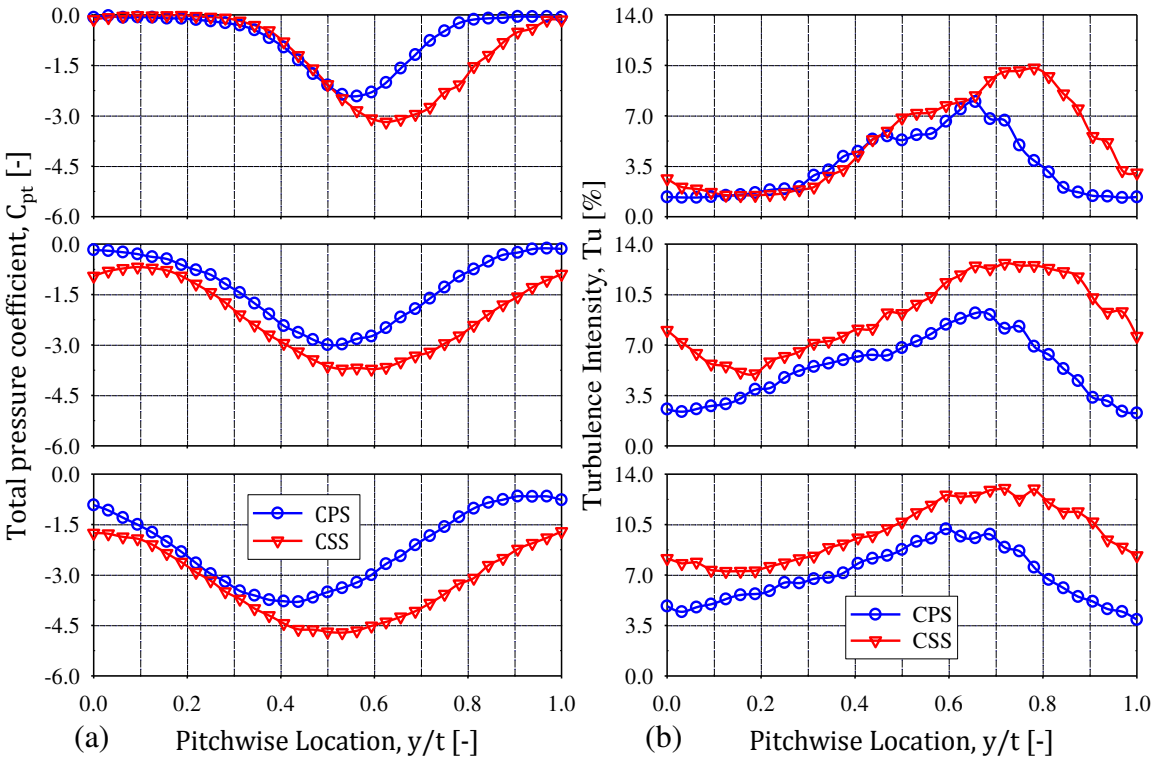

Figure 5.3 (a) Total pressure coefficient; (b) Turbulence intensity at the three different closing conditions, δ = 10%, 20%, and 30% for both CPS and CSS

At δ = 10%, it is found that the highest turbulence intensity in the case of CPS is about 7.5 percent and in the case of CSS is about 10.5 percent. This maximum value of intensity occurs on the suction side of the wake at about y/t = 0.65 for the case of CPS and y/t = 0.75 for the CSS case. It is also seen that the turbulence intensity decreases as the undistributed freestream is approached. The distinct trends are shown at higher closing degrees, δ = 20% and 30% as shown in the middle and bottom plots. The trends display that the turbulence intensity in CPS case is much lower than in CSS one along entire pitch location. Moreover, the wakes are significant wider at both closing cases investigated.

Die approbierte gedruckte Originalversion dieser Dissertation ist an der TU Wien Bibliothek verfügbar.
The approved original version of this doctoral thesis is available in print at TU Wien Bibliothek.
TU Bibliothek Your knowledge hub WIEN

5.1.6 Pitchwise-averaged distribution

The results of pitchwise-averaged measurements as a function of closing degree position are plotted in Figs. 5.4, 5.5 and 5.6. The differences in averaged flow angle at two closing types of CPS and CSS are illustrated in Fig. 5.4a. This plot shows that the averaged flow angles are declining at different slope for $\delta > 12.5\%$ with declining slope of the CPS is smaller than that of CSS. In addition, this plot also shows that the averaged value of flow angle decreases as the degree of closing enlarges for the CPS, while for the CSS, the profile gradually increases at the low degree of closing $\delta < 7.5\%$, and then decreases more rapidly in a mostly linear with increase the degree of closing.

The trends of averaged nondimensional velocity for both closing types of CPS and CSS are presented in Fig. 5.4b. From this figure, it is seen that averaged nondimensional velocities at the CPS have the same tendency as those measured at the CSS. Also shown that there is initially a small drop in the nondimensional velocity at low closing degree but then it starts to increase more rapidly with increasing the degree of closing for both closing directions tested. This increasing in the CPS is relatively lower than in the CSS case.

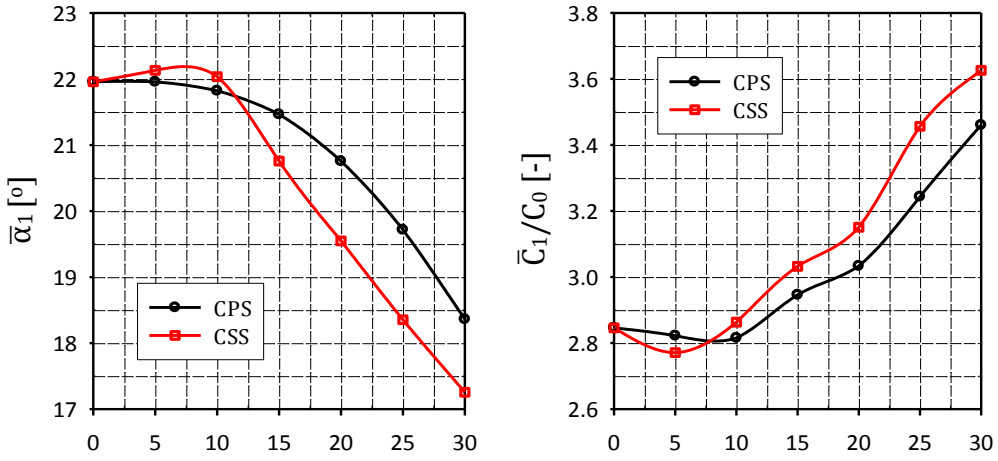

Figure 5.4 Exit flow angle and velocity as a function of δ for both CPS and CSS

Figure 5.5a describes the averaged static pressure coefficient at both closing types of CPS and CSS. In general, averaged static pressure coefficient decreases as the increase closing degree for both closing cases. with the decreasing trend of the CSS is higher than that of CPS. It also can be noticed that the static pressure coefficient reduces dramatically at the large closing degree, $\delta > 17.5\%$.

The discrepancies in averaged total pressure coefficient between both closing cases of CPS and CSS are displayed in Fig. 5.5b. Based on this plot, it seems that the averaged total pressure coefficient decrease monotonically as the closing enlarges for both closing cases

Die approbierte gedruckte Originalversion dieser Dissertation ist an der TU Wien Bibliothek verfügbar.
The approved original version of this doctoral thesis is available in print at TU Wien Bibliothek.
TU Bibliothek Your knowledge hub WIEN

evaluated. However, at low closing degree δ < 5%, the profiles are almost coincident, and then followed decreases more rapidly in a mostly linear way with increasing degree of closing. This decrease in the case of CSS is much sharper than in the CPS case. This could be possibly caused by the effect of the development and growth of blade boundary layers, as well as the influence of the abrupt change of the flow passage.

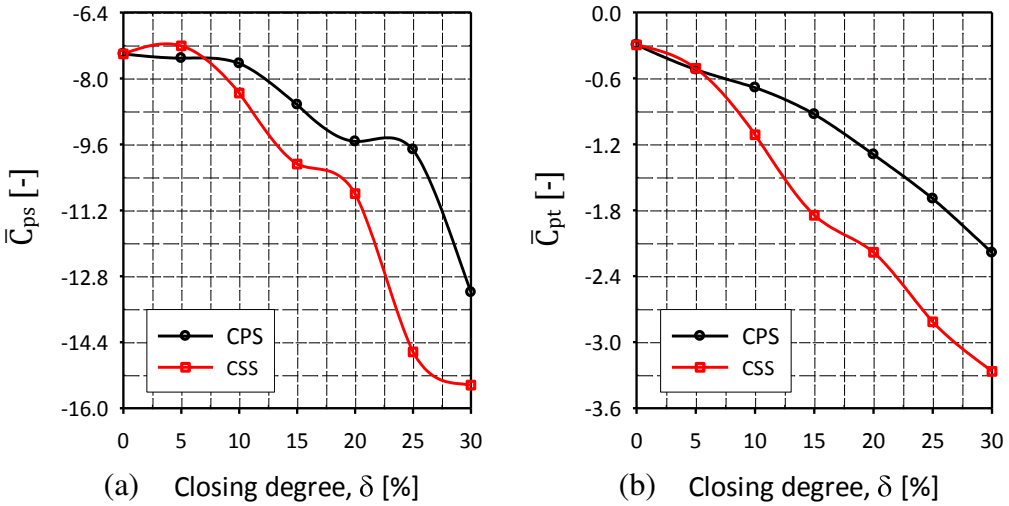

Figure 5.5 Static and total pressure coefficient as a function of δ for both CPS and CSS

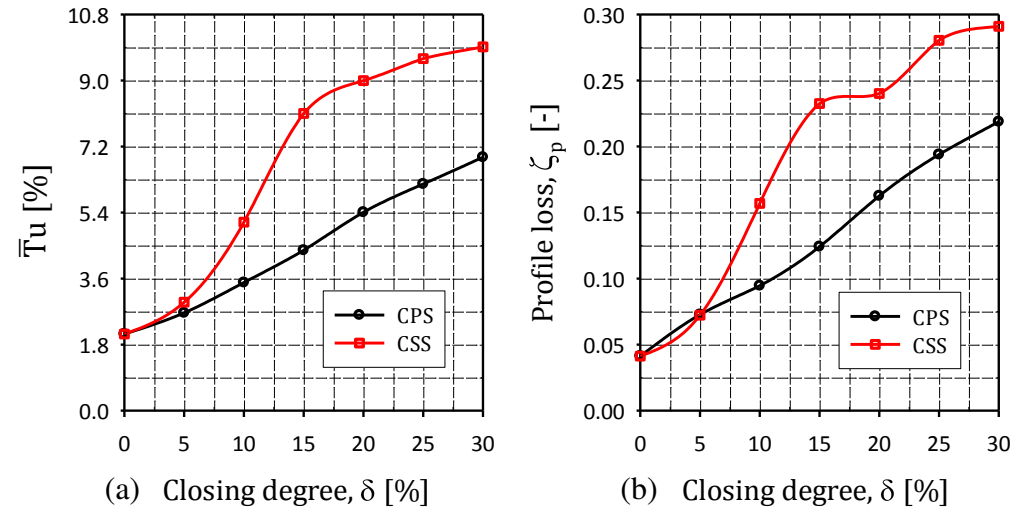

Figure 5.6 Turbulence intensity and profile loss as a function of δ for both CPS and CSS

Figure 5.6a depicts the variations of averaged turbulence intensity at both closing cases of CPS and CSS. The curve describes the fluctuating of streamwise velocity caused by the interaction of blade boundary layer and the wake. From this figure, it could be seen that the intensity steadily increases as the increasing degree of closing at the CPS. While, at the CSS, the trend of intensity shows a considerably increase at δ < 15% and then again gradually increase in a mostly linear way with enlarge closing degree.

Die approbierte gedruckte Originalversion dieser Dissertation ist an der TU Wien Bibliothek verfügbar.
The approved original version of this doctoral thesis is available in print at TU Wien Bibliothek.
TU Bibliothek Your knowledge hub WIEN

The loss for this study was determined based on three-hole probe measurement in midspan downstream of the cascade. This loss is expressed as the coefficient and calculated as

$$\zeta_P = -\bar{C}_{pt}\left(\frac{\sin\bar{\alpha}_1}{\sin\alpha_0}\right)^2 \tag{5.1}$$

where ζ_P is the pressure loss coefficient, $\bar{C}_{pt}$ is the averaged total pressure coefficient, α_0 and $\bar{\alpha}_1$ are inlet and outlet flow angles. The distribution of the averaged loss coefficient is presented in Fig. 5.6b. The curves in this plot obviously show that the loss increases as the closing degree enlarges in both cases. In the case of CPS, the loss increases monotonically, while in the case of CSS, the sharp growth of the loss at $\delta < 15\%$ and then again it grows moderately at $\delta > 20\%$. Based on this result, the CPS has a better performance than CSS, therefore the CPS is preferred to regulate steam flow rate in the extraction turbines.

5.2 Three-dimensional flow field

This section is intended to give an analysis of the results for three-dimensional flow field downstream of the throttling nozzle. Effects of the partial closing on the secondary flow structures at two closing types of closing to pressure side (CPS) and to suction side (CSS) at three different closing degrees of $\delta = 5\%$, 15% and 30%, are presented. The view is of the measurement plane looking upstream with the passage pressure side on the left, and the passage suction side on the right. The plots have the same scale and are placed side by side for direct comparison in terms of physical structures.

5.2.1 Pitchwise flow angle

Effects of partial closing degree on the pitchwise flow angle downstream of the cascade for both closing types of CPS and CSS are presented in Fig. 5.8a and 5.8b. The closing degree of the cascade increases from top to bottom. The isoclines from low to large closing degree show, in general, large variations in flow angle, especially very near the endwall. Contours with values higher than reference exit flow angle of 20^o indicate regions where the flow was overturned. Examining isoclines at $\delta = 5\%$, overturning predominates near the endwall at about $z/H < 0.15$ as driven by the passage vortex in both cases. The vortex induces flow underturning in the area above 15% span. This result is almost similar with fully opened cascade as shown in Fig. 4.3a. The cores of vortex are centred at about $y/t = 0.6$ and $z/H = 0.1$ for both closing types examined. At higher closing degrees, $\delta = 15\%$ and $\delta = 30\%$, the vortex cores tend to move to the pressure side and shift down toward the endwall for both closing types. It can be noted that the closing type has a relatively small effect on the level of underturning causing a slight increase from $z/H = 0.15$ to midspan. Below $z/H = 0.15$, the gradient of the flow angle decreases for both closing types evaluated.

Die approbierte gedruckte Originalversion dieser Dissertation ist an der TU Wien Bibliothek verfügbar.
The approved original version of this doctoral thesis is available in print at TU Wien Bibliothek.
TU Bibliothek Your knowledge hub WIEN

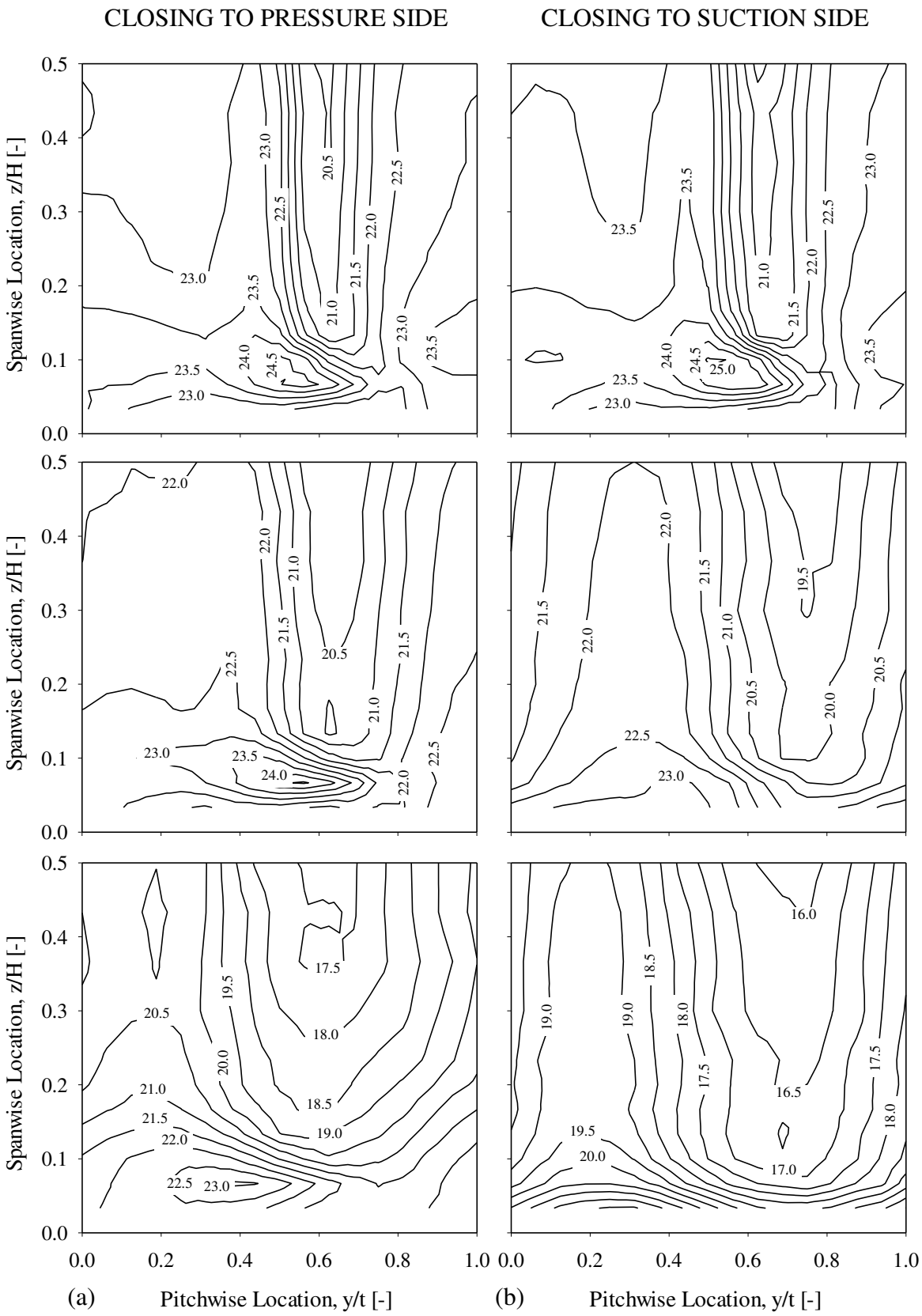

Figure 5.8 Pitchwise flow angle contours at three different partial closing positions, δ = 5%, 15%, and 30% (a) by CPS and (b) by CSS

Die approbierte gedruckte Originalversion dieser Dissertation ist an der TU Wien Bibliothek verfügbar.
The approved original version of this doctoral thesis is available in print at TU Wien Bibliothek.
TU Bibliothek Your knowledge hub WIEN

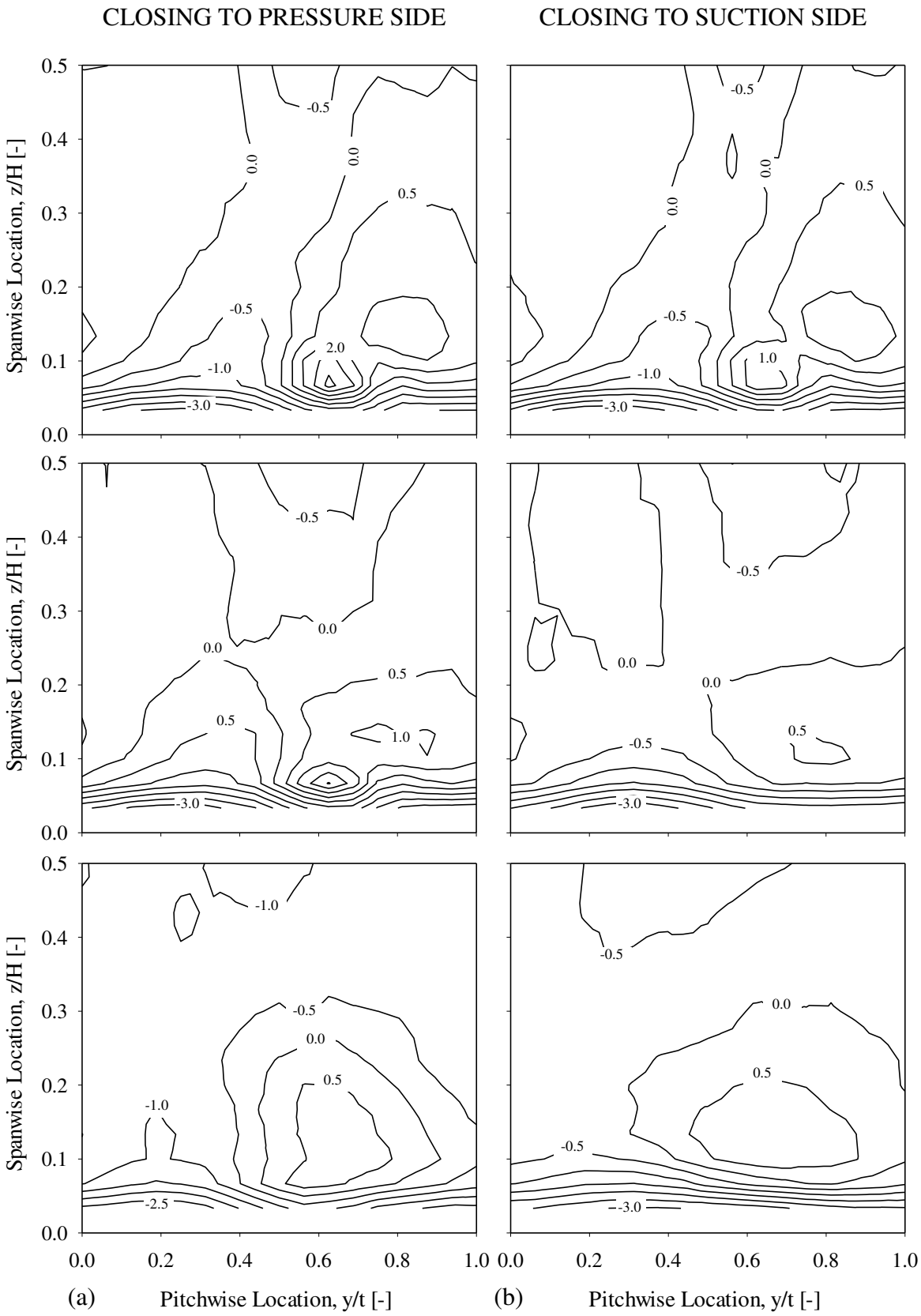

Figure 5.9 Spanwise flow angle contours at three partial closing positions, δ = 5%, 15%, and 30% (a) by CPS and (b) by CSS

Die approbierte gedruckte Originalversion dieser Dissertation ist an der TU Wien Bibliothek verfügbar.
The approved original version of this doctoral thesis is available in print at TU Wien Bibliothek.
TU Bibliothek Your knowledge hub WIEN

5.2.2 Spanwise flow angle

Measurements of spanwise flow angle distribution for two types of CPS and CSS at three different closing degrees are plotted in Fig 5.9a and 5.9b. The upper plots are for a closing degree of 5% while middle and bottom plots are for a closing degree of 15% and 30% respectively. Again, isoclines contours show very large variation of the flow structure downstream of the cascade and show strong endwall boundary layer effects at x/b = 0.3 plane. The measurements of spanwise flow angle at this location show some evidence of spanwise asymmetry. Moreover, isoclines are almost similar structure at the same degree of closing for both cases examined. The local values of flow angle near midspan are found as high as -0.5^o to -1^o. Probably, this is an error may be caused by the probe interfering with the vortex structures. In general, the locations of vortex core are clearer for these pitchwise angle contours than they are for spanwise angle contours for both cases. At δ = 5%, cores were found at the point where the local magnitude of flow angle is zero, which is between the maximum value of +2.0^o for CPS case and +1.0^o for CSS case and the minimum value of -3.0°, near the same spanwise and pitchwise location found in the pitchwise flow angle contours. At larger closing degrees, δ = 15% and δ = 30%, the flow starts to straighten, however, the locations of the vortex core remain evident. The locations of core are seen to shift down toward the endwall as can be seen in the middle and bottom plots, plausibly consistent with isoclines of pitchwise flow angle.

5.2.3 Nondimensional velocity

Figure 5.10a and 5.10b show contours of nondimensional velocity at three different partial closing conditions for CPS and CSS, respectively. Again, the upper plots are for a closing degree of 5% while the middle and bottom plots are for a closing degree of 15% and 30% respectively. Evaluating the plots at δ = 5%, the contours are almost similar to the fully opening case, reveal the wakes which are the vertically oriented regions of mean velocity defect in the region from 15% of the span up to midspan. Outside this region, the passage vortex from blade #3 can be seen to dominates the endwall region, revealed as the region of high velocity defect, and occupying the area the wake of blade #4. The core of vortex is concentred at y/t = 0.60 and z/H = 0.10 with a minimum value of nondimensional velocity approximately 2.45 for both closing types tested. As the degree of closing was increased, as presented in the middle plot, there appeared the vortex structures spread in the wake with minimum nondimensional velocity value are about 2.60 at CPS and 2.65 at CSS. At highest closing degree, these structures begin to merge entirely in the wake with peaks increased and reached about 3.10 at CPS and 3.45 at CSS very near the endwall as shown in the bottom plot. This is due to the boundary layer experiences early separation and form a mixing boundary layer of the blades. To sum up, it can be noted that an increase in the closing degree results in an increase of nondimensional velocity for both closing cases as can be seen in the middle and bottom plots.

Die approbierte gedruckte Originalversion dieser Dissertation ist an der TU Wien Bibliothek verfügbar.
The approved original version of this doctoral thesis is available in print at TU Wien Bibliothek.
TU Bibliothek Your knowledge hub WIEN

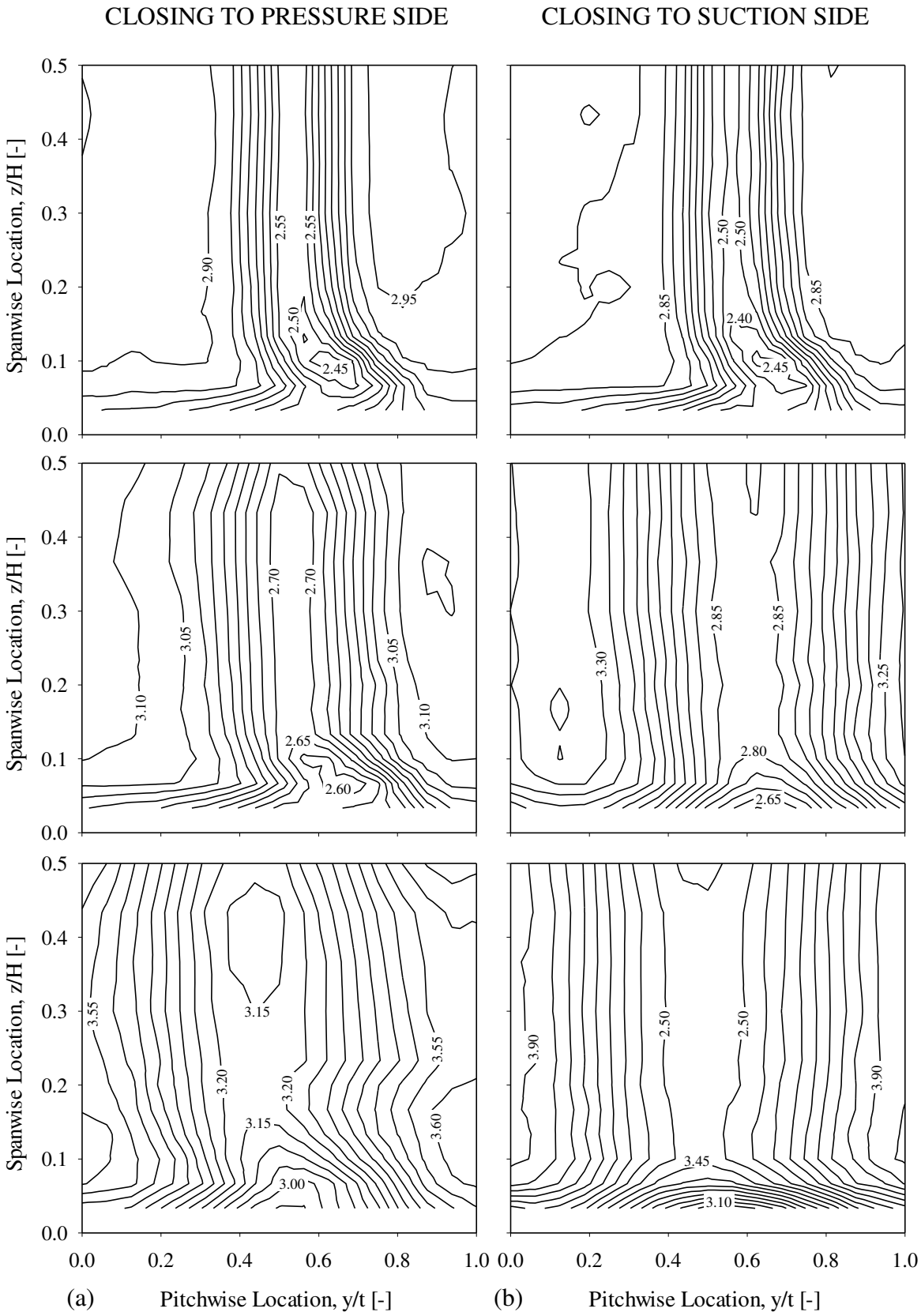

Figure 5.10 Nondimensional velocity contours at three different closing positions δ = 5%, 15%, and 30% (a) by CPS and (b) by CSS

Die approbierte gedruckte Originalversion dieser Dissertation ist an der TU Wien Bibliothek verfügbar.
The approved original version of this doctoral thesis is available in print at TU Wien Bibliothek.
TU Bibliothek Your knowledge hub WIEN

5.2.4 Secondary kinetic energy coefficient

Contour plots of the secondary kinetic energy coefficient at three partial closing conditions of δ = 5%, 15% and 30% for both CPS and CSS are shown in Fig 5.11a and 5.11b. As before, the upper plots are for a closing degree of 10% while the middle and bottom plot are for a closing degree of 15% and 30% respectively. The contour plots show a trend of secondary kinetic energy coefficient near the endwall increase with the increase closing degree. A reason for this is the change of endwall boundary layer which is affected by the abrupt change in the area of the flow passage. In the case of δ = 5%, the contour plots of CPS and CSS reveal a high secondary kinetic energy coefficient induced by the action of passage vortex near the endwall below 10% span, resulting in flow overturning. The magnitudes of secondary kinetic energy coefficients produced by passage vortex are $1.0\text{x}10^{-2}$ at CPS case and $1.25\text{x}10^{-2}$ at CSS case. Closer to the endwall, these magnitudes significantly increase, a possibly results of penetration of a horseshoe vortex and a direct consequence of increased overturning in this region. At higher closing the coefficient of secondary kinetic energy increased. These magnitudes increase by $2.75\text{x}10^{-2}$ at δ = 15% and by $5.25\text{x}10^{-2}$ at δ = 30% for CPS, while for the case of CSS the increase of these coefficients can reach $4.50\text{x}10^{-2}$ at δ = 15% and $10.50\text{x}10^{-2}$ at δ = 30%. In the case of CSS, the strength of secondary kinetic energy near the endwall is accentuated and roughly twice as strong for the case of closing to pressure side.

5.2.5 Nondimensional vorticity

Figures 5.12a and 5.12b are the contour plots of normalized vorticity at three different partial closing degrees for both CPS and CSS, respectively. The upper plots are for a closing degree of 5% while the middle and bottom plots are for a closing degree of 15% and 30% respectively as before. Observing the contour plots at δ = 5%, the secondary flow region is very well defined. The secondary flow structures are occupied by passage vortex, counter-rotating vortex, and suction side leg of the horseshoe vortex in both closing cases investigated. The passage vortex with intensity of -2.80 is concentred at about y/t = 0.75 and approximately z/H = 0.1. A counter-rotating vorticity of about +2.10 for CPS case and +1.40 at CSS case are centered at around y/t = 0.55 and about z/H = 0.1. The suction side leg of horseshoe vortex with the same direction and intensity of passage vortex is found close to the endwall at about z/H < 0.15. As the closing degree increased there appeared to be an appreciable change in the intensity and the structures of vortices. At δ = 15%, this change is marked by the decreasing intensity of horseshoe vortex and counter-rotating vortex while the strength of passage vortex is relatively unchanged. At highest closing degree, δ = 30%, very close to the endwall both passage vortex and suction side leg of the horseshoe vortex are not recognized. Probably, both these vortices merged into a single negative vortex with intensity -1.40. Moreover, it is also seen that intensities of counter-rotating vortex increased for this condition at both closing cases tested.

Die approbierte gedruckte Originalversion dieser Dissertation ist an der TU Wien Bibliothek verfügbar.
The approved original version of this doctoral thesis is available in print at TU Wien Bibliothek.
TU Bibliothek Your knowledge hub WIEN

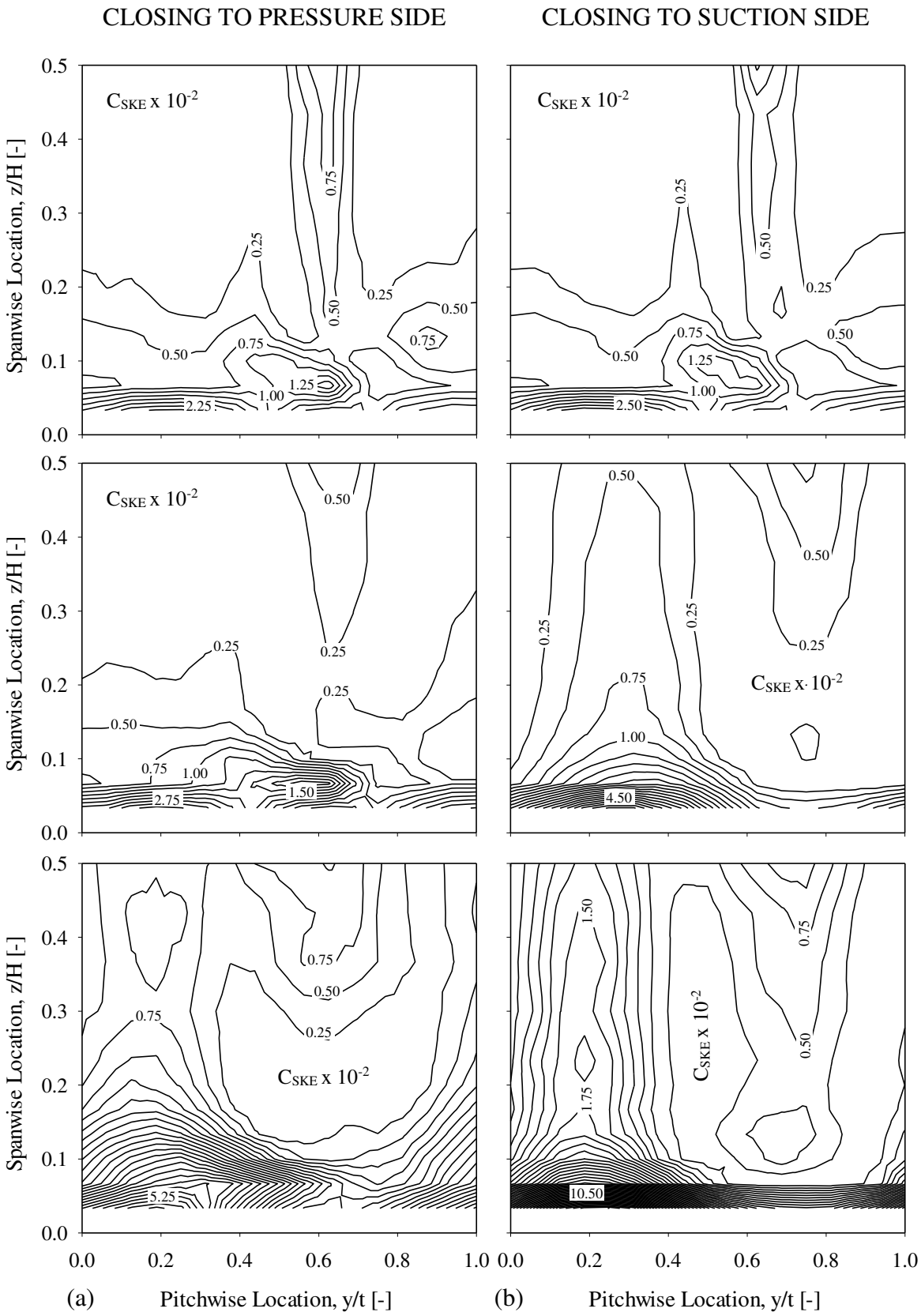

Figure 5.11 Secondary kinetic energy coefficient contours at three partial closing positions, δ = 5%, 15%, and 30% (a) by CPS and (b) by CSS

Die approbierte gedruckte Originalversion dieser Dissertation ist an der TU Wien Bibliothek verfügbar.
The approved original version of this doctoral thesis is available in print at TU Wien Bibliothek.

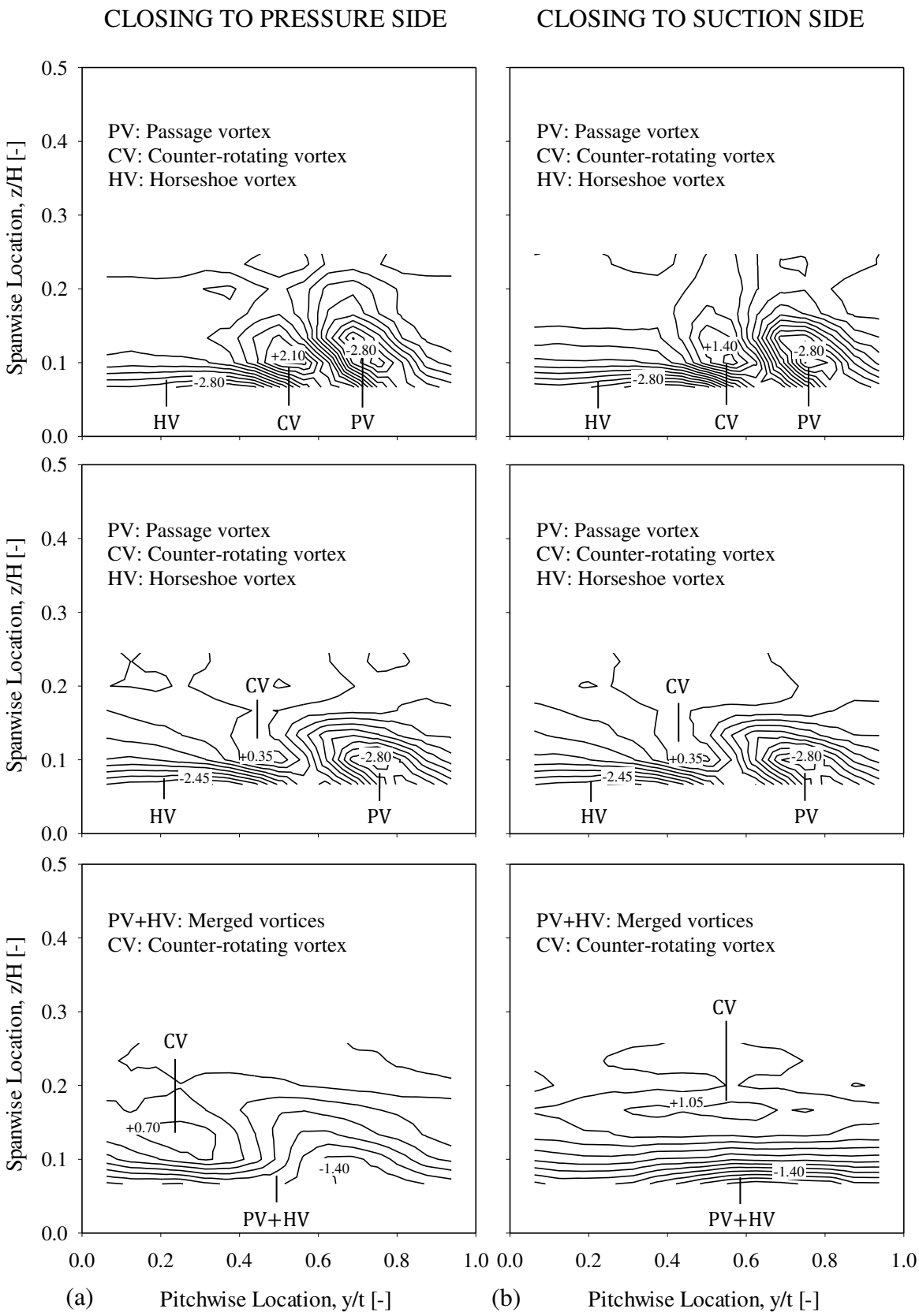

Figure 5.12 Nondimensional streamwise vorticity contours at three partial closing positions δ = 5%, 15%, and 30% (a) by CPS and (b) by CSS

Die approbierte gedruckte Originalversion dieser Dissertation ist an der TU Wien Bibliothek verfügbar.
The approved original version of this doctoral thesis is available in print at TU Wien Bibliothek.
TU Bibliothek Your knowledge hub WIEN

5.2.6 Total pressure coefficient

Contour plots of total pressure coefficient for both CPS and CSS at three partial closing degrees are depicted in Fig. 5.13a and 5.13b respectively. Again, the upper plots are for a closing degree of 5% while the middle and bottom plots are for a closing degree of 15% and 30% respectively. From this plot, the positions of the passage vortices can be found based on the regions of reduced total pressure. Looking at the contour plots for $\delta = 5\%$, the flow field has a relatively uniform structure dominated the two-dimensional flow extends from midspan up to about z/H = 0.15 for both closing conditions tested. The highly flow two-dimensionality in this zone is also presented by the almost ignorable values shown by contour plots of secondary kinetic energy coefficient in Fig. 5.11. Moving toward the endwall region, the contours show high total pressure deficit cores centred at about z/H = 0.1 in the spanwise location for both cases, while in the pitchwise location, it is around y/t = 0.6 for the CPS and approximately y/t = 0.7 for the CSS.

To examine the effects of increasing closing degree on secondary flows, results associated with the case of $\delta = 15\%$ are illustrated in middle plot of Fig. 5.13a and 5.13b. A much wider wake characterizes this higher closing degree for both closing cases examined. Thus, higher total pressure deficit is produced in this case. The flow two-dimensionality extends from midspan up to z/H = 0.10. Maximum values of total pressure deficit come out to be significantly increased at this condition, suggesting the occurrence of stronger secondary flows induced by increasing of closing degree. The highest deficit values in total pressure coefficient occurs near the endwall are about -2.45 at CPS and -2.50 at CSS, which are the passage vortex cores, showing a high loss region. At highest closing degree, $\delta = 30\%$, the changes in magnitudes and core locations of the peak total pressure coefficient are seen to occur as can be seen in the bottom plots of figure. From this plot, the expansion appears to be entirely a redistribution of the cores of total pressure coefficient spreading outwards the pressure and suction side of the passage. The deficits of total pressure coefficient increase by -5.0 and -7.65 for both CPS and CSS.

Comparing the CPS to the CSS at the three closing positions in Figs. 5.13, it is important to note that there are slightly changes in flow structures, and redistribution of total pressure deficit in the endwall region. Both closing directions alter the secondary flow structures, with the total pressure deficit areas expanding significantly as an increasing the degree of closing. It is worth noting that when comparing the pressure deficit regions at both closing cases, this expansion occurs to be massively redistribution of pressure deficit cores spilling out toward the pressure side and the suction side as can be seen in the middle and bottom plots of Fig. 5.13a and 5.13b. Moreover, the deficit cores of the CPS and CSS appear in the different location. The CSS has higher deficit at the cores than the CPS with higher closing conditions. Near midspan the CPS has lower deficit in the wake than the CSS. In short, it can be noted that the pressure loss in the CSS case is higher than in the case of CPS, especially at higher closing degree position.

Die approbierte gedruckte Originalversion dieser Dissertation ist an der TU Wien Bibliothek verfügbar.
The approved original version of this doctoral thesis is available in print at TU Wien Bibliothek.
TU Bibliothek Your knowledge hub WIEN

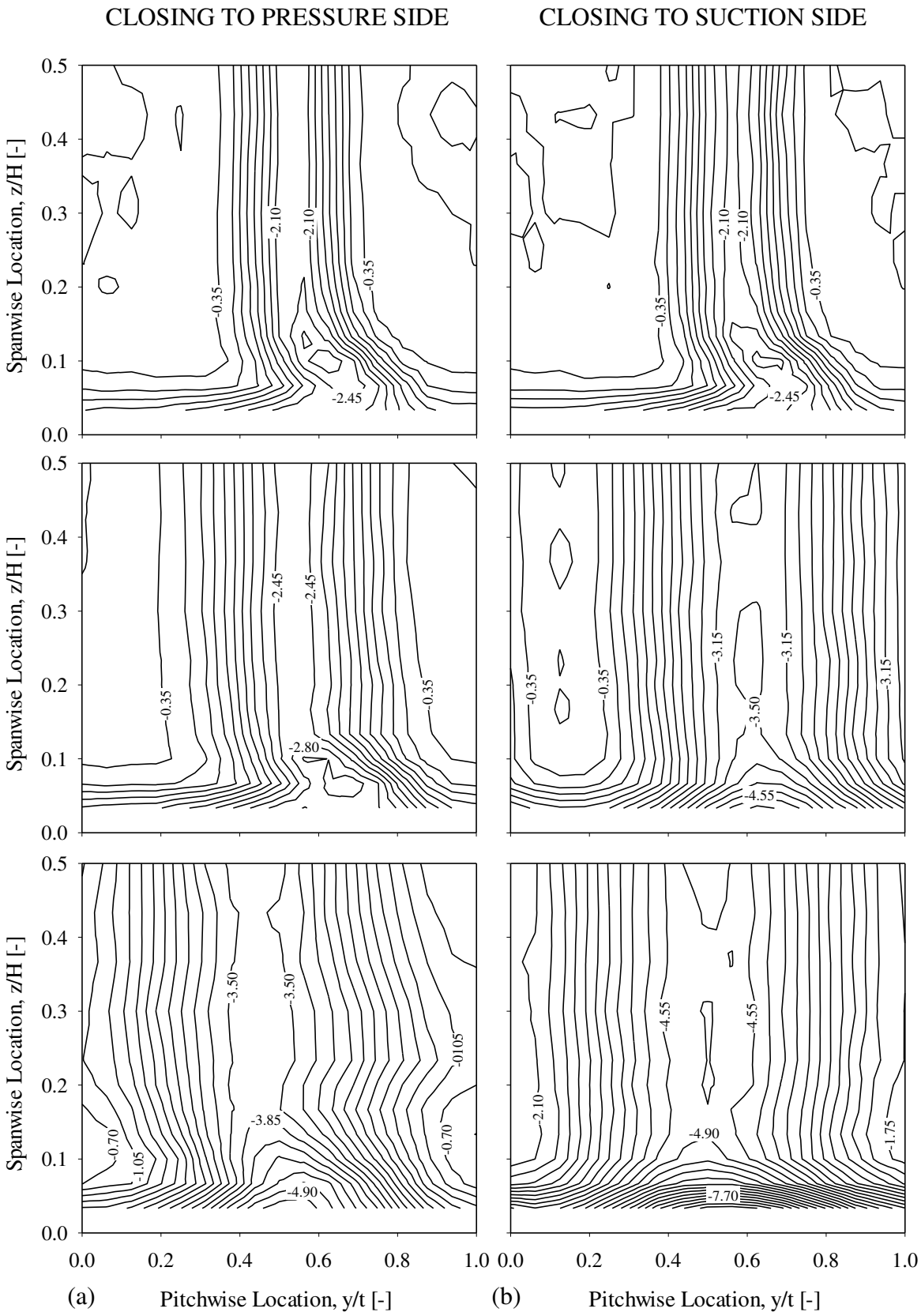

Figure 5.13 Total pressure coefficient contours at three different partial closing positions δ = 5%, 15%, and 30% (a) by CPS and (b) by CSS

Die approbierte gedruckte Originalversion dieser Dissertation ist an der TU Wien Bibliothek verfügbar.
The approved original version of this doctoral thesis is available in print at TU Wien Bibliothek.
TU Bibliothek Your knowledge hub WIEN

5.2.7 Pitchwise-averaged distribution

In order to examine and compare the effects secondary flows for different situations tested, all flow parameters measured in both closing types of closing to pressure side (CPS) and closing to suction side (CSS) have been pitchwise-averaged. All data originate from five-hole probe at measurement plane 30% axial chord downstream of the cascade. These average distributions as a function of the span at three partial closing degrees, δ = 5%, 15%, and 30% were combined, for each closing degree, here they are plotted as the upper, the middle and the bottom plot, respectively.

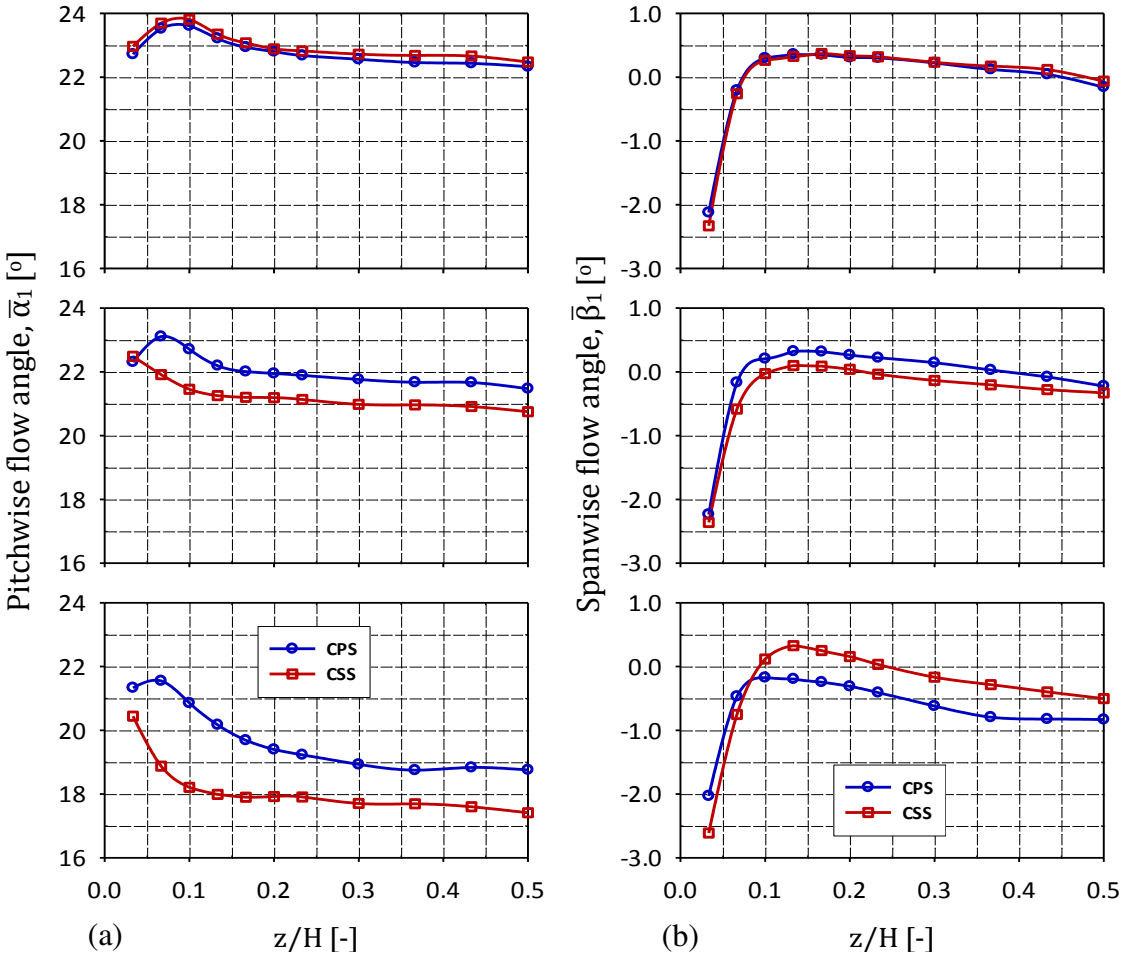

Figure 5.14 (a) Averaged pitchwise flow angle; (b) Averaged spanwise flow angle for three partial closing degrees, δ = 5%, 15%, and 30%

Figure 5.14a is a pitchwise-averaged distribution of pitchwise flow angles. The variations of the flow angles in the range of z/H = 0.2 to the endwall is the result of the formation of the vortices. As mentioned in discussion of Fig 5.8, the vortices rise towards the endwall and show complex structure but always overturned flow. At δ = 5%, the curves have a high overturning near the endwall, and this continuously reduces until it reaches underturning towards midspan. The averaged flow angles distribution for both closing cases is almost

Die approbierte gedruckte Originalversion dieser Dissertation ist an der TU Wien Bibliothek verfügbar.
The approved original version of this doctoral thesis is available in print at TU Wien Bibliothek.
TU Bibliothek Your knowledge hub WIEN

coincident along span with a peak underturning occurs at z/H = 0.10, pointing out that the highest loss occurs in the region where the passage vortex and the counter-rotating vortex interact. The flow angles at midspan for both CPS and CSS are about 22.3° and 22.5°. At higher closing degrees, the flow angles in the CPS case are higher along span as compared with the CSS one. Moreover, the quantitative variation of underturning slightly increased for both closing cases. The flow angles at midspan is decreased with average angle values are about 21.5° for CPS and around 20.8° for CSS at δ = 15% and its value is about 17.4° for CPS and around 18.8° for CSS at δ = 30%.

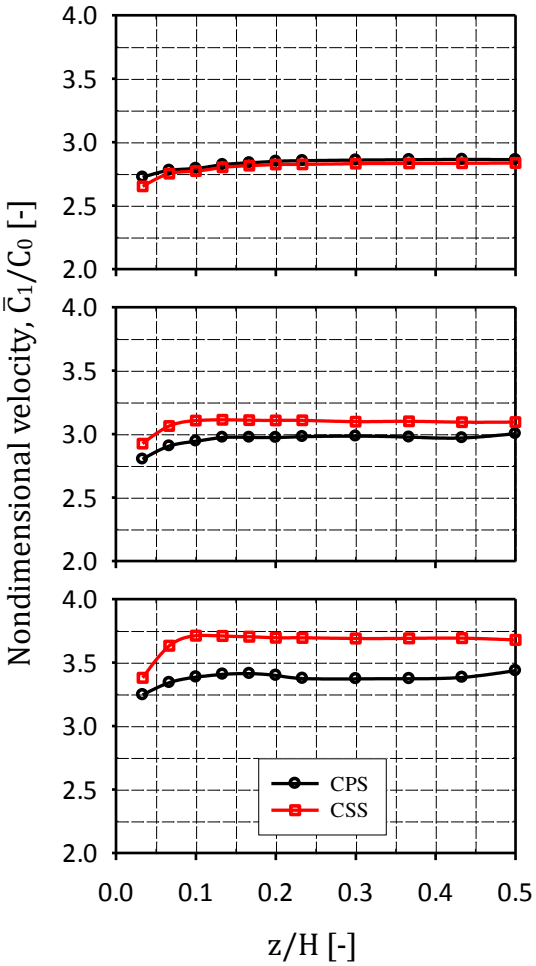

Figure 5.15 Averaged nondimensional velocity for three partial closing degrees, δ = 5%, 15%, and 30%

Figure 5.14b presents the pitchwise-averaged spanwise flow angles. Despite large local values of the spanwise flow angle as shown in Fig. 5.9, this plot shows that spanwise flow angle is within approximately -3° to +1°, even at the higher closing degree where the local value of flow angle is very large. There are not considerably changes in the typical of flow angles distribution with increasing the degree of closing, indicating that the flow field in spanwise direction is almost not influenced by the degree of closing, but slightly dependent on the directions of closing, especially for higher closing degree.

Die approbierte gedruckte Originalversion dieser Dissertation ist an der TU Wien Bibliothek verfügbar.
The approved original version of this doctoral thesis is available in print at TU Wien Bibliothek.
TU Bibliothek Your knowledge hub WIEN

Measurements of pitchwise-averaged nondimensional velocity are given in Fig. 5.15. The distributions show a large gradient below 15% span, showing the presence of secondary flow in this region. At δ = 5%, the distribution of nondimensional velocity coefficient is almost coincident along spanwise location at both closing cases. At higher closing degrees, δ = 15% and 30%, the nondimensional velocity showing much lower at closing to pressure side than at closing to suction side along span from the endwall up to midspan as can be seen in the middle and the bottom plots.

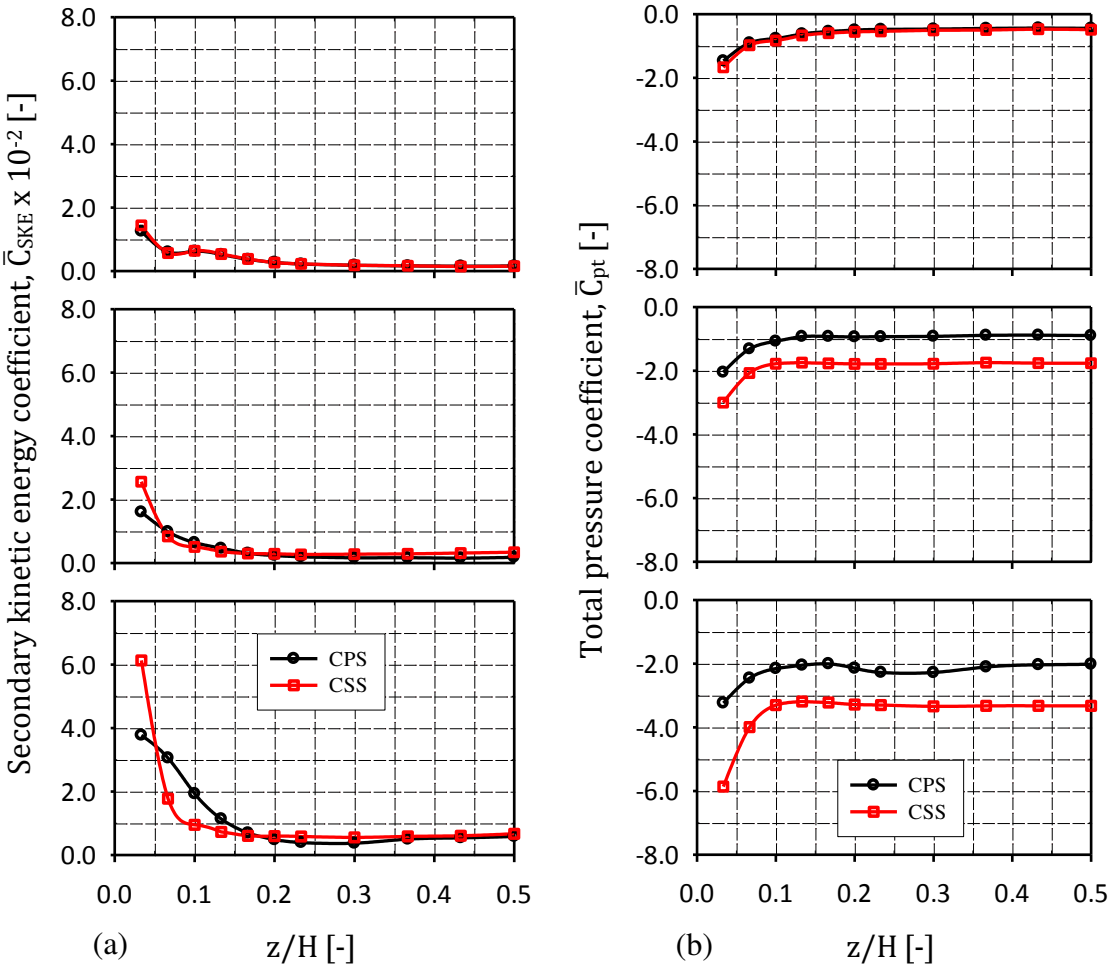

Figure 5.16 (a) Averaged secondary kinetic energy coefficient; (b) Averaged total pressure coefficient for three partial closing degrees, δ = 5%, 15%, and 30%

Profiles of pitchwise-averaged secondary kinetic energy coefficient are presented in Fig. 5.16a. In the region at about z/H = 0.15 to midspan, the distributions are roughly uniform and almost zero for all three closing degrees, thus showing that the flow field is pure two-dimensional. The high secondary kinetic energy can be seen near the endwall at about z/H < 0.15 as a result of accumulation of vortex strength and flow overturning there. Maximum values of secondary kinetic energy can be recognized in the region where various vortex interact, producing high shear as impact of their opposite rotational direction.

Die approbierte gedruckte Originalversion dieser Dissertation ist an der TU Wien Bibliothek verfügbar.
The approved original version of this doctoral thesis is available in print at TU Wien Bibliothek.
TU Bibliothek Your knowledge hub WIEN

Figure 5.16b is total pressure coefficients analysed by pitchwise averaging. From this plot, the values of total pressure deficit appear to have increased in the secondary flow region, because of the growth of endwall boundary layer. The rise of total pressure deficit starts at z/H = 0.15 up to the endwall. This position corresponds with the loss accumulation caused by the secondary flows. At δ = 5%, there is not a qualitative difference in the spanwise distributions of two closing directions tested. However, at higher closing degrees δ = 15% and 30%, there is a significant discrepancy in the total pressure coefficient between CPS case and CSS one where the deficit of total pressure in the CPS is much lower than in the CSS case along the span as can be seen in the middle and bottom plots.

Die approbierte gedruckte Originalversion dieser Dissertation ist an der TU Wien Bibliothek verfügbar.
The approved original version of this doctoral thesis is available in print at TU Wien Bibliothek.

6 Conclusion and outlook

Experimental studies to improve the understanding of the throttling nozzle flow field have been developed through the linear turbine cascade wind tunnel. The detailed measurements were performed using a variety of the probes to reveal the midspan wake characteristics and secondary flow structures. The presented data include the blade loading, flow angles, total and static pressure, turbulence intensity, vorticity, and secondary kinetic energy. The main conclusions from this work can be drawn as follows.

Results of fully opened cascade measurement provide a basic description about the cascade flows in this thesis. The important conclusions based on this result are:

- Result of blade static pressure coefficient distribution shows that there was no evidence of suction side separation with strong favourable pressure gradient extends from leading edge up to suction peak, then the flow slightly meets adverse pressure gradient towards trailing edge. A strong favourable pressure gradient also was seen in short area of the pressure side up to x/b = 0.1, then followed again the flow was slightly undergoes an acceleration towards trailing edge.
- From midspan flows, it can be drawn that a large deviation of flow angle occurs in the wake with high non-uniformity covers area from y/t = 0.3 up to 0.8. Outside this region, the flow was uniform with velocity was almost unchanged, and it decreased drastically in the wake and reached minimum value of $C_1/C_0 = 2.54$. The static pressure coefficient distribution was not quite uniform along pitch, and its value slightly increased towards wake center, y/t = 0.5. While the distribution of total pressure coefficient was nearly symmetric about wake centre with its lowest value is -1.75. Meanwhile, the turbulence intensity distribution in the wake was asymmetric with double-peak characteristic. This distribution remined uniform in undistributed freestream region, and it increases up to a peak value in the wake.
- Based on the endwall flows, it was seen that flow structures downstream of the cascade were highly complex three-dimensional occupied by passage vortex, suction-side leg of horseshoe vortex and counter-rotating vortex concentrated near the endwall. The typical structure was flow overturning first up to the vortex core and then underturning toward midspan. Meanwhile, secondary kinetic energy was almost nearly zero from z/H = 0.25 to midspan, showing that flow field was a primary two-dimensional flow. From a total pressure coefficient distribution, it was shown that high deficit of total pressure covered the endwall areas up to 20% span.
- The highest uncertainty in total pressure coefficient was found in the wake and near the endwall. These are regions affected by boundary layer and secondary flows, where there are large variations of the flow properties from mainstream condition. Especially near the endwall, there was a strong correlation between places of high vorticity and places of high uncertainty. Zones with a high uncertainty could often be related to the locations where positive and negative vorticities met.

Die approbierte gedruckte Originalversion dieser Dissertation ist an der TU Wien Bibliothek verfügbar.
The approved original version of this doctoral thesis is available in print at TU Wien Bibliothek.
TU Bibliothek Your knowledge hub WIEN

Conclusions based on the two-dimensional results with different partial closing positions presented in this thesis are outlined follows:

- Based on the flow angle measurement, a large deviation in the wake region was seen for the flow angles which caused by high velocity gradients. This deviation was augmented through closing the flow passage, and its value was larger in the closing to suction side than in the closing to pressure side. This result can be explained that when the flow is flowing through the passage of closing to pressure side, the velocities in the tangential direction attenuated significantly due to the diffusion of boundary layer into the wake, and it generated relatively low deviation.
- Through the velocity profile, asymmetry was present in all wake distributions measured downstream of the cascade. Suction side wakes were thicker than the pressure side wakes due to different growth and development of boundary layers on the suction and pressure sides. For each closing direction, the spreading of the wake occurred in both directions, and its defects in the closing to suction side were higher than in the closing to pressure side case.
- From the static pressure distribution, the static pressure was almost uniform across the wake at all measurements. It should be noted that the distribution showed decreasingly trend with increasing of closing degree for both direction types, and its value reduced significantly mainly owing to the large closing degree.
- Based on the results of total pressure measurement, the wake characteristic showed that the stretching of wake increasing through closing of the cascade. The significant parts of inviscid region, starting from suction side, were occupied by the wake with increasing closing degree. The deficit in total pressure at closing to suction side was more than at closing to pressure side.
- From the turbulence intensity profiles, it was seen that the distribution is asymmetrical about the trailing edge axis, y/t = 0.5 with more significant differences occurred in the wake suction side. The asymmetrical profile reflects the different sizes of boundary layers exiting from blade passage. Additionally, the intensity was considerably higher around the wake containing suction side boundary layer for all both cases.

Results of three-dimensional flow analysis of the cascade at various partial closing degrees illustrated the complex nature of the flows. The main conclusions could be drawn from this analysis as follows

- Based on the isoclines contour, it was shown that there was not considerably change in flow turning over the endwall at low closing compared to fully opening, although some local variations did exist. In general, the flow turning increased with the increasing closing degree in both closing cases. It was also seen that the cores of passage vortex were found more clearly in the isoclines of pitchwise flow angle than in the spanwise flow angle distribution.
- Nondimensional velocity results showed that during the partially closing of the cascade, large velocity gradients caused high loss region in the total pressure coefficient. The velocity defect induces a large deficit of the total pressure near the endwall, which was

Die approbierte gedruckte Originalversion dieser Dissertation ist an der TU Wien Bibliothek verfügbar.
The approved original version of this doctoral thesis is available in print at TU Wien Bibliothek.
TU Bibliothek Your knowledge hub WIEN

marked augmentation in the magnitudes of velocity defect. The areas of velocity defect increase with the enlarge of closing degree for both closing cases tested.

- From the vorticity distribution, it was presented that passage vortex, suction-side leg of horseshoe vortex, and counter-rotating vortex were found with only a little difference in intensity and the position of the vortex cores for the closing to pressure side compared with the closing to suction side in all cases. However, the changes in the overall vortex structure are significant with increasing of the closing degree.
- Based on secondary kinetic energy coefficient distribution, it was shown that significant changes in the peak value of secondary kinetic energy occurred near the endwall with increasing the degree of closing in both closing cases tested. The high secondary kinetic illustrates the strong crossflow near the endwall. The rolling up of the secondary flows is believed because of pitchwise crossflow in this region.
- In general, the high-pressure deficit regions in the closing to suction side were wider compared with closing to pressure side case for all closing degrees. The cores of the total pressure deficit were seen at about 10%-15% of the span for all both closing cases tested. Furthermore, this study has revealed that changing of flow passage can shift the core location of total pressure deficit circumferentially.

The experiments have provided a vast amount of measurement data and led to a number of important outcomes with respect to the wake characteristics and endwall flow structures of the throttling nozzle, and confirmed several conclusions established in the previous study especially for findings of midspan flows. Moreover, the overall results from this work are believed to be helpful to enhance the understanding of complex flows and associated losses of throttling nozzle for both closing types of CPS and CSS.

For future works, from this investigation there are a few issues that can be recommended to develop on this study and within this research area as follows.

- One important task for future study is the measurement of blade loading in term of static pressure distribution. It is aimed to analyse how the interactions change the blade static pressure with changes of the closing degree.
- The next work is calculating pitchwise and spanwise vorticity by using a fine grid. A method for calculating these vorticity components has been presented in Section 4.2.5.
- The next research, it would be of great interest to study the wake and secondary flow for different cascades with the similar approach to obtain generic conclusions.
- The other work is eliminating several limitations in the evaluation of uncertainty. This includes determining missing systematic uncertainty and incorporating uncertainties from calibration process into the overall uncertainty measurement.
- Another task is the use of other techniques, for instance, using LDA (Laser Doppler Anemometry), PIV (Particle Image Velocimetry), as well as numerical calculations by involving incompressible and compressible issues.

Die approbierte gedruckte Originalversion dieser Dissertation ist an der TU Wien Bibliothek verfügbar.
The approved original version of this doctoral thesis is available in print at TU Wien Bibliothek.
TU Bibliothek Your knowledge hub WIEN

References

[1] Amin. S.: Siemens answers, oil & gas and industrial application division, SIEMENS, 2010.

[2] Batenin. V. M., Datsenko V. V., Zeigarnik Yu. A., Kosoi A. S., and Sinkevich M. V.: Thermodynamic evaluation of the possibility to increase cogeneration turbine efficiency by using a heat pump operating with steam, Thermal Engineering, vol. 63, no. 1, pp. 1–6, 2016.

[3] Benner. M. W., Sjolander. S. A., and Moustapha. S. H.: The influence of leading-edge geometry on secondary losses in a turbines cascade at the design incidence, ASME Journal of Turbomachinery, vol. 126, pp. 277–291, 2004.

[4] Binder. A. and Romey R.: Secondary flow effects and mixing of the wake behind a turbine stator, ASME Journal of Engineering for Power, vol. 105, pp. 40–46, 1983.

[5] Bindon. J. P.: The measurement and formation of tip clearance loss, ASME Journal of Turbomachinery, vol. 111, pp. 257–263, 1989.

[6] Bloch. H. P., and Singh M. P.: Steam turbines: design, applications, and rerating, Second Edition, The McGraw-Hill Companies. 2009.

[7] Bruun. H. H.: Interpretation of hot-wire probe signals in subsonic airflows, J. Phys. E: Sci. Instrum, vol. 12, pp. 1116–1128, 1979.

[8] Came. P. M., and Marsh H.: Secondary flow in cascades: Two simple derivations for the components of vorticity, Journal of Mechanical Engineering Science, vol. 16. no. 6. pp. 391–401, 1974.

[9] Coleman. H. W and Steele W. G.: Experimentation, validation, and uncertainty analysis for engineers, John Wiley and Sons, 2009.

[10] Coulon. V.: Experimental study of the free jet in a wind tunnel for probe calibration SEG, DLR-Interner Bericht. 223–96 A 58, 1997.

[11] Denton. J. D.: Loss mechanisms in turbomachines, ASME Journal of Turbomachinery, vol. 115, pp. 621–656, 1993.

[12] Deych. M. Y., and Troyanovskiy. B. M.: Investigation and calculation of axial turbine stages, FTD-MT-65–409, 1967.

[13] Gao. L., Zheng. Q., and Chen. H.: Comparative experimental investigation on aerodynamic performance of a steam turbine cascades, part II-stator vanes, ASME paper, GT2013–94815, 2013.

[14] Geist. R.: Dampfturbine mit einem Drehschieber, ABB Patent GmbH, European Patent Office, EP 0 568 909 A1, 10.11.1993.

Die approbierte gedruckte Originalversion dieser Dissertation ist an der TU Wien Bibliothek verfügbar.
The approved original version of this doctoral thesis is available in print at TU Wien Bibliothek.
TU Bibliothek Your knowledge hub WIEN

[15] Geist. R., and Jürke S.: Drehschieber mit mindestens einem Axialnadeldrehkranz als drehbewegliches Lagerelement, ABB Patent GmbH, DE 4425344A1, 1994.

[16] Gregory-Smith. D. G., and Cleak. J. G. E.: Secondary flow measurements in a turbine cascade with high inlet turbulence, ASME Paper, 90-GT-20, 1990.

[17] Hah. C.: A Navier-Stokes analysis of three-dimensional turbulent flows inside turbine blade rows at design and off-design conditions, Journal of Engineering for Gas Turbines and Power, vol. 106, pp. 421– 429, 1984.

[18] Heinke. W., Konig. S., Matyschok. B., Stoffel. B., Fialla. A., and Heinig. K.: Experimental investigations on steady wake effects in a high-lift turbine cascade, Experiments in Fluids, vol. 37, pp. 488-496, 2004.

[19] Hoheisel. H., Kiock. R., Lichtfuß. H. J., and Fottner. L.: Influence of free steam turbulence and blade pressure gradient on boundary layer and loss behavior of turbine cascades, ASME Paper, 86-GT-234, 1986.

[20] Horlock. J. H.: Losses and efficiencies in axial flow turbines, International Journal mechanical science, vol. 2, pp. 48–75, 1960.

[21] Horlock. J. H., and Lakshminarayana. B.: Secondary flows: theory, experiment, and application in Turbomachinery aerodynamics, Annual Review in Fluid Mechanics vol. 5. pp. 247–280, 1973.

[22] Jorgensen. F. E.: How to measure turbulence with hot-wire anemometers – a practical guide, Dantec Dynamics, DK-2740 Skovlunde, Denmark, 2002.

[23] Kariman. M. R.: Fluid dynamic investigation of an alternative extraction steam turbine control method: Rotary valve, Dissertation, Technische Universität Wien, Austria, 2013.

[24] Kiciński. J., and Lampart. P.: Cogeneration in a large and small scale, Acta Energitica, vol. 2, no. 2, 2009.

[25] King. L.V.: On the convection of heat from small cylinders in a stream of fluid: Determination of the convection constants of small platinum wires with applications to hot-wire anemometry, Philosophical Transaction of the Royal Society of London, pp. 373–432, 1914.

[26] Kline. S. J., and McClintok. F. A.: Describing uncertainties in single-sample experiments, Mechanical Engineering, pp. 3–8, 1953.

[27] Lampart. P., and Puzyrewski. R.: Numerical analysis of adaptive control in LP turbines, Task Quarterly, vol. 9, no.2, pp. 211–234, 2005.

[28] Langston. L. S.: Crossflows in a turbine cascade passage, ASME Journal of Engineering for Power, pp. 866–874, 1980.

[29] Luo. J., and Lakshminarayana. B.: Three-dimensional Navier-Stokes computation

Die approbierte gedruckte Originalversion dieser Dissertation ist an der TU Wien Bibliothek verfügbar.
The approved original version of this doctoral thesis is available in print at TU Wien Bibliothek.
TU Bibliothek Your knowledge hub WIEN

of turbine nozzle flow with advanced turbulence models, ASME Journal of Turbomachinery, vol. 119, pp. 516-530, 1997.

[30] MAN Turbo, Industrial steam turbines, 2002.

[31] Moore. J., and Adhye. R. Y.: Secondary flows and losses downstream of a turbine cascade, ASME Journal of Engineering for Gas Turbines and Power, vol. 107, pp. 961–968, 1985.

[32] Perdichizzi. A.: Mach number effects on secondary flow development downstream of a turbine cascade, ASME Journal of Turbomachinery, vol. 112, pp. 643–651, 1990.

[33] Perdichizzi. A., and Dossena. V.: Incidence angle and pitch-chord effects on secondary flows downstream of a turbine cascade, ASME Journal of Turbomachinery, vol. 115, pp. 383–391, 1993.

[34] Platz. R.: Industrial steam turbine control, Application Note 83403 (Revision B), Woodward Company, /12/Fort Collins, USA. 2008.

[35] Puzyrewski. R., Malec. A., and Gardzilewicz. A.: Redesign of adaptive stage for 25 MW cogeneration turbine, Proceeding of the Tenth Conference on Steam and Gas Turbines for Power and Cogeneration Plants, Czech Republic, pp. 219–223, 1994.

[36] Raj. R., and Lakshminarayana. B.: Characteristics of the wake behind a cascade of airfoils, Journal of Fluid Mechanics, vol. 61, part 4, pp. 707-730, 1973.

[37] Ramachandran. R., Krishna. H. C. R., and Narayana. P. A. A.: An experimental investigation of turbulent wake behind `S` shape profiles, J. India. Inst, Sci, no. 61(A), pp. 263–275, 1981.

[38] Sanz. W., Gehrer. A., Woisetschlager. J., Forstner. M., Artner. W., and Jericha. H.: Numerical and experimental investigation of the wake flow downstream of linear turbine cascade, ASME Paper, 98-GT-246, 1998.

[39] Sauer. H., Schmidt. R., and Vogeler. K.: Influence of chord length and inlet boundary layer on the secondary losses of turbine blades, ASME Journal of Turbomachinery, vol. 134, pp. 1–9, 2012.

[40] Sharma. O. P., and Butler. T. L.: Predictions of endwall losses and secondary flows in axial flow turbine cascades, ASME Journal of Turbomachinery, vol. 109, pp. 229–236, 1987.

[41] Sieverding. C. H.: Recent progress in the understanding of basic aspects of secondary flows in turbine blade passages, ASME Journal of Engineering for Gas Turbines and Power, vol. 107, pp. 248–257. 1985.

[42] Simoyu. L. L., Barinberg. G. D., Efros. E. I., Ermolaev. V. V., Zhuchenko. L. A., Shklyar. A. I., Sakhnin. Yu. A., Modenov. S. I., and Kalinin. B. B.: The

Die approbierte gedruckte Originalversion dieser Dissertation ist an der TU Wien Bibliothek verfügbar.
The approved original version of this doctoral thesis is available in print at TU Wien Bibliothek.
TU Bibliothek Your knowledge hub WIEN

effectiveness of modernization of the low-pressure cylinder of the T-185/220-12.8 turbine, Thermal Engineering, vol. 54, no. 4, pp. 286–291, 2007.

[43] Speicher. K., und Mietsch. E.: Der Drehschieber als Regelorgan für Entnahme-Dampfturbinen, Maschinenbautechnik 15-Heft 4, Berlin. VEB Verlag Technik, 1966.

[44] Sutherland. W.: The viscosity of gases and molecular force, Philosophical Magazine Series 5, 36:223, pp.507–531, 1893.

[45] Treaster. A. L and Yocum. A. M.: The calibration and application of five-hole probes, ISA Transactions, vol. 18, no. 3, pp. 23–34, 1979.

[46] Walsh. J. A., and Gregory-Smith. D. G.: Inlet skew and the growth of secondary losses and vorticity in a turbine cascade, ASME Paper, 89-GT-65, 1989.

[47] Wang. H. P., Olson S. J., Goldstein. R. J., and Eckert. E. R. G.: Flow visualization in a linear turbine cascade of high-performance turbine blades, ASME Journal of Turbomachinery, vol.119, pp. 1–8, 1997.

[48] Weiss. A. P, and Fottner. L.: The influence of load distribution on secondary flow in straight turbine cascades, Journal of Turbomachinery, vol.117, pp. 133–141, 1995.

[49] Willinger. R.: Thermische Turbomachinen, Skriptum zur Vorlesung, Technische Universitat Wien, Austria. 2015.

[50] Willinger. R.: Beitrag zur aerodynamischen Wechselwirkung zwischen axialer Turbinenstufe und nachgeschaltetem Diffusor, Dissertation, Technische Universität Wien, Austria, 1997.

[51] Xu. C., and Amano. R. S.: Computational analysis of pitch-width effects on the secondary flows of turbine blades, Computational Mechanics, vol. 34, pp. 111–120, 2004.

[52] Yamamoto. A.: Production and development of secondary flows and losses in two types of straight turbine cascades: Part 1-A stator case, ASME Journal of Turbomachinery, vol.109, pp. 186–193, 1987.

[53] Zaccaria. M., and Lakshminarayana. B.: Investigation of three-dimensional flow field at the exit of a turbine nozzle, AIAA Journal of Propulsion and Power, vol. 11, no.1, 1995.

[54] Zaccaria. M., Ristic. D., and Lakshminarayana. B.: Three-dimensional flow field in a turbine nozzle passage, AIAA Journal of Propulsion and Power, vol. 12, pp. 974–983, 1996.

[55] Zweifel. O.: Die Frage der optimalen Schaufelteilung bei Beschauflungen von Turbomaschinen, insbesondere bei grosser Umlenkung in den Schaufelreihen, Brown Boveri Mitteilungen, pp. 436–444, 1945.

Die approbierte gedruckte Originalversion dieser Dissertation ist an der TU Wien Bibliothek verfügbar.
The approved original version of this doctoral thesis is available in print at TU Wien Bibliothek.
TU Bibliothek Your knowledge hub WIEN

Appendix A. Thermodynamic relationships

This appendix presents a derivation of the change in entropy based on measurable flow parameters using the first and second laws of thermodynamics. These laws relate entropy (s), internal energy (u), pressure (p), and specific volume (v) which is

$$Tds = du + pdv. \tag{A.1}$$

Considering a fixed mass system, the specific (per mass) values are considered. This equation is comprised entirely of state variables and is thus path independent. Therefore, only the inlet and exit states are needed for integration. This research is performed in the air, so the perfect gas laws can be applied.

From the definition of enthalpy, $h = u + pv$, one can find

$$dh = du + pdv + vdp \tag{A.2}$$

or

$$du + pdv = dh - vdp. \tag{A.3}$$

From equation (A.1), eliminating du and pdv, therefore equation (A.3) becomes

$$Tds = dh - vdp. \tag{A.4}$$

Differential changes in entropy can be obtained as

$$ds = \frac{du}{T} + \frac{pdv}{T} \quad \text{and} \quad ds = \frac{dh}{T} - \frac{vdp}{T}. \tag{A.5}$$

For ideal gas, the relationship between du or dh and T is expressed as

$$c_v = \frac{du}{dT} \quad \text{and} \quad c_p = \frac{dh}{dT}. \tag{A.6}$$

Using equation (A.6), then equation (A.5) can be integrated to give

$$s_1 - s_0 = \int_0^1 \frac{c_v dT}{T} + \int_0^1 \frac{Rdv}{v} \tag{A.7}$$

$$s_1 - s_0 = \int_0^1 \frac{c_p dT}{T} - \int_0^1 \frac{Rdp}{p}. \tag{A.8}$$

Die approbierte gedruckte Originalversion dieser Dissertation ist an der TU Wien Bibliothek verfügbar.
The approved original version of this doctoral thesis is available in print at TU Wien Bibliothek.
TU Bibliothek Your knowledge hub WIEN

The constants R and c_p can be pulled out of the integrals. The change in entropy can then be written as

$$s_1 - s_0 = c_v \ln\left(\frac{T_1}{T_0}\right) + R \ln\left(\frac{v_1}{v_0}\right) \tag{A.9}$$

and

$$s_1 - s_0 = c_p \ln\left(\frac{T_1}{T_0}\right) - R \ln\left(\frac{p_1}{p_0}\right). \tag{A.10}$$

Equation (A.10) says that the ratio of the total pressures in the control volume measured upstream and downstream of a blade row is proportional to the change in entropy. This means that the change in entropy is related to the ratios of temperature and pressure.

This research involves a fixed specific volume, so dv = 0. Finally, given that the temperature change in the cascade is negligible and the flow is incompressible, entropy equation then simplifies to

$$s_1 - s_0 = -R \ln\left(\frac{p_1}{p_0}\right). \tag{A.11}$$

This equation means that the entropy production is proportional to the ratio of total pressures in the control volume measured upstream and downstream of low speed blade cascade. This is the approach is used to calculate the losses related to turbine cascade.

For the isentropic process of perfect gases, the relations can be found by setting ds = 0, equation (A.9) and equation (A.10) can be written as

$$\ln\left(\frac{T_1}{T_0}\right) = -\frac{R}{c_v} \ln\left(\frac{v_1}{v_0}\right) \tag{A.12}$$

and

$$\ln\left(\frac{T_1}{T_0}\right) = \frac{R}{c_p} \ln\left(\frac{p_1}{p_0}\right). \tag{A.13}$$

From ideal gases relation, $Pv = RT$ and $h = u + Pv$, differentiate this relationship with respect to temperature T

$$\frac{dh}{dT} = \frac{du}{dT} + R \tag{A.14}$$

$$c_p = c_v + R \tag{A.15}$$

Die approbierte gedruckte Originalversion dieser Dissertation ist an der TU Wien Bibliothek verfügbar.
The approved original version of this doctoral thesis is available in print at TU Wien Bibliothek.
TU Bibliothek Your knowledge hub WIEN

$$k = \frac{c_p}{c_v} \quad \text{then} \quad c_p = \frac{kR}{k-1} \quad c_v = \frac{R}{k-1} \tag{A.16}$$

equation (A.12) and equation (A.13) are arranged to become

$$\ln\left(\frac{T_1}{T_0}\right) = -\frac{c_p - c_v}{c_v} \ln\left(\frac{v_1}{v_0}\right) = -(k-1)\ln\left(\frac{v_1}{v_0}\right) \tag{A.17}$$

and

$$\ln\left(\frac{T_1}{T_0}\right) = \frac{c_p - c_v}{c_p} \ln\left(\frac{p_1}{p_0}\right) = \frac{k-1}{k} \ln\left(\frac{p_1}{p_0}\right). \tag{A.18}$$

From equation (A.17) and (A.18) we get relations as

$$\frac{T_0}{T} = \left(\frac{v}{v_0}\right)^{k-1} = \left(\frac{\rho_0}{\rho}\right)^{k-1} \tag{A.19}$$

and

$$\frac{T_0}{T} = \left(\frac{p_0}{p}\right)^{\frac{k-1}{k}}. \tag{A.20}$$

Combining equation (A.19) and equation (A.20), we obtain

$$\frac{p_0}{p} = \left(\frac{v}{v_0}\right)^{k}. \tag{A.21}$$

This equation is a relation for perfect gases in isentropic condition.

Die approbierte gedruckte Originalversion dieser Dissertation ist an der TU Wien Bibliothek verfügbar.
The approved original version of this doctoral thesis is available in print at TU Wien Bibliothek.
TU Bibliothek Your knowledge hub WIEN

Appendix B. Laboratory facilities

B.1 Linear cascade wind tunnel

Figure B.1 Linear cascade wind tunnel at Institute for Energy Systems and Thermodynamics, Technische Universität Wien

B.2 Turbine cascade model

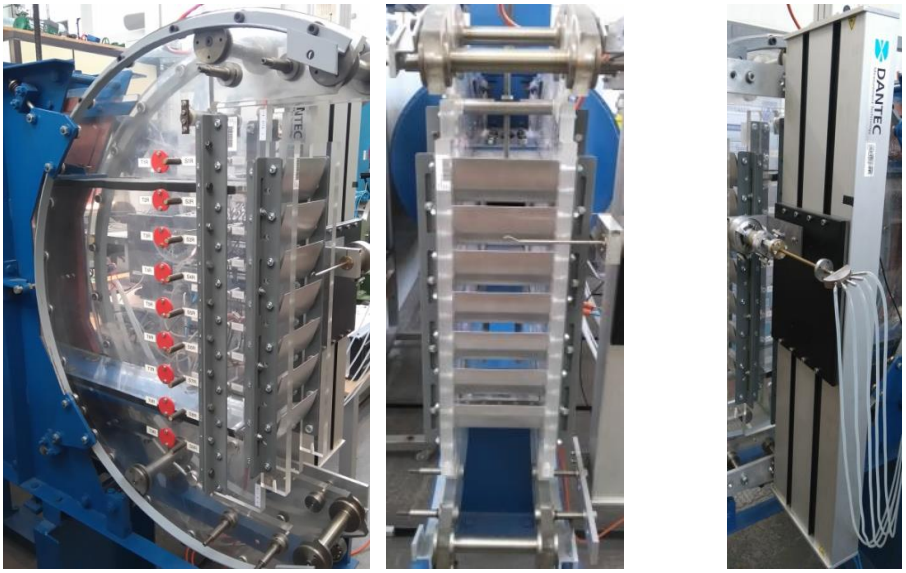

(a) (b)

Figure B.2 (a) Testing cascade model; and (b) DANTEC traversing mechanism unit

Die approbierte gedruckte Originalversion dieser Dissertation ist an der TU Wien Bibliothek verfügbar.
The approved original version of this doctoral thesis is available in print at TU Wien Bibliothek.
TU Bibliothek Your knowledge hub WIEN

B.3 Free jet facility

Figure B.3 Free jet facility with support devices at Institute for Energy Systems and Thermodynamics, Technische Universität Wien

B.4 Pneumatic probes

- Three-hole probe
- Five-hole probe

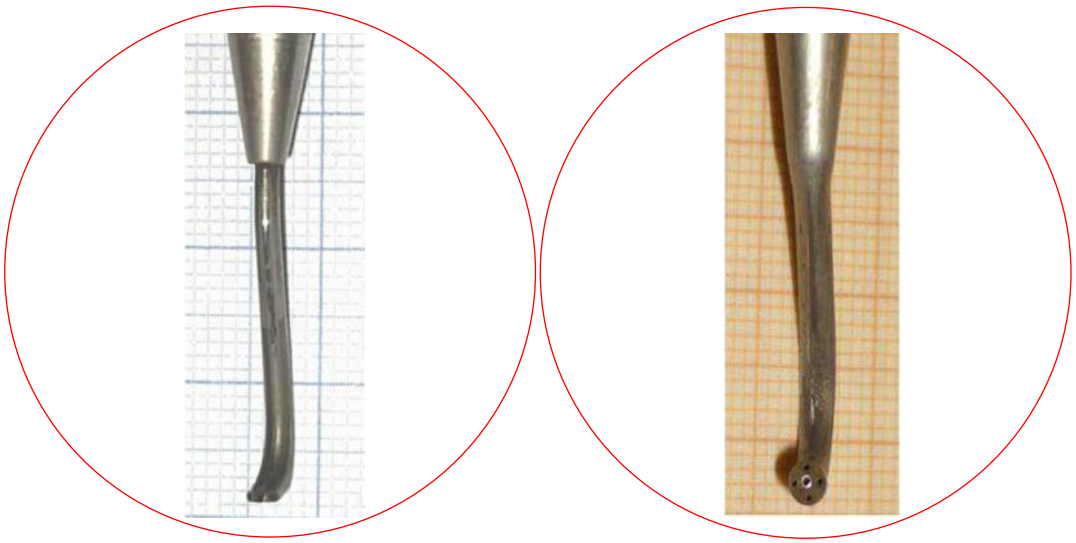

(a) (b)

Figure B.4 (a) Three-hole probe (3H-P); and (b) Five-hole probe (5H-P)

Die approbierte gedruckte Originalversion dieser Dissertation ist an der TU Wien Bibliothek verfügbar.
The approved original version of this doctoral thesis is available in print at TU Wien Bibliothek.
TU Bibliothek Your knowledge hub WIEN

Curriculum vitae

Name	:	Khoiri Rozi
Date of Birth	:	16 February 1976
Marital Status	:	Married
Office	:	Faculty of Engineering, Diponegoro University, Semarang
Address	:	Jl. Prof. Soedarto, SH, Tembalang 50275, Semarang – Indonesia

Education

1995-1996	Bachelor student in Engineering of Physics, Sepuluh Nopember Institute of Technology, Indonesia.
1996-2004	Bachelor student in Mechanical Engineering, Sepuluh Nopember Institute of Technology, Indonesia.
2006-2009	Master student in Mechanical Engineering, Sepuluh Nopember Institute of Technology, Indonesia.
From 2014	PhD candidate in Mechanical Engineering, Technische Universität Wien, Austria.

Job Experience

2010-2014	Worked as Lecturer at Department of Mechanical Engineering, Faculty of Engineering, Diponegoro University, Indonesia.

Die approbierte gedruckte Originalversion dieser Dissertation ist an der TU Wien Bibliothek verfügbar.
The approved original version of this doctoral thesis is available in print at TU Wien Bibliothek.